

ENVIRONMENTALLY SUSTAINABLE SYNTHESIS OF NOVEL NANO ASSISTED  
ION EXCHANGE SYSTEMS FOR FACILE AND HIGH-CAPACITY WATER  
PURIFICATION

by

Abhispa Sahu

A dissertation submitted to the faculty of  
The University of North Carolina at Charlotte  
in partial fulfillment of the requirements  
for the degree of Doctor of Philosophy in  
Nanoscale Science

Charlotte

2020

Approved by:

---

Dr. Jordan C. Poler

---

Dr. James E. Amburgey

---

Dr. HaiTao Zhang

---

Dr. Swarnapali De Silva Indrasekara

---

Dr. Terry Xu

©2020  
Abhispa Sahu  
ALL RIGHTS RESERVED

## ABSTRACT

ABHISPA SAHU. Environmentally sustainable synthesis of novel nano assisted ion exchange systems for facile and high-capacity water purification (Under the direction of PROFESSOR JORDAN C. POLER)

Demand for clean and safe drinking water is a global challenge because of water scarcity, growth of human population, urbanization, and anthropogenic pollution. Purification of water involves removal of small molecules and ions from ground water addressed as “emerging contaminants” which are extremely mobile and toxic in nature, do not degrade or hydrolyze easily, and highly soluble in water resulting in bioaccumulation. Most of the current water treatment systems have complex deficiencies that affect their overall performance. We have synthesized carbon nanostructures assisted ion exchange resins in aqueous medium that help remove these emerging contaminants in a fast, easy, and high capacity manner while supporting less contact time and low transmembrane resistance primarily achieved using thin film assemblies. We have developed a novel sonochemistry assisted atom transfer radical polymerization (SONO-ATRP) process for synthesis of polyelectrolyte anion exchange resins in water without use of any external initiator or reducing agents while using only a few ppm of catalyst. We successfully performed high-density functionalization of polyelectrolyte anion exchange resin strands onto single walled carbon nanotubes sidewalls using the SONO-ATRP process while at low reaction temperatures thereby providing a less energy intensive alternative for green chemistry. We have developed green processes to defluorinate fluorographite in water and simultaneously perform covalent grafting of anionic short brushes of poly(vinyl benzyl trimethylammonium chloride) to its surface under mild reaction conditions

without need of any external reactive reagents. Field Emission Scanning Electron microscopy of thin film of functionalized carbon nanotubes demonstrated pin-hole free mesoporous architecture illustrating scaffold robustness while thin films of functionalized fluorographite exhibited stacked arrangement of plate-like structures. Exfoliation and functionalization of fluorographite was revealed through Transmission Electron Microscopy. Both the resins demonstrated high water flux ( $>1500 \text{ L m}^{-2}\text{h}^{-1}\text{bar}^{-1}$ ) due to their intrinsic architecture and high percent removal ( $>90\%$ ) of contaminants due to the tortuous path length during molecular transport through the membrane. These properties enable adsorption of impurities at environmentally relevant concentrations. These materials exhibited facile regeneration and reuse of the thin films, thus supporting sustainability. In conclusion, these processes abide by the principles of green chemistry and their processability opens new avenues for smart point-of-use water purification systems.

## ACKNOWLEDGMENTS

I would like to first acknowledge my advisor, Professor Jordan C. Poler for being a constant support throughout my Ph.D. journey. Your unceasing motivation pushed me to become a better researcher. You taught me to never underestimate the potential of any tiny morsel of life, introduced me to efficient multi-tasking, and were always there to teach me any skill that I lacked. With time, I became independent and was able to carry out all research activities on my own and I immensely thank you for taking the time and teaching me most of the life and technical skills I have learnt so far. You mentally stimulated me and made me realize that I was capable of generating innovative ideas. In addition to work, you always looked after me like a guardian which was very valuable to me being away from home including the small gestures like invitation to Thanksgiving dinners (I want to especially thank Caroline!), celebrating birthday parties, driving me to different work locations because I cannot drive, etc. all of these mean a lot to me. I extremely thank my other dissertation committee members, Dr. Zhang, Dr. Indrasekara, Dr. Amburgey, and Dr. Xu for their constant support, guidance, and patience with me. I am also grateful to all the JSNN folks (Dr. Jeffry Alston, Haley Harrison, Matt Craps and Klint Davis) for sharing their research expertise and helping me with the characterization data and their analyses. I would like to thank all the amazing PRG members I met and worked with throughout this journey. I immensely thank Timothy Eldred, who helped me get started with synthesis and characterization skills, Justin Zuczek, who made my life easier while I was toiling for long hours in the lab. I thank each undergraduate I met in my journey, Rabia Sheikh, Kayla Durkin, Kayla Blackburn, Matthew Bonfield, Anna Jones, Rachel Rollins, Andrew Hirasawa, Nick Zelenka, Terawit Kongruengkit, William

Hixon, and Nesreen Elathram. I thank Adriana, Chauncey, and Nicolas whom I met for a very short period of time. I wish Jenny, Abby, Sydney, and CJ good luck on their future endeavors. I cannot thank enough all the graduating or graduated students I met in this journey who taught me how to survive Ph.D., were there for me emotionally and intellectually, and gave me some of the wisest life and research advice. I would like to thank Nanoscale Science department of UNC Charlotte for providing me with various experiences in graduate-level and research-level platform. I would also like to thank US EPA for awarding my team with P3 Phase I and for appreciating our work on a national platform. Lastly, I would like to thank my parents, my brother and sister-in-law, and extremely close friends (Abhisek!) who have always been my support and have always believed in me more than I believed in myself.

## TABLE OF CONTENTS

LIST OF FIGURES	xi
LIST OF TABLES	xvi
LIST OF ABBREVIATIONS	xviii
CHAPTER 1: Introduction	1
1.1 Background	1
1.1.1 Water Purification	1
1.1.2 Processes of water purification	2
1.1.3 Nanomaterials for water purification	5
1.2 Activator regenerated by electron transfer assisted atom transfer radical polymerization (ARGET ATRP)	7
1.3 Green Chemistry, Synthesis and Functionalization	9
1.3.1 Green Synthesis and functionalization using Sonochemistry	10
1.3.2 Green functionalization using functional 2D materials	11
1.3.2.1 Fluorographite	12
1.4 Structure-property-function relationships through characterization and water purification testing	13
CHAPTER 2	16
Abstract	17
Introduction	18
2.1 Synthetic Methods	21
2.1.1 Materials and Methods.	21
2.1.2 Workup of the synthesis required	22
2.1.3 Aqueous Synthesis of vbTMAC polyelectrolytes.	22
2.1.4 Aqueous Synthesis of functionalized SWCNT nanoresin (Aq-SNR).	23
2.1.5 Purification of as-synthesized Aq-SNR	24
2.2 Characterization Methods	25
2.2.1 Kinetics of polymer growth.	25
2.2.2 UV-Vis-NIR Spectroscopy.	26
2.2.3 Raman Spectroscopy for covalent functionalization of SWCNTs.	26
2.2.4 Total Organic Carbon (TOC) Analysis of aqueous analyte.	26
2.2.5 Dynamic Light Scattering (DLS) and Zeta Potential.	27

2.2.6 Scanning Electron Microscopy (SEM).	27
2.2.7 Analyte Adsorption Capacity Studies.	28
2.2.8 Adsorption Capacity: Fast-Filtration.	28
2.2.9 Regeneration and Reuse Studies.	28
2.3 Results and Discussion	29
2.3.2 Adsorption Capacity Testing.	33
2.3.3 Percentage removal of Analyte.	34
2.4 Conclusions.	35
Safety	36
Acknowledgements.	36
2.5 References.	37
2.6 Figures and Tables	41
2.7 Supplementary figures and tables	48
CHAPTER 3	64
Abstract	65
3.1 Introduction	66
3.1.1 Sonochemical ATRP	66
3.1.2 Ultrasonic debundling of nanomaterials	67
3.2 Materials and methods	67
3.2.1 Chemicals and Materials	67
3.2.2 Workup and Purification	68
3.2.3 ARGET ATRP synthesis of poly(vbTMAC)	68
3.2.4 Sonochemically assisted ARGET ATRP poly(vbTMAC) syntheses (SONO-ARGET-ATRP)	69
3.2.5 Sonochemically assisted ATRP initiation and propagation (SONO-ATRP-initiation and SONO-ATRP-propagation)	69
3.2.6 Sonochemically assisted ATRP poly(vbTMAC) synthesis (SONO-ATRP)	70
3.2.7 Aqueous sonochemically assisted ARGET ATRP functionalization of SWCNT NanoResin (Aq-SONO-ARGET ATRP-SNR)	71
3.2.8 Aqueous sonochemically assisted ATRP functionalization of SWCNT NanoResin (Aq-SONO-ATRP-SNR) as function of reaction temperature	71

3.2.9	Purification of sonochemically functionalized NanoResins (Aq-SONO-ARGET ATRP-SNR and Aq-SONO-ATRP-SNR) and determination of percent functionalization	73
3.2.10	Characterization techniques	73
3.2.11	Breakthrough studies	75
3.3	Results and Discussion	76
3.3.1	Sonochemical functionalization of SWCNTs	76
3.3.2	Sonochemistry kinetics and NanoResin percent functionalization	77
3.3.3	Sonochemistry kinetics and polymer percent conversion	80
3.3.4	Sonochemical polymerization and control studies	82
3.3.5	Covalent functionalization to SWCNTs	85
3.3.6	Nanoscale Anion Exchange Resins for Water Purification	87
3.4	Conclusions	91
3.5	References	93
3.6	Figures and tables	98
3.7	Supplementary figures and tables	106
CHAPTER 4		125
Abstract		126
Introduction		127
4.2	Materials	130
4.2.1	Chemicals and Materials	130
4.2.2	Workup and purification	131
4.3	Method.	132
4.3.1	Synthetic methods.	132
4.3.1.1	Aqueous synthesis of polyelectrolyte functionalized fluorographite in presence of external radical, catalyst complex and reducing agent using sonochemistry and reflux (PFG-I)	132
4.3.1.2	Aqueous synthesis of polyelectrolyte functionalized fluorographite in presence of reducing agent, catalyst complex and absence of external radical using sonochemistry and reflux (PFG-II)	133
4.3.1.3	Aqueous synthesis of polyelectrolyte functionalized fluorographite in presence of catalyst complex and absence of reducing agent and external radical under sonochemistry and reflux (PFG-III)	134

4.3.1.4 Aqueous synthesis of polyelectrolyte functionalized fluorographite in absence of catalyst complex, reducing agent and external radical under sonochemistry and reflux (PFG-IV)	136
4.3.1.5 Aqueous synthesis of polyelectrolyte functionalized fluorographite in absence of catalyst complex, reducing agent and external radical under reflux (PFG-V)	136
4.3.1.6 Control studies	137
4.3.2 Characterization Methods.	137
4.3.2.1 Dynamic Light Scattering	137
4.3.2.2. Attenuated Total Reflectance Fourier Transform Infrared Spectroscopy	137
4.3.2.3 Raman Spectroscopy	138
4.3.2.4 X-Ray Photoelectron Spectroscopy	138
4.3.2.5 X-Ray Powder Diffraction	138
4.3.2.6 Transmission Electron Microscopy	139
4.3.2.7 Thermogravimetric Analysis	139
4.3.3 Purification and performance evaluation.	139
4.3.3.1 Water flux studies	139
4.3.3.2 Kinetic studies	140
4.3.3.3 Adsorption Isotherm	140
4.3.3.4 Analyte adsorption studies	140
4.3.3.5 Regeneration Studies	141
4.4 Results and Discussion	142
4.4.1 Synthesis, morphological and physicochemical characterization of poly(vbTMAC) functionalized fluorographite (PFG):	142
4.4.2 Morphology of thin films, Adsorption Kinetics and Isotherm, Water Purification Testing:	147
4.5 Conclusion	151
4.6 References:	153
4.7 Figures and Tables	158
4.8 Supplementary Figures and tables	167
OVERALL CONCLUSIONS	177
Future Prospects	181
Introduction References:	183

## LIST OF FIGURES

Scheme 1. Mechanism of ARGET ATRP	7
Figure 2.1. Removal of vbTMAC monomer and unbound polymer after successive centrifugation and dispersal into brine cycles. UV-Vis determination of concentration	42
Figure 2.2. Normalized Raman spectra of a 2 h Pristine SWCNT and Aq-SNR after centrifugation at 20,000 RCF for 1 hr.	43
Figure 2.3. FE-SEM images of pristine SWCNTs (A) and Aq-SNR (B) drop cast from a dilute dispersion onto a Si chip.	44
Figure 2.4. Equilibrium loading capacity of NaFL onto Aq-SNR using an initial concentration $C_0 = 5.8$ mg-C/L.	45
Figure 2.5. Percent removal of analyte versus Aq-SNR membrane mass	46
Figure 2.6. Regeneration and reusability study.	47
Figure S2.1: After centrifugation at 100,000 RCF (1 h), the reaction mixture deposits at the wall of the polycarbonate tubes	48
Figure S2.2: Brine removal from Aq-SNR dispersion.	49
Figure S2.3: Reaction scheme showing the change from vinylic to allylic conditions for the terminal hydrogen.	50
Figure S2.4: $^1\text{H}$ NMR spectra of reaction mixtures from polymerization reaction versus time.	51
Figure S2.5: Percent conversion (lower) and $\ln([M]_0/[M])$ (upper) versus time.	52
Figure S2.6: Adsorption kinetics of surrogate NOM NaFL into a thin Aq-SNR membrane.	53
Figure S2.8: Zeta potential characterization of ionomer after 30 min of growth or 25% conversion.	54
Figure S2.7: DLS characterization of ionomer after 30 min of growth or 25% conversion.	54
Figure S2.9: EDX of 2 h Aq-SNR thin film on MCE membrane.	55
Figure S2.10: FE-SEM micrographs of Aq-SNR thin film on top of an MCE membrane.	56

Figure S2.11: AFM micrographs of Aq-SNR thin film on top of an MCE membrane.	57
Figure S2.12: Baseline-Normalized Raman spectra of Pristine SWCNT compared to: 2h (left), 12h (center), and 3 day (right) Aq-SNR after centrifugation at 20,000 RCF for 1 h.	58
Figure S2.13: Baseline-Normalized Raman spectra of Pristine SWCNT and 3 day Aq-SNR after centrifugation at 200,000 RCF for 1 h.	59
Figure S2.14: Zeta potential data for 2h (top) and 12h (bottom) functionalized Aq-SNR.	60
Figure S2.15: DLS data for 2h (top), 12h (middle) and 3 day (bottom) functionalized Aq-SNR.	61
Figure S2.16: Equilibrium loading capacity of NaFL onto Aq-SNR using an initial concentration $C_o = 5.8$ mg-C/L.	62
Figure 3.1: Total-mass per SWCNT mass ratio versus functionalization process.	98
Figure 3.2: SONO-ATRP % functionalization as a function of temperature.	99
Figure 3.3: Growth kinetics of SONO-ATRP of poly(vbTMAC) as a function of temperature using ultrasonication	100
Figure 3.4: Breakthrough curves (ratio of effluent concentration, [NaFL] and feed concentration, [NaFL] <sub>o</sub> as function of effective volume).	103
Figure 3.5: Effective volume at 10% breakthrough versus %Functionalization for various NanoResin membranes.	104
Figure 3.6: Molecular mechanics geometry optimization of Aq-SNR film. %Functionalization = 1.5 (left) and 3.0 (right).	104
Figure 3.7: NaFL loading onto NanoResin thin film versus effective analyte volume.	105
Figure 3.8: NanoResin membrane before any breakthrough experiments (left) and then after the 3 <sup>rd</sup> breakthrough experiment (right).	105
Figure S3.1: Growth kinetics of ARGET-ATRP of poly(vbTMAC) as a function of temperature under conditions	107
Figure S3.2: Growth kinetics of SONO-ATRP of poly(vbTMAC) as a function of temperature using $125.2 \text{ W cm}^{-2}$ ultrasonication intensity	108

Figure S3.3: (a) Arrhenius and (b) Eyring plots for poly(vbTMAC) using ARGET ATRP in aqueous medium	109
Figure S3.4: Arrhenius plot for poly(vbTMAC) using Aq-SONO-ATRP at $36 \text{ W cm}^{-2}$ in aqueous medium performed using thin probe sonicator.	109
Figure S3.5: Effective hydrodynamic diameter (nm) of poly(vbTMAC) using Aq-SONO-ATRP at $144 \text{ W cm}^{-2}$ for 4 h resulting in 93% conversion.	111
Figure S3.6: Zeta potential of $0 \text{ }^\circ\text{C}$ functionalized Aq-SONO-ATRP-SNR with total mass per SWCNT-mass ratio of 3.04.	113
Figure S3.7: Zeta potential of stable dispersion from supernatant of $0 \text{ }^\circ\text{C}$ functionalized Aq-SONO-ATRP-SNR centrifuged at 20,000 g.	114
Figure S3.8: Zeta potential of $85 \text{ }^\circ\text{C}$ functionalized Aq-SONO-ATRP-SNR with total mass per SWCNT-mass ratio of 1.74.	115
Figure S3.9: Zeta potential of stable dispersion from supernatant of $85 \text{ }^\circ\text{C}$ functionalized Aq-SONO-ATRP-SNR centrifuged at 20,000 g.	116
Figure S3.10: Effective hydrodynamic diameter (nm) of stable dispersion from supernatant of $0 \text{ }^\circ\text{C}$ functionalized Aq-SONO-ATRP-SNR centrifuged at 20,000 g.	117
Figure S3.11: Effective hydrodynamic diameter (nm) of stable dispersion from supernatant of $85 \text{ }^\circ\text{C}$ functionalized Aq-SONO-ATRP-SNR centrifuged at 20,000 g.	118
Figure S3.12: Breakthrough curves (ratio of outlet NaFL concentration, $[\text{NaFL}]$ and feed concentration, $[\text{NaFL}]_0$ as function of effective volume) for NaFL adsorption by Aq-SNR of different mechanisms and durations of functionalization.	120
Figure S3.13: Breakthrough curves (ratio of outlet NaFL concentration, $[\text{NaFL}]$ and feed concentration, $[\text{NaFL}]_0$ as function of effective volume) for NaFL adsorption by 2 h functionalized Aq-SONO-ATRP-SNR (two pot, 30-mer) NanoResin.	121
Figure S3.14: Schlenk apparatus with sonicator probe sealed and vessel under Ar(g) positive pressure	122
Figure 4.1. (a) ATR FTIR spectra of fluorographite and PFG-V demonstrating defluorination and functionalization of poly(vbTMAC) on fluorographite; (b) XPS survey scan of fluorographite, PFG-I and PFG-V; high resolution C 1s spectra of (c) fluorographite and (d) PFG-V and their deconvolutions results.	159
Figure 4.2. Measured EELS spectra showing F-K edge of (a) Fluorographite (b) PFG-V exhibiting characteristic post peak at 700 eV supporting defluorination processes.	160

Figure 4.3. Transmission electron micrographs of (a,b) fluorographite sheets (c,d) PFG-I. SAED pattern of (e) PFG-I (f) PFG-V exhibited similar diffraction pattern as presented in XRD analysis.	161
Figure 4.4. XRD patterns of pristine fluorographite and PFG-I.	162
Figure 4.5. Raman spectra of (a) Fluorographite and (b) PFG-V. Crystallite size of the samples, L was calculated using Raman analysis.	162
Figure 4.6. Scanning Electron Micrographs of PFG-II thin film revealing plate like morphology.	163
Figure 4.7. Kinetic studies of PFG-II using NaFL as analyte. 3.11 mg-C/L and 5.86 mg-c/L are two initial concentrations of NaFL.	163
Figure 4.8. Adsorption isotherm of PFG-V	164
Figure 4.9. Percent removal of emerging contaminants by PFG-I as a function of mass density ( $\text{mg cm}^{-2}$ ) of PFG thin film deposited on MCE membrane (13 mm wide, 0.2 $\mu\text{m}$ pore size).	165
Figure 4.10. Percent removal of $\text{AsO}_4^{3-}/\text{OH}^{1-}$ to assess co-selectivity of PFG-II resin in presence of $\text{OH}^-$ ions.	166
Figure 4.11. Regeneration and reusability studies of PFG-I thin films using NaFL as surrogate.	166
Figure S4.1. Change of color and dispersibility of PFG-V reaction (a) start of the reaction (b) after 3 days (c) purified PFG-V	167
Figure S4.2. ATR FTIR of fluorographite and PFG-II	167
Figure S4.3. High resolution C 1s spectra of PFG-I and its deconvolutions results.	168
Figure S4.4. TGA thermogram of PFG-V (in air mode)	168
Figure S4.5. Transmission electron micrograph of PFG-V.	169
Figure S4.6. Effective hydrodynamic diameter (nm) of PFG-I dispersion.	170
Figure S4.7. Zeta potential (mV) of PFG-I dispersion.	171
Figure S4.8. Effective hydrodynamic diameter (nm) of PFG-V dispersion.	172
Figure S4.9. Effective zeta potential (mV) of PFG-V dispersion.	173

Figure S4.10: Different batches of controlled experiments in cold bath (a) FGI in water after 2 h sonication at  $90 \text{ W cm}^{-2}$  for 2 h (b) FGi and PEG in water (c) FGi in water stirred for 3 days. 175

Figure S4.11: Different batches of controlled experiments in reflux (a) FGi in water (b) FGi and PEG in water under reflux for 3 days 176

## LIST OF TABLES

Table 1.1: MCL values of some emerging contaminants as reported by US EPA	1
Table 1.2: Types of Water Purification techniques	3
Table 1.3: Overview of advantages and disadvantages of various nanomaterials to act as scaffolds for water/wastewater purification/treatment processes	6
Table S2.1: Adsorption of various analytes onto Aq-SNR thin films	63
Table 3.1: % monomer conversions of SONO-ATRP-I and SONO-ATRP-P as a function of power intensities under conditions: $T_{\text{bulk}} = 10\text{ }^{\circ}\text{C}$ during sonochemistry ( $\Delta t =$ sonication duration). $T_{\text{bulk}} = \sim 100\text{ }^{\circ}\text{C}$ during reflux.	101
Table 3.2: D:G ratio of Raman spectra of Pristine SWCNT compared to Aq-SNR synthesized under different conditions	102
Table S3.1: Apparent values of propagation rate constants ( $k_{\text{app}}$ ) of ARGET ATRP, SONO-ARGET ATRP and SONO-ATRP reactions calculated from slopes of $\ln(\text{Mo}/\text{M})$ vs time at different temperatures	106
Table S3.2: DLS and Zeta potential measurements.	110
Table S3.3. Membrane kinetic parameters analyzed for adsorption of $0.86\text{ mg-C L}^{-1}$ NaFL onto 3 mg of NanoResin thin film.	119
Table 4.1. Elemental composition (in terms of At%) of fluorographite, fluorographite under reflux (control studies) PFG-I and PFG-V analyzed by XPS.	158
Table 4.2. Crystallite sizes calculated from Raman analysis using the formula $(2.4 \times 10^{-10})\lambda \frac{I_D}{I_G}^{-1}$	161
Table 4.3: Water flux measurements of PFG-II thin films deposited on MCE determined at specific pressure.	164
Table S4.1. List of d-spacing values calculated by measuring the area of the rings in SAED pattern and finding radius using ImageJ software	169
Table S4.2 Hydrodynamic diameter (nm) and zeta potential (mV) measured using DLS	174
Table S4.3 Water flux measurements of PFG-IV thin films deposited on MCE determined at specified pressure	174

Table S4.4: Parameters derived from Langmuir and Freundlich fitted models of NaFL binding isotherm to PFG-V 175

Table S4.5. Overview of reagents/processes involved in different batches of PFGs 176

## LIST OF ABBREVIATIONS AND ACRONYMS

AA	ascorbic acid
AER	anion exchange resin
Aq-SONO- ARGET ATRP- SNR	aqueous sonochemical assisted ARGET ATRP functionalization on SWCNT NanoResin
Aq-SONO-ATRP- SNR	aqueous sonochemical assisted ATRP functionalization on SWCNT NanoResin
Aq-SONO-ATRP- SS-SNR	aqueous sonochemical assisted ATRP functionalization of short strands vbTMAC on SWCNT NanoResin
Aq-SNR	aqueous single walled carbon nanostructured resin
ARGET	activators regenerated by electron transfer
$\text{AsO}_3^{3-} / \text{OH}^{-1}$	arsenic trioxide/sodium hydroxide ion of interest
ATR FTIR	attenuated Total Reflectance Fourier transform infrared spectroscopy
ATRP	atom transfer radical polymerization
$C_e$	concentration of analyte at equilibrium (mg-C/L)
$\text{CrO}_4^{2-}$	potassium chromate ion of interest
Cu/TPMA [CuBr <sub>2</sub> ]	Cu catalyst complex (CuBr <sub>2</sub> /tris(2-pyridylmethyl)amine) concentration of copper (II) bromide
DLS	dynamic light scattering
DMF	dimethyl formamide
DBP	disinfection byproduct
DTZA	diatrizoic acid
$E_a$	Arrhenius activation energy
EPM	electrophoretic mobility
%F	functionalization density
FE-SEM	Field emission-scanning electron microscope
$\gamma$	ratio between specific heat at constant pressure ( $C_p$ ) and specific heat at constant volume ( $C_v$ )
g	relative centrifugal force (rcf)
$\Delta H$	activation enthalpy
HAA	haloacetic acid

$\text{H}_2\text{AsO}_4^{1-}$ / $\text{HAsO}_4^{2-}$	arsenic (V) oxide hydrate ion of interest
HEBiB	2-hydroxyethyl 2-bromoisobutyrate
HiPCO	high pressure carbon monoxide
IEX	ion exchange
$k_{\text{app}}$	apparent propagation rate constants
$k_T$	Thomas rate constant
M	mass of adsorbent (g)
$[\text{M}]_0$	initial monomer concentration during polymerization
$[\text{M}]$	monomer concentration measured after certain polymerization duration
mg-C/L	milligrams of carbon per liter of solution
MWCO	molecular weight cut-off
NaFL	sodium fluorescein
$[\text{NaFL}]$	concentration of sodium fluorescein in the effluent
$[\text{NaFL}]_0$	initial concentration of sodium fluorescein in the feed solution
NanoResin	nanostructured resin
NOM	natural organic matter
NMR	nuclear magnetic resonance
$P_a$	pressure in the bubble at start of its collapse
PDI	polydispersity index
PFG	polymer functionalized fluorographite
PEG	poly(ethylene glycol) methyl ether
PFOA	perfluorooctanoic acid
PFOS	potassium perfluorooctanesulfonate
ppb	parts per million
ppm	parts per million
ppt	parts per trillion
$P_{\text{vapor}}$	liquid vapor pressure
q	loading or adsorption capacity (mg/g)
$q_e$	continuous flow or equilibrium adsorption capacity (mg/g)
Q	volumetric flow rate (L/min)
R	universal gas constant

$\Delta S$	activation entropy
SEC-MALS	size Exclusion Chromatography – Multi Angle Light Scattering
SEM	scanning electron microscope
SI-ATRP	surface initiated ATRP
SONO-ATRP	sonochemical assisted ATRP of vbTMAC
SONO-ATRP-I	sonochemical assisted ATRP initiation
SONO-ATRP-P	sonochemical assisted ATRP propagation
Sono-RAFT	Sonochemical assisted reversible addition–fragmentation chain transfer polymerization
SnOct	stannous octoate
SWCNT	single walled carbon nanotube
$T_{\text{bubble}}$	temperature generated at sono-cavitation bubble
$T_{\text{bulk}}$	measured bulk temperature of reaction solution
TEM	transmission electron microscope
TEMPO	2,2,6,6-tetramethylpiperidine-1-oxyl
THM	trihalomethane
TOC	Total organic carbon
TPMA	tris(2-pyridylmethyl)amine
[TPMA]	concentration of tris(2-pyridylmethyl)amine
USEPA	United States Environmental Protection Agency
vbTMAC	vinylbenzyl trimethylammonium chloride
[vbTMAC]	concentration of vinylbenzyl trimethylammonium chloride
$V_{\text{eff}}$	throughput volume (L)
$\text{VO}_4^{3-}$	sodium orthovanadate ion of interest
$\text{WO}_4^{2-}$	ammonium Tungstate ion of interest

## CHAPTER 1: Introduction

### 1.1 Background

#### 1.1.1 Water Purification

Water has always been the most life-sustaining drink to human beings and essential for the survival of all living organisms. Demand for clean and safe drinking water is a global challenge because of water scarcity, growth of human population, urbanization, and anthropogenic pollution. Clean drinking water substantially impacts human health, ecosystems and economic conditions around the world.

Table 1.1: MCL values of some emerging contaminants as reported by US EPA

Class of chemicals	Chemicals	MCL ( $\mu\text{g/L}$ )
PFAS	Perfluorooctanoic acid (PFOA)	<b>0.070</b>
	Perfluorooctane sulfonic acid (PFOS)	
DBPs	Dichloroacetic acid	60
	Dibromochloromethane	80
Pharmaceutical	Trinitroglycerol	5
Pesticides	Alachlor	2
	Carbofuran	40
	Simazine	4
Consumer products	Pentachlorophenol	1
Heavy metals	Arsenic	10
	Chromium	100
	Cadmium	5

In order to address this issue, robust water purification processes are required, which incorporate low cost and less energy, while minimizing the use of chemicals and

the impact on the environment.<sup>1</sup> Due to greater chances of water contamination in the supply systems, the US Environmental Protection Agency (EPA) is evaluating the use of a number of centralized water treatment concepts as “small system compliance technology”.<sup>2</sup> Purification of water involves removal of chemicals in the form of small hydrophilic molecules and ions from ground water or surface water reservoirs, which are addressed as “emerging contaminants” by the health advisories board that establish drinking water risk level concentrations of these contaminants. These health advisories programs sponsored by US EPA focus on the presence of molecules such as pharmaceuticals, pesticides, metalloid oxyanions, disinfection byproducts, per- and polyfluoroalkyl substances, GenX and other consumer products in natural water resources. These molecules are extremely mobile and toxic in nature, do not degrade or hydrolyze easily, and highly soluble in water which can easily result in bioaccumulation.<sup>3</sup> As the toxicology, fate, transport and bioaccumulation potential of these contaminants are widely studied and understood, health advisories have established drinking water maximum contaminant levels (MCLs) of several types of these emerging contaminants (as shown in Table 1.1).<sup>4</sup> Most of these contaminants currently exist at parts per billion (ppb) levels in the natural water resources and purification technologies are being challenged to remove PFAS down to or below 70 parts per trillion (ppt) concentration.<sup>5,6</sup>

#### 1.1.2 Processes of water purification

Conventionally, the general processes to treat water include chemical addition, coagulation, flocculation, sedimentation, and chlorine disinfection. At the end point of water treatment utilities, chlorine disinfection is performed to prevent pathogenic activity. Due to this, chlorine reacts with active humic substances present in water to give rise to

disinfection byproducts (DBPs) which further exacerbates the drinking quality of water. For safe drinking water conditions, advanced purification systems are required as the last line of defense to take care of byproducts and emerging contaminants. Water purification techniques that can be used for this purpose can be divided into adsorbent materials, flocculation/coagulation methods, nanofiltration techniques, disinfection techniques, and a special category, which integrates miniaturized materials into the formulation of sorbent nanocomposites for water purification. Various purification techniques along with their subclasses are listed in Table 1.2.<sup>7</sup>

Most of these current systems have complex deficiencies that affects their

Table 1.2: Types of Water Purification techniques

Flocculation /Coagulation	Disinfection	Filtration	Adsorption	Nanocomposites
Electro Coagulation	Photo catalytic oxidation	Reverse Osmosis	Activated Carbon	Anion exchange
Dialysis	Chemical treatment	Ultrafiltration	Ion Exchange	Cross linkers
	Sonication energy	Nanofiltration	Metal Organic Framework	Biopolymers like cellulose, starch, chitin
	Ozonation	Microfiltration	Zero Valent Iron	Functionalized nanomaterials
		Aerogels	Zeolite clay/siliceous materials	

overall performance. For instance, techniques using microfiltration or UV disinfection are not capable of removing these molecules from ground water or surface water reservoirs to meet the increasingly stringent water quality standards.<sup>8,9</sup> It is difficult to

coagulate these small hydrophilic molecules/ions, hence, coagulation and flocculation methods are not an adequate technique for removing these small molecules. It takes many hours for AC to adsorb pollutants and large quantities of AC are required. Moreover, the adsorption of emerging contaminants is negatively affected by the presence of natural organic matter (NOM) at environmentally relevant concentrations.<sup>10-</sup>  
<sup>12</sup> Regeneration of AC takes place at high temperature (800 °C) under continuous N<sub>2</sub> flow, and the initial capacity and affinity towards contaminants are not fully restored.<sup>13</sup> MIEX® and DOWEX (commercial IERs) take hours to reach ion exchange equilibrium, so they are very slow and not easily regeneratable.<sup>14</sup> Hence, all these materials have slow kinetics. These inadequacies in current water treatment processes demand for affordable, fast yet high capacity membrane technologies for water purification that are easily regeneratable. Smart point-of-use (POU) water purification systems can be used as the last line of defense to mitigate inadequacies at the public utilities' level. Smart POU systems have the ability to provide fast, high capacity solutions and straightforward control at the consumer level.

Most of these emerging contaminants are anionic electrolytes in water, thus making anion-exchange resins that employ electrostatic interactions to adsorb these anions as the most suitable candidate of all the current purification techniques. The performance of interface related processes (i.e., adsorption) is strongly dependent on surface area.<sup>15</sup> Nanomaterials have been promising materials for next generation water purification systems due to ultra-high specific surface area resulting in greater amount of material in contact with the surrounding, and higher reactivity.<sup>16</sup> Based on this high surface reactivity, nanomaterials can be easily surface functionalized to target the

emerging contaminants of interest. This research dissertation is focused on nano assisted ion exchange systems which integrates nanomaterials as scaffolds to facilitate anion exchange-based adsorption of emerging contaminants for water purification.

### 1.1.3 Nanomaterials for water purification

Nanomaterials have generated widespread scholarly interests in the field of water purification. As mentioned above, they are excellent candidates for adsorbents due to their small size and high specific surface area or high porosity. Nanomaterials are not only capable of removing contaminants with varying size, hydrophobicity/fluorophilicity, and morphology but can also increase the effectivity of purification per mass of raw material when used as a scaffold.<sup>17</sup> Nanoadsorbents/nanocomposites support faster kinetics and overall higher adsorption capacity due to an increased number of active interaction sites at the surface. Apart from this, they possess superior catalytic potential and high reactivity, which make the active sites more dynamic compared to active sites of conventional sorbent materials. It is difficult to implement green chemistry in the design of nanocomposites but if achieved, it would lead to sustainable and affordable solutions. The intrinsic properties and calculated design will help us attain the required pretotype for achieving potable thin film systems for water purification.

However, there are some challenges when using nanomaterials for water purification purposes which include concerns regarding the fate of the nanomaterials and administrative/regulatory challenges.<sup>18</sup> All these nanomaterials have different applications in water and wastewater treatment due to the structural and morphological

Table 1.3: Overview of advantages and disadvantages of various nanomaterials when acting as scaffolds for water/wastewater purification/treatment processes

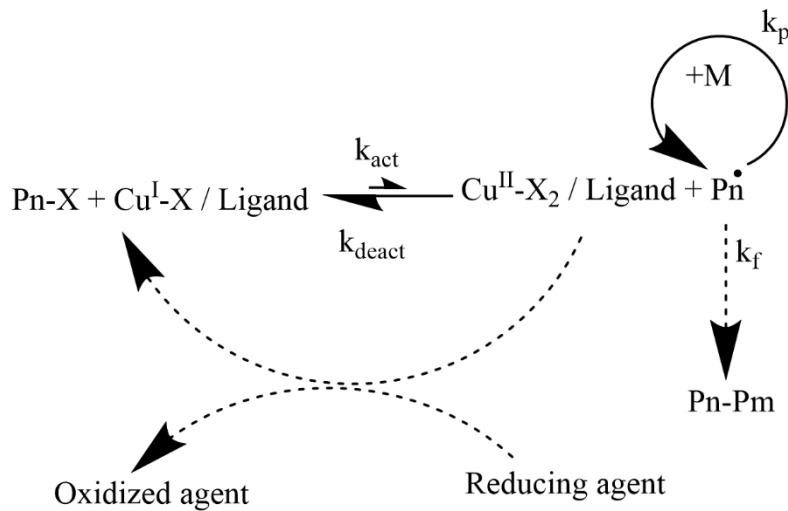
Nanomaterials	Advantages	Disadvantages
Carbon Nanotubes <sup>1,2</sup>	<ul style="list-style-type: none"> <li>• Extremely good structural integrity</li> <li>• High water flux</li> <li>• High percent removal</li> <li>• Highly reusable</li> <li>• High surface reactivity</li> </ul>	<ul style="list-style-type: none"> <li>• Cost of raw material is high</li> </ul>
Graphene <sup>3,4</sup>	<ul style="list-style-type: none"> <li>• Affordable</li> <li>• High percent removal</li> <li>• Highly reusable</li> </ul>	<ul style="list-style-type: none"> <li>• Low water flux</li> <li>• Low reactivity</li> </ul>
Biopolymers (cellulose, chitin, etc.) <sup>5</sup>	<ul style="list-style-type: none"> <li>• Biodegradable</li> </ul>	<ul style="list-style-type: none"> <li>• Low surface reactivity</li> </ul>
Nano-TiO <sub>2</sub> /Photolysis	<ul style="list-style-type: none"> <li>• Affordable</li> <li>• Highly reactive</li> </ul>	<ul style="list-style-type: none"> <li>• Needs photocatalytic activation/needs energy consumption<sup>7</sup></li> <li>• Low water flux</li> <li>• Limitation of removal at low concentration<sup>8</sup></li> </ul>
Magnetic nanocomposites <sup>9</sup>	<ul style="list-style-type: none"> <li>• Rapid separation</li> <li>• Chemicals stability</li> </ul>	<ul style="list-style-type: none"> <li>• Need external magnetic field</li> </ul>
Zeolites <sup>5</sup>	<ul style="list-style-type: none"> <li>• Uniform porosity</li> <li>• Microporous</li> </ul>	<ul style="list-style-type: none"> <li>• Not designed for fast filtration</li> </ul>
Metal Organic frameworks <sup>10</sup>	<ul style="list-style-type: none"> <li>• Modulation of pore size</li> <li>• Different surface functionality</li> <li>• Microporous</li> </ul>	<ul style="list-style-type: none"> <li>• Unstable in harsh conditions</li> <li>• Regeneration and reusability challenge under mild conditions</li> <li>• High cost of fabrication</li> </ul>

characteristics as mentioned in Table 1.3. Applications comprise desalination, ion-exchange bed filtration, ultrafiltration and membrane water purification.

My research goal is to form water purification modalities that allow high accessible surface area rendering fast, easy, and high percent removal of contaminants, and support low transmembrane resistance which is achievable primarily using thin films assemblies. This research study focuses on the green and sustainable synthesis of these nanocomposites to achieve sustainable materials to reduce the toxic payload of nanomaterials into the environment and provide safe drinking water.

### 1.2 Activator regenerated by electron transfer assisted atom transfer radical polymerization (ARGET ATRP)

One of the industrially relevant procedures to synthesize hydrophilic brushes of anion exchange resins is via atom transfer radical polymerization (ATRP).<sup>19-23</sup> This procedure ensures continuous activation and deactivation of alkyl chain radicals to achieve well-defined polymers having a controlled growth rate.<sup>24,25</sup> During ATRP, an initiator in the form of alkyl halide or dormant species (initiator RX or polymeric initiator PX) are activated by transition metal complex in lower oxidation state that produces alkyl radicals or propagating radicals ( $R^{\bullet}/Pn^{\bullet}$ ) and higher oxidation state transition metal



Scheme 1.1: Mechanism of ARGET ATRP

complex with coordinated halide ligands (i.e., deactivator complex) (as shown in Scheme 1.1).<sup>25,26</sup> This process takes place reversibly with a rate constant of activation ( $k_{act}$ ) or deactivation ( $k_{deact}$ ). The halide group must quickly migrate between growing chain species and transition metal complex. The resulting alkyl radical then attacks and adds to the end of the growing polymer with a propagation rate constant,  $k_p$ .<sup>24</sup> Initiation should be rapid and the equilibrium rate constant ( $K_{ATRP} = K_{act}/K_{deact}$ ,  $K_{ATRP} \ll 1$ ) should be small (i.e., shifting the equilibrium towards the dormant species) to ensure the uniform initiation and growth of the polymer strands, and the minimization of possible bimolecular terminations of active polymer chains.<sup>20,22,24</sup> The ATRP rate law is indicated in the following equation 1:

$$R_P = k_p[M][P^*] = k_p[M]K_{eq}[I]_0 \frac{[Cu^I]}{[X - Cu^{II}]}$$

where  $k_p$  is rate constant of propagation;  $[M]$ , and  $[I]_0$  are concentrations of monomer and initiator, respectively, and  $[Cu^I]/[X-Cu^{II}]$  is the molar ratio of activator to deactivator.<sup>27</sup>

ARGET ATRP in water is a result of high catalytic activity rendering poor control on polymerization. One of main factors could be high  $K_{ATRP}$  constant value in water which in turn generates high number of propagating radicals and increases rate of termination. There is complication of dissociation of halide from the deactivator complex with poor control on deactivation of propagating radicals. To minimize unwanted radical processes, these reactions typically use large quantities of catalyst, with concentrations of 20,000 to 45,000 ppm in order to lower the  $[Cu^I]/[X-Cu^{II}]$  ratio and thereby to avoid chain termination processes. This use of high catalyst concentration is wasteful, generating metal byproducts that must be cleaned out and discarded at the end.<sup>19,27</sup> By

incorporating activator regenerated by electron transfer (ARGET) technique in ATRP, one can regenerate the Cu(I) complex using a reducing agent (tin(II) 2-ethylhexanoate (SnOct) or ascorbic acid (AA)). Therefore, the concentration of catalyst complex can be lowered to ~10 ppm. Moreover, the regeneration of the Cu(I) activating complex results in a less toxic payload to the environment. This has been a great paradigm for introduction of green chemistry in ATRP processes in the form of ARGET-ATRP. We have synthesized short strands of polyelectrolyte brushes of vinylbenzyl trimethylammonium chloride (vbTMAC) having taken advantage of ATRP (or ARGET ATRP) environment to functionalize grown polymer radicals on various carbon nanostructures.

### 1.3 Green Chemistry, Synthesis and Functionalization

Green chemistry broadly includes innovative measures to maximize the desired end product while using greener solvents and environmentally benign reagents.<sup>28</sup> Since my main goal is to formulate water purification systems, it is necessary to use eco-friendly reagents to build safe and sustainable water purification systems. Pioneering work for synthesizing nanocomposites for water purification in our lab was done previously using an organic solvent, N,N dimethylformamide to produce good dispersions of carbon nanostructures but this is a toxic and expensive solvent.<sup>14</sup> In Chapter 1, we eliminated the use of organic solvents to synthesize and functionalize polyelectrolyte strands of vbTMAC on Single Walled Carbon Nanotubes (SWCNTs) (Aq-SNR) using ARGET ATRP technique.<sup>29</sup> This process allows easy and clear dispersion of functionalized SWCNTs in water which otherwise would not be possible. These polyelectrolyte brushes form a conformal coating around SWCNT with a ~10 nm

cross-section, allowing an open structure exposing most of the active sites for rapid adsorption of anionic contaminants of different sizes and hydrophilicities.<sup>29</sup>

### 1.3.1 Green Synthesis and functionalization using Sonochemistry

In a recent work, Matyjaszewski et al. demonstrated usage of ultrasonic bath (110 W, 40 kHz) to mediate aqueous ATRP (SONO-ATRP) without use of any additional conventional initiators or reducing agents with 40-4000 ppm levels of Cu/TPMA. The proposed mechanism generated hydroxyl radicals from sonolysis of water in aqueous medium which is capable of regenerating deactivator species and hence, replacing the role of reducing agent, which is required in the ARGET ATRP mechanism.<sup>30</sup> However, this work did use a macroinitiator for initiating the polymerization and employed mixture of ethanol/water as synthesis media to form carbon radicals from ethanol for efficient generation of Cu(I) species rather than just hydroxyl radicals. In Chapter 2, I demonstrated the first reported synthesis of SONO-ATRP assisted polyelectrolytes of vbTMAC and their subsequent functionalization onto pristine SWCNT using only water as a solvent and without the use or need of any initiators, reducing agents and at catalyst loading <5 ppm using sonication probe (144 Wcm<sup>-2</sup>, 20 kHz).<sup>31</sup> When ultrasonic waves propagate through water, they cause the formation of cavitation bubbles that are filled with water vapor and dissolved gas molecules and eventually induce strong vibrations of these microbubbles. These sonic vibrations cause compression of bubbles in short lived adiabatic phenomena that leads to generation of highly localized inhomogeneous high temperatures (4000 – 5000 °C) and high pressures (> 500 atm) within the bubble and >1200 K at the interfacial region between bulk media and the bubble. These conditions are harsh enough for water splitting which leads to hydrogen and hydroxyl (H/OH)

radicals.<sup>32,33</sup> The hydrogen/hydroxyl (H/OH) radicals generated during the sonolysis of water react with vBTMAC to efficiently produce carbon radicals, which are capable of initiating radical polymerizations.<sup>32</sup> These generated carbon radicals can also regenerate the Cu(I) activating complex from deactivating Cu(II) complex, which replaces the role and eliminates the need of the reducing agent often used duringARGET-ATRP.<sup>30</sup> This research study not only focused on green SONO-ATRP, but also demonstrated faster polymer growth kinetics and high chain-end functionalization onto the SWCNT surface (at low temperatures), thus, redefining Aq-SNR for water purification applications.<sup>31</sup>

### 1.3.2 Green functionalization using functional 2D materials

Even though SWCNTs form excellent nanostructured composites, the cost of raw material is high (up to \$1000/g). There is a need for cost-effective alternatives to nano-scaffolds that support green chemistry processability. Graphene has been widely used in drinking water purification technologies due to its exceptional mechanical<sup>34</sup> and chemical stability, large specific surface area and nano-assembly capability into multi-layer laminate thin films, which is beneficial to possible tortuosity and transport of water channels. However, it has strong hydrophobicity along with chemical inertness. Researchers have modified surface of graphene to form graphene oxide (GO) and reduced graphene oxide to increase reactivity. Hummers and Offeman achieved oxidation of graphene to form GO within few hours using  $\text{NaNO}_3$  and  $\text{KMNO}_4$  dissolved in concentrated  $\text{H}_2\text{SO}_4$ .<sup>35</sup> Furst et al. demonstrated chemical reduction of GO by hydrazine or hydrazine hydrate.<sup>36</sup> These highly toxic and lethal compounds are harmful to the environment and cannot be used as precursors for sustainable and safe drinking water purification systems. Thus, alternative graphene derivatives are required to allow

easy green processability and achieve high functionalization to remove target contaminants.

#### 1.3.2.1 Fluorographite

Fluorographene has emerged as a potential graphene derivative that is widely used in various applications like corrosion resistant coatings<sup>37</sup> thermoelectric devices,<sup>38</sup> supercapacitors,<sup>39</sup> biosensing,<sup>40</sup> solar cells,<sup>41</sup> organic field effect transistors,<sup>42,43</sup> etc. Although the C-F bonds have high chemical stability,<sup>44</sup> due to low lying  $\sigma^*$  orbital of tertiary C-F bond they do react as an electrophiles.<sup>45</sup> Studies have shown that the defluorination of fluorographene follows an  $S_N2$  nucleophilic substitution mechanism. Additionally, the generation of spin centers/radical centers (fluorine vacancies) due to radical addition mechanisms from the solvent or from the presence of electron rich species, has been shown to facilitate defluorination.<sup>45-48</sup> Radical centers on fluorographite can interact with electron rich or electron donating species. Delocalization of spin centers, due to the presence of C-F  $\sigma^*$  orbitals in the neighboring atoms, can stabilize these Singly Occupied Molecular Orbitals (SOMO).<sup>45</sup> These defects can act as the initiation sites of defluorination which eventually increase upon reaction with electron rich species. Baumgartner et al. postulated that the byproduct of defluorinated fluorobenzene, under aqueous conditions, is the fluoride anion.<sup>49</sup> Hence, the defluorinated carbon will carry slightly positive charge due to highly electronegative fluorine atoms bound to neighboring carbon atoms. These sites are potential centers for polyelectrolyte radical attack and subsequent covalent attachment. The number of spin centers increase during the reaction, resulting in a well functionalized PFG resin material. It has been demonstrated in previous research works that the defluorination and

delocalization of spin centers gave rise to cascade of C=C bonds (or  $\pi$  conjugated regions) in fluorographite.<sup>45,46</sup> We have observed similar behavior as discussed in the results section below. In my third research study, I demonstrate facile defluorination and covalent attachment of poly(vbTMAC) on fluorographite (PFG) in aqueous medium. The physicochemical properties of these materials have been extensively explored to understand the morphology of these materials. PFG resins provide an efficient platform for tailoring graphene derivatives with high degree of functionalization for water purification.

#### 1.4 Structure-property-function relationships through characterization and water purification testing

Property and performance of a nanocomposite are dependent on structure, dimensionality, and arrangement of nanomaterials. Water flux can be measured from the following equation:  $J_w = \frac{Q}{AP\Delta t}$  where  $J_w$  is water flux (permeability) ( $L\ m^{-2}h^{-1}bar^{-1}$ ),  $Q$  is volume of water (L),  $A$  is the surface area of the layers or film ( $m^2$ ),  $P$  is the pressure (bar) and  $\Delta t$  is the time (h) required for volume  $L$  to flow through. Pore distribution and cylindrical capillary pore diameter of the membranes affect the liquid flow through these channels as per Poiseuille's law:  $J = N \frac{\pi d^4}{128\mu l} \Delta p$  where  $N$  is the total number of pores per square centimeter of membrane,  $d$  is pore diameter,  $\Delta p$  is pressure difference across pore,  $\mu$  is liquid viscosity and  $l$  being pore length. This equation can be simply modified to:  $J = \frac{\Delta p \epsilon}{32\mu l} d^2$  where  $\epsilon$  is the number of pores per square centimeter.<sup>50</sup> Since,  $J$  is directly proportional to pores per unit area and pore diameter, water flux of different structures and arrangements of nanomaterials will be different. If the pore diameter is less, then the

pore density should be high to maintain high water flux and vice versa. But having large pores will restrict the effectivity of percent removal capacity. Jang et al. created uniform pore densities ( $\sim 10^{13} \text{ cm}^{-2}$ ) on graphene monolayer to create nanopores (0.25 nm) via ion bombardment and oxygen plasma etching. They achieved a water flux of 13  $\text{L m}^{-2}\text{h}^{-1}\text{bar}^{-1}$  which is equivalent to  $3.6 \times 10^{-8} \text{ m kPa}^{-1}\text{s}^{-1}$  that rejected 98% of  $\text{MgSO}_4$ .<sup>51</sup> A 4-layered self-assembly of spherical Au nanocrystals functionalized with dodecanethiol ligand (34 nm thick) resulted in water flux of  $10^{-6} \text{ m kPa}^{-1}\text{s}^{-1}$  at 82 kPa with a pore diameter of 1.7 nm.<sup>52</sup> This material exhibited size dependent rejections of molecules at high analyte concentrations ( $\sim 1 \text{ mg/ml}$ ) and achieved 10% rejection for small ( $< 1.6 \text{ nm}$ ) uncharged molecules, 45–60% rejection for small charged molecules and 99% for molecules larger than 1.7 nm.<sup>52</sup> Our thin film assemblies in the form of short strand polyelectrolyte functionalized SWCNT resin (Aq-SNR) have the greatest advantage in terms of scaffold robustness, defect tolerance and extreme tortuosity leading to high water flux of  $1680 \text{ L m}^{-2}\text{h}^{-1}\text{bar}^{-1}$  (for a mass density of  $0.90 \text{ mg cm}^{-2}$ ) which is equivalent to  $4.67 \times 10^{-6} \text{ m kPa}^{-1}\text{s}^{-1}$  for a thickness of few  $\mu\text{m}$ . If we assume the top monolayer of Aq-SNR has spherical pores, then the pore diameter was estimated to be in the range of 20 – 150 nm (measured from SEM image of Aq-SNR using ImageJ software) which fall within the porosity of ultrafiltration membranes. Short strands polymer functionalized fluorographite (PFG) resins exhibited high water flux of  $510 \text{ L m}^{-2}\text{h}^{-1}\text{bar}^{-1}$  (for a mass density of  $0.70 \text{ mg cm}^{-2}$ ) which is equivalent to  $1.4 \times 10^{-6} \text{ m kPa}^{-1}\text{s}^{-1}$  for a thickness of 2.9  $\mu\text{m}$ . PFG resins exhibited stacked assembly of non-uniform crystallite sized plate-like morphology similar to exfoliated fluorographite with amine functionalities.<sup>53</sup> Our materials are designed to remove hydrophilic small

molecules at environmentally relevant concentrations. It is more challenging to achieve significant removal of contaminants at very low concentrations ( $\mu\text{g L}^{-1}$ ). We achieved >95% removal of emerging contaminants with initial concentration of 2 – 4 mg –  $\text{C L}^{-1}$  using Aq-SNR and obtained >99% removal of emerging contaminants with initial concentrations of 80-220  $\mu\text{g L}^{-1}$  using PFG resins. Aq-SNR and PFG have different architectures that facilitate high water flux and high percent removal of contaminants compared to presence of uniform micropores. The closely packed short strand polyelectrolytes act as a conduit for providing permeable pathways for water channels in the layers below. The functionalized architecture allows for longer tortuous path lengths that periodically brings hydrophilic small contaminants in close proximity to the anion exchange quaternary ammonium binding sites for contaminant adsorption - leading to maximum removal<sup>54</sup> even under low initial concentrations. All materials that employ adsorption-based purification will eventually become ineffective as the available and accessible binding sites become exhausted. Aq-SNR and PFG, both exhibit facile regeneration capabilities due to open resin mechanism.

## CHAPTER 2

### GREEN SYNTHESIS OF NANOSCALE ANION EXCHANGE RESIN FOR SUSTAINABLE WATER PURIFICATION

Abhispa Sahu, Kayla Blackburn, Kayla Durkin, Tim B. Eldred, Billy R. Johnson, Rabia Sheikh, James E. Amburgey, and Jordan C. Poler

#### Citation

Sahu, A.; Blackburn, K.; Durkin, K.; Eldred, T. B.; Johnson, B. R.; Sheikh, R.; Amburgey, J. E., Poler, J. C. Green synthesis of nanoscale anion exchange resin for sustainable water purification. *Environ Sci-Wat Res Technol.* **2018**, *4* (10), 1685-1694  
10.1039/c8ew00593a

#### KEYWORDS

Water purification, NOM removal, adsorption, ion-exchange, SWCNT, poly(vbTMAC), kinetics, disinfection byproducts

## Abstract

The challenge of providing safe and reliable drinking water is being exacerbated by accelerating population growth, climate change, and the increase of natural and anthropogenic contamination. Current water treatment plants are not effective at the removal of pervasive, hydrophilic, low molecular weight contaminants, which can adversely affect human health. Herein, we describe a green all-aqueous synthesis of an ion exchange resin comprised of short chain polyelectrolyte brushes covalently bound to single walled carbon nanotubes. This composite material is incorporated onto a membrane and the active sites are tested against analyte adsorption. Our control studies of water or brine pushed through these materials, found no evidence of single-walled carbon nanotubes (SWCNTs) or carbon/polymer coming out of the membrane filter. We have measured the adsorption capacity and percentage removal of ten different compounds (pharmaceuticals, pesticides, disinfection byproducts and perfluoroalkylated substances). We have measured their removal with an efficiency up to 95% – 100%. The synthesis, purification, kinetics, and characterization of the polyelectrolytes, and the subsequent nanoresin are presented below. The materials were tested as thin films. Regeneration capacity was measured up to 20 cycles and the material has been shown to be safe and reusable, enabling them as potential candidates for sustainable water purification.

## Introduction

The US Environmental Protection Agency (USEPA) is focused on the monitoring and removal of many classes of compounds from drinking water and wastewater including; disinfection byproduct (DBP) precursors, pharmaceuticals, personal care products, heavy metals, and per- and polyfluoroalkyl substances (PFAS).<sup>1</sup> These pervasive substances are related to adverse human health conditions and they are persistent in the environment. Under environmental conditions, PFAS do not hydrolyze, photolyze or biodegrade and hence, are extremely persistent in the environment.<sup>2</sup> It is becoming increasingly difficult for water treatment facilities to remove molecular contaminants at the limits set by the USEPA (e.g., PFAS 70 ppt, 80 ppb for trihalomethanes (THM) and 60 ppb for haloacetic acids (HAA)).<sup>3</sup> Possible health risks from prolonged exposure include; kidney, liver, and central nervous system issues, as well as cancer.<sup>4-5</sup> Many water utilities rely solely on coagulation as the means of lowering the levels of molecular contaminants; however, this is not as effective a method for low molecular weight and hydrophilic compounds. Activated carbon is the most widely used adsorbent material, but it comes with a high operating cost.<sup>6</sup> With natural and anthropogenic contaminant levels rising in drinking water sources worldwide, there is a significant increase in demand for more efficient removal.<sup>7-11</sup> In general, there are a large number of compounds, across many chemical classes, that are naturally occurring in surface water. Many others are anthropogenic, and released into the environment due to improper treatment of wastewater. All drinking water sources contain natural organic matter (NOM), which can become DBPs during required water treatment processes. In our previous work we have demonstrated that our ion exchange nanomaterials can

remove (NOM) faster, and at a higher capacity than other methods and materials currently deployed.<sup>12</sup> Since the publication of those results, we have optimized the materials and processes and here show that we can also remove other classes of compounds from water. Specifically, we demonstrate the removal of several types of pharmaceuticals (*viz.*, tetracycline and carbenicillin), pesticides (*viz.*, bentazon, terbacil, and bromacil), DPBs (*viz.*, bromoacetic acid and chloroacetic acid) and PFAS (*viz.*, perfluorooctanoic acid (PFOA) and perfluorooctanesulfonate (PFOS)), from water. We have synthesized these nanoresin materials using a green all-aqueous process.

Use of pristine nanostructured carbons in a synthesis typically requires a good dispersant to stabilize the nanoparticles. Often these dispersants are aprotic polar solvents like N,N-Dimethylformamide (DMF) or N-Methyl-2-pyrrolidone (NMP) which are both toxic and expensive. We have eliminated all organic solvents from our green all-aqueous synthesis of functionalized nanostructured carbon using the activators regenerated by electron transfer – atom transfer radical polymerization (ARGET – ATRP) method. Aqueous ARGET-ATRP reactions are complicated by multiple issues. The activation constants for initiators tend to be over an order of magnitude higher in water than in organic solvents.<sup>13-14</sup> This leads to an increase in ATRP polydispersity which is inversely proportional to the ratio of active to inactive chains.<sup>15</sup> In addition, changes in pH can lead to further complications such as the protonation of the catalyst. We have optimized a process that maintains low polydispersity during this all-aqueous synthesis of shortchain strong-base ion-exchange polymers. We have covalently functionalized these linear non-crosslinked polyelectrolytes to pristine SWCNTs using the same all-aqueous ARGET ATRP process. These short brush-like polyelectrolytes

form a conformal coating around the SWCNT resulting in a nanoresin with a ~10 nm cross-section, allowing access to all of the binding sites without being diffusion limited. The cationic nature of the polymer allows the nanoresin to be readily deployed in aqueous systems. This then promotes rapid adsorption of a broad spectrum of contaminants from drinking water or wastewater.

We have synthesized these nanoresins, using the ARGET-ATRP method where the reaction follows a living radical propagation mechanism. This method is preferable to traditional ATRP because of the reduced transition metal catalyst required and the increased control of the polydispersity.<sup>16</sup> The catalyst concentration can be kept to a minimum by using a reducing agent. A common ATRP catalyst is the Cu(I)-Br/TPMA complex (TPMA is tris(2-pyridylmethyl)amine). This is a very reactive complex in water and the use of a reducing agent is required for control of the reaction. A low ratio of the Cu(I) to Cu(II) form of the catalyst (activator/deactivator) is required for ATRP in water to reduce radical concentrations and maintain control of the polymerization.<sup>16</sup> Rapid addition of a reducing agent pushes the catalyst too far toward its activator form leading to poor polymerization control. Often ascorbic acid is added slowly to regenerate the catalyst. Here we describe a way to maintain the reducing agent concentration by using tin(II) 2-ethylhexanoate in the aqueous reaction. Sn(II) in water exists in many species but the Sn(OH)<sub>2</sub>(aq) form is prevalent at the pH range and ionic strength of our reaction,<sup>17-18</sup> and the K<sub>sp</sub> of Sn(OH)<sub>2</sub>(s) is 5.45x10<sup>-27</sup>. As the reducing agent reacts to reactivate the catalyst, the Sn<sup>2+</sup> oxidizes to Sn<sup>4+</sup>, but the concentration of the reducing agent stays constant throughout the reaction due to the slow dissolution of the Sn(OH)<sub>2</sub>(s) back into the reaction solution. This enables a constant regenerator concentration, which

in turns maintains a constant activator/catalyst concentration and thereby a constant rate of polymerization.

This paper describes a green synthesis of a polyelectrolyte modified nanostructured carbon material. We show outstanding adsorption loading and fast adsorption kinetics for several class of water contaminants. These materials are also regeneratable and reusable such that they enable a sustainable new material for water purification.

## 2.1 Synthetic Methods

2.1.1 Materials and Methods. All reagents were used as purchased without additional purification or modification. HiPCO (Grade P CNT, 0.8-1.2 nm diameter, 100-1000 nm length; Lot # P0276) SWCNTs were used. Polymer synthesis was based on: vinylbenzyl trimethylammonium chloride (vbTMAC) (Fisher, 97%; Lot # A0311318) monomer, copper(II) bromide (Acros, 99+%; Lot # A0344238), tris(2-pyridylmethyl)amine (TPMA) (TCI, >98.0%; Lot # Z8GMO-AD) for the catalyst, tin(II) 2-ethylhexanoate (Sigma-Aldrich, 92.5-100%, Lot # SLBP5072V) for the reducing agent, 2-hydroxyethyl 2-bromo-isobutyrate (HEBiB) (Sigma-Aldrich, 95%, Lot # MKBW2607) initiator. Other analytes include: D-(+)-glucose (Sigma, Lot # 89H0150), toluene (HPLC grade, lot #), perfluorooctanoic acid (Aldrich, Lot #MKCC6736), Potassium perfluorooctanesulfonate, 98% (Matrix Scientific, Lot #M22Q), tetracycline hydrochloride (Fisher BioReagents®, Lot #106895-36), carbenicillin disodium (Fisher Scientific, Lot #148020), Bentazon (Ultra Scientific, Lot# NT059639), Bromacil (Ultra Scientific, Lot# NT053779), Terbacil

(Ultra Scientific, Lot# NT059638), Bromoacetic acid (99%: Acros Organics, Lot# 106572500), and Chloroacetic acid (99%: Lot B0143934) and sodium fluorescein (Sigma, Lot# BCBR1213V).

2.1.2 Workup of the synthesis required: polypropylene membrane filters (0.45  $\mu\text{m}$  pore size, 47 mm wide, Lot #2075-5), Nitrocellulose Mixed Ester (MCE) (Sterlitech Corp., Lot. # 31127255) with 0.45  $\mu\text{m}$  pore diameter and 13 mm width, Whatman Anotop Sterile syringe filter (25 mm, 0.02 micron pore size, Cat. No. # 68092102), 12 KDa molecular weight cutoff (MWCO) dialysis membrane (Thermo Fisher Scientific, Lot. # AD-8099-2) 45 mm width and 28.6 mm diameter, 2 kDa MWCO dialysis membrane (Spectrum Labs, Lot. #3294218) 45 mm flat width and 29 mm diameter, and 50 kDa MWCO dialysis membrane (Spectrum Labs, Lot. #3292110) 34 mm flat width and 22 mm diameter. Membranes were activated by incubated for 10 minutes in Milli-Q water with constant stirring.

2.1.3 Aqueous Synthesis of vbTMAC polyelectrolytes. Polymerization was performed using a Schlenk apparatus under a positive pressure of Ar(g). TPMA (6.32 mg, 21.8  $\mu\text{mol}$ ) and an aqueous CuBr<sub>2</sub> solution (17.24  $\mu\text{L}$ , 20.6 mM, 0.35  $\mu\text{mol}$ ) were added into 1.0 mL of Milli-Q water to form the catalyst complex. Additional Milli-Q water (15.1 mL), vbTMAC (1.60 g, 7.57 mmol) were added and fully dissolved. The reaction mixture was sparged with Ar(g) for 20 minutes. HEBiB (10.3  $\mu\text{L}$ , 71.0  $\mu\text{mol}$ ) was then added. Tin(II) 2-ethylhexanoate (6  $\mu\text{L}$  - 60  $\mu\text{L}$ ) was added and the reaction flask heated in a 110  $^{\circ}\text{C}$  oil bath under reflux conditions for the duration of the reaction. 300  $\mu\text{L}$  aliquots were taken for <sup>1</sup>H NMR analysis throughout the reaction. To reach 95% conversion of the monomer, the reaction proceeds for 4158 min and is then cooled and exposed to air to

terminate the polymerization. The mixture was centrifuged at 100,000 RCF for 1 h at 20 °C to remove the thick polymer pellet. The polymer was dissolved in water and then dialyzed against Milli-Q water through a 2 kDa MWCO cellulose dialysis membrane to remove remaining monomer and other reagents. Up to eight dialysis iterations were performed until the monomer was no longer detected in the dialysate. vbTMAC is easily detected to < 1mg/L by measuring the UV-Vis absorption peak at 254 nm.

2.1.4 Aqueous Synthesis of functionalized SWCNT nanoresin (Aq-SNR). Polymerization was performed using a Schlenk apparatus under Ar(g). TPMA (6.59 mg, 22.7  $\mu\text{mol}$ ) and CuBr<sub>2</sub> solution in water (17.3  $\mu\text{L}$ , 20.6 mM, 0.35  $\mu\text{mol}$ ) were dissolved into 1.0 mL of Milli-Q water. Additional Milli-Q water (15.1 mL), vbTMAC (1.61 g, 7.62 mmol) and were added and fully dissolved. The reaction mixture was degassed with Ar(g) for 20 minutes. HEBiB (10.3  $\mu\text{L}$ , 71.0  $\mu\text{mol}$ ) was then added, Tin(II) 2-ethylhexanoate (6  $\mu\text{L}$  - 60  $\mu\text{L}$ ) was added and the reaction flask heated in a 110 °C oil bath for the duration of the reaction. 300  $\mu\text{L}$  samples were taken for <sup>1</sup>H NMR analysis throughout the reaction. DMF is added to the reaction (1% by volume) as an internal standard to quantify the remaining vinylic protons measured in the <sup>1</sup>H NMR spectra.

After 10 min, SWCNT (30.3 mg HIPCO) were added to a 5.0 mL aliquot of the reaction mixture. This mixture contained very short ionomers that were then sonicated with the SWCNTs to disperse the tubes into the polymer solution (15 min, 10 W<sub>RMS</sub>) followed by ten min sparge under Ar(g). The SWCNT dispersion was added back into the polymerization reaction (40 min from the start of the polymerization, and a 33% conversion of monomer). The reaction was kept at reflux under Ar(g) until completion (typically from 2 h or up to three days for 99% conversion of any remaining vbTMAC

monomer). The reaction was cooled and exposed to air to quench the catalyst. SWCNTs do not disperse into water without the polymer present. The polyelectrolyte strands act as a surfactant and stabilizes the SWCNT dispersion which enable subsequent covalent functionalization of polymer to the nanotubes in an aqueous reaction.

2.1.5 Purification of as-synthesized Aq-SNR is required for the removal of unreacted monomer, other reaction reagents, and all non-covalently bound polymer strands. We have shown previously that these polyelectrolytes will wrap around the SWCNTs leaving them stable in water.<sup>12</sup> By increasing the ionic strength of the solution, the surfactant is screened from the SWCNT surface and the SWCNTs aggregate as the non-covalently bound polymer is removed. NaCl(s) was added to the reaction mixture to bring the concentration to 4 M. The reaction mixture was sonicated to disperse the product and mechanically disrupt the physisorbed polymer from the SWCNTs (15 min, 10 W). The attachment processes has not been optimized for atom efficiency. Moreover, since this is a fundamental study, only a small amount of SWCNTs are used for each batch and most, ~95% of the polymer is not used. Future studies with less expensive nanostructured carbons will optimize the atom efficiency. HCl(aq) was added to dissolve residual Sn(OH)<sub>2</sub>(s) from the material. The dispersion was centrifuged (100,000 RCF, 60 min) in the high ionic strength solution. Desorbed polymer strands remain in the supernatant while the Aq-SNR collects in the sediment. Unbound polymer and other residual molecular and ionic species, are decanted and properly disposed of in hazardous waste (See Supporting Information Figure S2.1). This procedure was repeated until the unbound polymer concentration was below our detection limit as measured by UV-Vis absorption where  $\epsilon_{254} = 0.00628 \pm 0.0004 \text{ (mg-C/L)}^{-1} \text{ cm}^{-1}$ , yielding a minimum

detection limit of  $< 0.2 \text{ mg-C/L.}$ ) as shown in Figure 2.1. Dialysis was used to remove the remaining  $\text{NaCl(aq)}$  from the sample, (multiple replicates, 75 mL internal volume, into 1000 mL external volume, through a 50 kDa membrane) (as shown in Figure S2.2). Conductivity of the dialysate was used to monitor removal of the brine until the conductivity was  $\kappa < 1 \mu\text{S cm}^{-1}$ . The final Aq-SNR product was dispersed into Milli-Q water. The concentration of SWCNTs was measured by UV-Vis-NIR. The total mass concentration was measured by filtering a known volume of the Aq-SNR dispersion using a  $0.45 \mu\text{m}$  pore size polypropylene membrane filter, which retained all of the nanoparticles. The thin film was washed with methanol then dried under vacuum at  $T = 65 \text{ }^\circ\text{C}$  overnight. The mass of the Aq-SNR deposited onto the membrane was measured by subtracting off the initial mass of polypropylene membrane. Concentrations are reported in  $\text{mg Aq-SNR / L}$  of dispersion. Synthesis and cleanup of Aq-SNR did not use any organic solvents (Green Chemistry Principle 3,4, and 5).<sup>19</sup>

## 2.2 Characterization Methods

2.2.1 Kinetics of polymer growth. Polymerization kinetics were measured by monitoring monomer concentration versus time as determined by  $^1\text{H}$  NMR analysis. Standard polymer synthesis (1.50 g, 7.10 mmol vbTMAC) were monitored by pulling 300  $\mu\text{L}$  aliquots as a function of time. For each aliquot of reaction mixture, 200  $\mu\text{L}$  was mixed into 500  $\mu\text{L}$   $\text{D}_2\text{O}$ . Proton spectra taken on a 500 MHz  $^1\text{H}$  NMR (32 scans, 40 second relaxation time) and baseline corrected. To quantify the relative concentration of monomer, the vinylic protons of the vbTMAC at 5.8 ppm and 5.3 ppm were compared to the singlet at 7.77 ppm (internal standard DMF methyl protons). Integrated areas decrease in value relative to the internal standard as the monomer was polymerized. The

percent conversion for each aliquot was calculated accordingly. Loss of vinylic protons during polymerization is illustrated in Figure S2.3. Percent conversion versus time is illustrated in spectra in Figure S2.4 and pseudo first order  $\ln([M]_o/[M])$  vs. time in Figure S2.5.

2.2.2 UV-Vis-NIR Spectroscopy. Concentration and yield of the Aq-SNR was measured using UV-Vis-NIR spectroscopy. The concentration of SWCNT was measured using the absorption at 925 nm, with an extinction coefficient of  $0.0206 \text{ (mg/L)}^{-1} \text{ cm}^{-1}$ . From the total volume of dispersion and the concentration of SWCNTs determined from characteristic UV-Vis-NIR absorption, the mass of the functionalized SWCNTs was calculated. The polyelectrolyte strands do not absorb at this wavelength. All mass and concentrations are reported as mg Aq-SNR or mg Aq-SNR/L of dispersion respectively.

2.2.3 Raman Spectroscopy for covalent functionalization of SWCNTs. Samples of pristine SWCNT and of Aq-SNR were deposited onto a  $0.45 \text{ }\mu\text{m}$  pore size polypropylene membrane filter as a thin film. A Kaiser Raman spectrometer was used to measure the integrated area under the D band ( $\text{sp}^3$  character C) relative to the integrated area under the G band ( $\text{sp}^2$  character C). The D:G ratio of the Aq-SNR increased relative to the D:G ratio of the pristine sample which indicates covalent binding between the polyelectrolyte strands and the SWCNT surface.<sup>20</sup> Typical results of a 2 h functionalization are shown in, with the D:G ratio increasing from 0.16 to 0.30.

2.2.4 Total Organic Carbon (TOC) Analysis of aqueous analyte. Concentrations of control and sample solutions were determined by total organic carbon (TOC) using a Shimadzu TOC-LCPN instrument following standard methods.<sup>21</sup> All amber glass collection vials were prepared to remove residual carbon. The vials were pre-cleaned by

rinsing ten times in Milli-Q water then placed in acid bath (10% HCl(aq)) overnight. They were rinsed multiple times in Milli-Q water to remove the acid solution, then covered with aluminum foil, and heated at 400 °C for at least 2 hours in air to remove any residual carbon in the vials. The TOC system was calibrated using standard dilutions of a stock aqueous glucose solution. The response was linear over the range 0.00 mg/L to 10.00 mg/L with an accuracy of  $\pm 0.03$  mg/L. All samples were diluted by a factor of 15 before analysis.

2.2.5 Dynamic Light Scattering (DLS) and Zeta Potential. The effective diameter and zeta potential of poly(vbTMAC) and Aq-SNR dispersion was measured using Malvern DLS Zetasizer instrument.<sup>22</sup> DLS samples of 10  $\mu\text{g/mL}$  of poly(vbTMAC) and 7  $\mu\text{g/mL}$  of Aq-SNR were dispersed in Milli-Q water just before measurement. All zeta potential measurements used 2 mg/L samples. The temperature of the cell was kept at 25 °C and the equilibrium time was 120 s. Multiple runs were averaged after maximum and minimum outliers were discarded.

2.2.6 Scanning Electron Microscopy (SEM). Dispersions of Aq-SNR were diluted and resonicated then drop cast and dried onto a Si chip surface. Drying induced aggregation was kept to a minimum. A LEO 1550 column with field emission gun and 2 nm beam width was used for imaging at 10 kV and a 30  $\mu\text{m}$  aperture. Figure 2.3 compares pristine SWCNTs (3A) to the Aq-SNR material. Some drying induced aggregation is found in all samples. Individual SWCNTs appear as wide as the FE-SEM beam width (2-3 nm). Polymer coated nanotubes aggregated (3B), but even the narrowest tubes show conformal coating of polymer with 8 – 10 nm diameter. Morphology of thin membrane surfaces was also measured (3C) and is discussed below.

2.2.7 Analyte Adsorption Capacity Studies. Multiple analytes were tested to evaluate their broad spectrum removal by the Aq-SNR. Sodium fluorescein (NaFL) was used as a low MW (376.27 g/mol) surrogate for fulvic acids. Tetracycline hydrochloride and carbenicillin disodium were used to evaluate removal of pharmaceutical compounds. PFOA and PFOS were used to test the removal of perfluorinated compounds. Bromoacetic acid and chloroacetic acid were used to evaluate removal of halogenated compounds (e.g., DBP). Bentazon, terbacil, and bromacil were used to evaluate removal of pesticides from water. NaFL sample concentrations were measured using UV-Vis spectroscopy ( $\epsilon_{490} = 0.358 \pm 0.011 \text{ (mg-C/L)}^{-1} \text{ cm}^{-1}$ ). All other analyte concentrations were measured using TOC analysis.

2.2.8 Adsorption Capacity: Fast-Filtration. A known mass of Aq-SNR was deposited on an MCE membrane by filtration. Control studies were performed to determine adsorption of the analyte by the apparatus without any Aq-SNR present. 3.0 ml of each analyte solution, of known initial concentration, were pushed manually through the film using a syringe. Low backpressure allowed the filtration to be completed in less than ten seconds. The concentration of analyte in the filtrate was measured using UV-Vis Spectroscopy or TOC analysis.

2.2.9 Regeneration and Reuse Studies. A known mass of Aq-SNR was deposited onto an MCE support membrane and placed into a glass vial. A NaFL solution of known concentration was added to the vial. The sample was vortexed for 2 h at 500 rpm while small aliquots were taken at intervals to test adsorption kinetics. Figure S2.6 shows the loading  $q$  of NaFL adsorbed onto the outer interface of the membrane as a function of time. To simulate pre-breakthrough conditions we tested the outer interface of the thin

film. The adsorption data are fit to a pseudo-second order diffusive kinetics model with a rate constant  $k = 0.0048 \text{ s}^{-1} (\text{mg/g})^{-1}$ .

For regeneration studies, a known mass of Aq-SNR was deposited onto MCE membrane. The film was placed inside a vial and was allowed to incubate in brine solution (1.5 ml, 2.0 M NaCl(aq)) for 5 min. After removal of the brine, Milli-Q water was used to rinse the remaining brine from the vial and resin (3 replicates, 1.5 mL). A known volume and concentration of NaFL(aq) was then added and allowed to incubate for 5 min. The concentration of the NaFL(aq) solution after incubation was measured by UV-Vis spectroscopy and the process was repeated for 20 cycles.

## 2.3 Results and Discussion

2.3.1 Characterization of Aq-SNR Kinetics of polyelectrolyte growth were measured by  $^1\text{H}$  NMR as described above. We have not yet optimized the performance of the Aq-SNR as a function of polyelectrolyte length. We use a 33% conversion (40 min polymerization) for all polymer synthesis before adding SWCNTs for functionalization. Since we use a 100:1 monomer to initiator ratio these polyelectrolytes should have a molecular mass of about  $33 \times 211.73 \text{ g/mol}$  or 7kD. Using DLS we measured an average hydrodynamic diameter of 1.7 nm three separate syntheses of 25% converted polyelectrolyte. Data shown in Figure S2.7. These data are consistent with radius of gyration data on similar polyelectrolytes. Moreover, since there is only one peak in the DLS analysis of the effective diameters we conclude that there is a minimal amount of bimolecular radical termination during the polymer growth. Any polymer end termination would result in loss of atom economy since those strands could not then react with the SWCNTs. The multi angle light scattering analysis by Takahara et al. show a  $\sim 2$

diameter ( $2 \cdot R_H$ ) for 7kD polyelectrolyte in low salt solution.<sup>23</sup> Their scattering model is consistent with a wormlike cylinder or brush polymer morphology. Zeta potential data (shown in Figure S2.8) measured a +8.8 mV which is consistent with a strong base polyelectrolyte.

Aq-SNR was characterized by UV-Vis-NIR to get the concentration of functionalized SWCNT as a stable dispersion, reported in mg-SWCNT/L. Centrifugation of 200,000 g is required to completely sediment the polyelectrolyte functionalized particles. The total concentration of Aq-SNR includes covalently bound polymer and SWCNT mass, mg/L and the total mass to SWCNT mass ratio was used to get total polymer mass for adoption testing. Energy dispersive x-ray spectroscopy (EDX) on thin films of the Aq-SNR found ~2% Sn by mass (Figure S2.9). Residual tin from the  $\text{Sn(OH)}_2$  equilibrium was removed from the dispersion by sedimentation and then by washing with  $\text{HCl(aq)}$  and then Milli-Q water. There may be some  $\text{SnO}_4(\text{s})$  that we cannot dissolve easily. This residual contaminant will be addressed in subsequent scale-up of our reactor design.

Conformal coating of polymer around the SWCNTs is shown in the FE-SEM image Figure 2.3B. It is important to note that there is no free polymer aggregates or salt on these samples. To use the Aq-SNR for analyte removal we form a thin film on an MCE membrane. These films show very smooth surface topography on top of the MCE membrane (surface morphology due to MCE membrane). Slightly aggregated polymer coated SWCNTs are shown in Figure 2.3C. The thin film exhibits a pin hole free, mesoporous architecture. A survey of the film as measured by SEM is shown in Figure S2.10. Figure S2.11 shows cross-sectional AFM data. The film thickness is ~140nm for

this sample with a total mass of 0.17 mg and mass density of 0.046 mg cm<sup>-2</sup>. The film is not vacuum dried before AFM and the probe tip is interacting very strongly with the surface charges of the polyelectrolytes.

Water samples must pass through a tortuous morphology such that the analyte can easily access the very high surface area Aq-SNR material. The open polymer microstructure and thin film morphology enables this “contact resin” behavior. This method of analyte removal was chosen over incubation so as to simulate ultrafiltration (UF) water purification technology. Intrinsic membrane resistance of these films was calculated by measuring the flux of water at a constant transmembrane pressure of 1.0x10<sup>5</sup> Pa, according to Darcy’s law.<sup>24-25</sup> The measured membrane resistance  $\kappa_m = 2.1 \times 10^{11} \text{ m}^{-1}$  is smaller than typical UF membranes with a  $\kappa_m = 2 \times 10^{12} \text{ m}^{-1}$ . A modest loading value  $q_e = 20 \text{ mg/g}$  with a 1 m<sup>2</sup> membrane at 0.9 mg/cm<sup>2</sup> mass density, would effectively remove 95% PFAS from 10<sup>5</sup> L of 1 mg-C/L effluent.

We monitor covalent functionalization of the polymer to the SWCNTs by measuring the D:G ratio from Raman spectroscopy. The larger the D:G ratio, the more defects we introduce into the SWCNT’s wall. The living radical end of the polymer reacts easily with  $\pi$  conjugated electron density on the SWCNTs and other nanostructured carbons.<sup>26</sup> We have not fully optimized the functionalization process. However, the Raman spectroscopy suggests that the attachment of polyelectrolytes to the SWCNTs is quite fast. Baseline-normalized Raman spectra in the D and G band region are overlaid in Figure 2.2 and in Figure S2.12. The area under each band is calculated and the D:G ratio for pristine versus functionalized Aq-SNR is compared. The D:G ration for the 2 h, 12 h, and 3 day functionalization are similar, 0.30, 0.33, and 0.33 respectively. While the

D:G ratio does indicate covalent attachment of polyelectrolyte strands to the SWCNT it does not give a quantitative measure of the degree of functionalization of the Aq-SNR. We use the supernatant of the centrifuged samples to partially purify the samples. It is clear that the Aq-SNR is not uniformly coated with polymer. During purification of the material some of the nanostructured carbon material sediments at low <10,000 g. The D:G ratio of the sediment material after a 20,000 g treatment is 0.26. Additionally, we have analyzed the Raman D:G ratio of Aq-SNR from the supernatant of a 200,000 g centrifugation. The material that stays in the supernatant at that high a RCF, is stabilized with polyelectrolyte attachment. The spectra in Figure S2.13 shows a D:G ratio of 0.93 from material collected from the supernatant only. So this ratio is a measure of how stable the functionalized tubes are during centrifugation. Moreover, supernatant from samples after centrifugation at 20,000 g have a higher zeta potential, 38.4 mV versus the zeta from the sample before any centrifugation, 22.8 mV as shown in Figure S2.14 for the 2 h functionalized Aq-SNR. Changes to our reactor design should allow us to optimize functionalization density.

DLS of 2 h , 12 h and 3 day Aq-SNR samples are shown in Figure S2.15.

Calculated hydrodynamic effective diameters for 2 h, 12 h, and 3 day are  $213 \pm 5$  nm,  $205 \pm 5$  nm, and  $213 \pm 7$  nm respectively. The effective diameter is calculated from the measured diffusion coefficient and assumes a spherical model. These particles are more rod like. From SEM we estimate the particle width to be  $w = 10$  nm. Then for a flexible rod length  $L = 1000$  nm, the calculated hydrodynamic diameter is  $D_h = L / (\ln(L/w) + 0.32) = 203$  nm, which is consistent with our measured values.<sup>27</sup> Fully characterized materials are then deposited as thin films and used to remove analyte from

water samples. The ratio of the total mass of Aq-SNR (measured by filtering out the purified material) to the SWCNT mass only (measured by the NIR absorption at 1025 nm) increases as functionalization time increases. These data are listed in Figure S2.12. The 12 h sample has a higher amount of polymer attachment per SWCNT mass than the 2 h (3.73 ratio to 2.40 ratio respectively). For this fundamental study we only add a small amount, ~30 mg of SWCNTs to the polymer solution during the attachment reaction. The SWCNTs are added to the ARGET ATRP reaction at the same time (after ~33% conversion). As the reaction proceeds, the radical end of the 33-mer attacks the  $sp^2$  carbon on the SWCNT walls. But, many of the polyelectrolyte chains continue to react with the other ~60% of the vbTMAC monomer resulting in longer chains, with more mass, which then subsequently attach to the SWCNTs. After removal of unbound polyelectrolyte, the mass of polymer attached to the SWCNTs is 2.4 – 4.8 times greater than the mass of the SWCNTs.

2.3.2 Adsorption Capacity Testing. To compare different adsorbent materials with various adsorbate compounds we measure the equilibrium loading capacity  $q_e$  in mg analyte / g adsorbent. In our previous works we published and analyzed the adsorption isotherm analysis and reported that these thin film nanoresin materials behave like “contact” resins which reach a pseudo-equilibrium in only a few seconds of exposure. We have shown that we can reproducibly synthesize the Aq-SNR, We measured the adsorption capacity of each batch of Aq-SNR against sodium fluorescein NaFL, which we use as a surrogate for natural water DBP precursors. A known volume and concentration of analyte is passed through a known mass of Aq-SNR as a thin film membrane. All fast-filtration experiments take less than 10 seconds. From control

studies of water or brine passed through the Aq-SNR / MCE filters, we found no evidence of SWCNTs or carbon/polymer coming out of the membrane filter. Results for  $q_e$  of NaFL on 2 h and 12 h Aq-SNR are shown in Figure 2.4. We compare  $q_e$  using an initial concentration  $C_o = 5.8$  mg-C NaFL / L. The SWCNT mass only, was used so that we can directly compare the material based on number of nanotubes in the film. We show the comparison of an addition four syntheses of 2 h and 12 h Aq-SNR binding capacity in Figure S2.16. All ten nanoresin samples showed a  $q_e$  of  $\sim 100$  mg-C NaFL / g SWCNT, a 10% loading capacity in  $< 10$  seconds of contact time.

2.3.3 Percentage removal of Analyte. The USEPA is evaluating systems for PFAs contamination reduction by challenging them with an influent of  $1.5 \pm 30\%$   $\mu\text{g/L}$  (total of both PFOA and PFOS)<sup>4</sup> and must reduce this contamination by more than 95% to  $0.07$   $\mu\text{g/L}$  or less. This Aq-SNR also removes other classes of analyte from water. In Figure 2.5, we show percent removal data for PFOS, PFOA and the antibiotic carbenicillin disodium, and the pesticide bentazon. Membrane mass was increased until at least 95% of the analyte was removed in one fast-filtration pass through the Aq-SNR film. The mass density for 95% removal of carbenicillin disodium, and bentazon was  $0.13$   $\text{mg/cm}^2$ . The required mass density for the PFAS compounds was  $0.90$   $\text{mg/cm}^2$ . The higher mass required for the PFAS is consistent with the challenge of removing these hydrophilic and persistent contaminants from water. The initial concentration of all analytes ranged between  $2-4$   $\text{mg-C/L}$ . The concentration was measured using TOC analysis ( $\text{mg-C/L}$ ). The limit of detection of our TOC analyzer and method is only  $\sim 0.2$   $\text{mg-C/L}$ . Further studies, at the lower EPA detection limits, will require tandem mass spectrometry.<sup>28-29</sup>

Relative equilibrium adsorption capacity of the Aq-SNR against several other compounds are listed in Table S2.1. In addition to the surrogate compound there are four classes of compounds that these materials can remove from water effectively. The equilibrium loading  $q_e$  in mg-C analyte / g Aq-SNR are from fast-filtration experiment where the sample was pressed through the membrane in just a few seconds. In its current form, all of the Aq-SNR are anion exchange resins so they are most effective at removing compounds with some negative charge character. With the exception of the tetracycline HCl, all of these compounds have negative zeta potentials at natural water pH 6.5 – 7.5. The absolute value of the  $q_e$  is not the subject of this study. Percent removal is the most important quality and we have shown near complete removal of most of these contaminants from water test samples. Future work will test our cation exchange resins and our materials in which we optimize for a specific analyte, like short chain PFAS.

2.4 Conclusions. We have demonstrated an all-aqueous synthesis and purification of functionalized SWCNTs with short chain polyelectrolyte resins using a modified facile ARGET ATRP mechanism. The synthesis and purification procedure did not involve any organic or hazardous reagents and control studies found no traces of SWCNTs or unbound polymer released from the materials during water treatment. Polyelectrolyte resin chains enable fast equilibration with analyte compounds in the influent solution, while the SWCNTs form a mesoporous scaffolding and provide a tortuous, but low resistance, path for the analyte to flow through. The covalent attachment of resins to SWCNTs is also confirmed with Raman spectroscopy and zeta potential measurements of highly stabilized dispersions. The DLS, zeta potential and the adsorption capacity of various Aq-SNRs synthetic batches show consistency in hydrodynamic diameters, high

surface charge, and adsorption performance. We have shown that these materials successfully target and electrostatically bind to several classes of pervasive compounds. We showed the effectiveness of these thin films by testing them against several compounds and reducing the analyte concentration by 95% – 100%. We have demonstrated a sustainable material that can be regenerated and reused many times. We have shown that the nanostructured carbon materials do not leach or escape from the membrane and therefore are safe to the environment<sup>30-31</sup> and drinking water applications (Green Principle 12).<sup>19</sup> Implementing these materials into existing membrane filtration systems should increase removal capabilities and lower operating costs of water treatment facilities. This fundamental proof-of-principle study will be extended to other nanostructured carbon materials that are much less expensive than SWCNTs, thereby lowering the cost of scaling this methodology.

**Safety.** Personal protective equipment should be used when doing any of the experiments described in this paper. Special care should be taken when working with evacuated glassware and Schenk line apparatus. All chemical waste should be disposed of as hazardous waste in accordance with regulatory agency oversight.

**Acknowledgements.** This material is based upon work supported by the National Science Foundation under Grant No. 1724972. This work was supported, in part, by funds provided by the Charlotte Research Institute at the University of North Carolina at Charlotte, the Nanoscale Science program, and support from the Thomas D. Walsh Graduate Research Fellowship to BRJ.

## 2.5 References.

- (1) Rayne, S.; Forest, K. Perfluoroalkyl sulfonic and carboxylic acids: A critical review of physicochemical properties, levels and patterns in waters and wastewaters, and treatment methods. *Journal of Environmental Science and Health Part a-Toxic/Hazardous Substances & Environmental Engineering* **2009**, *44* (12), 1145-1199, DOI: 10.1080/10934520903139811.
- (2) Hsu, J. Y.; Hsu, J. F.; Ho, H. H.; Chiang, C. F.; Liao, P. C. Background levels of Persistent Organic Pollutants in humans from Taiwan: Perfluorooctane sulfonate and perfluorooctanoic acid. *Chemosphere* **2013**, *93* (3), 532-537, DOI: 10.1016/j.chemosphere.2013.06.047.
- (3) Soriano, A.; Gorri, D.; Urtiaga, A. Efficient treatment of perfluorohexanoic acid by nanofiltration followed by electrochemical degradation of the NF concentrate. *Water Research* **2017**, *112*, 147-156, DOI: 10.1016/j.watres.2017.01.043.
- (4) Karanfil, T.; Krasner, S. W.; Westerhoff, P.; Xie, Y. F. Recent Advances in Disinfection By-Product Formation, Occurrence, Control, Health Effects, and Regulations. In *Disinfection by-Products in Drinking Water: Occurrence, Formation, Health Effects, and Control*; Karanfil, T.; Krasner, S. W.; Xie, Y., Eds.; 2008; pp 2-19.
- (5) Bond, T.; Goslan, E. H.; Parsons, S. A.; Jefferson, B. Disinfection by-Product Formation of Natural Organic Matter Surrogates and Treatment by Coagulation, MIEX® and Nanofiltration. *Water Res.* **2010**, *44* (5), 1645-1653.
- (6) Bolto, B.; Dixon, D.; Eldridge, R.; King, S.; Linge, K. Removal of natural organic matter by ion exchange. *Water Research* **2002**, *36* (20), 5057-5065, DOI: 10.1016/s0043-1354(02)00231-2.
- (7) Wang, H. T.; Keller, A. A.; Clark, K. K. Natural Organic Matter Removal by Adsorption onto Magnetic Permanently Confined Micelle Arrays. *J. Hazard. Matter* **2011**, *194*, 156-161.
- (8) Hruska, J.; Kram, P.; McDowell, W. H.; Oulehle, F. Increased Dissolved Organic Carbon (DOC) in Central European Streams Is Driven by Reductions in Ionic Strength Rather Than Climate Change or Decreasing Acidity. *Environ. Sci. Technol* **2009**, *43* (12), 4320-4326.

- (9) Geise, G. M.; Lee, H. S.; Miller, D. J.; Freeman, B. D.; McGrath, J. E.; Paul, D. R. Water Purification by Membranes: The Role of Polymer Science. *J. Polym. Sci. Pt. B-Polym. Phys.* **2010**, *48* (15), 1685-1718, DOI: 10.1002/polb.22037.
- (10) Ambashta, R. D.; Sillanpaa, M. Water purification using magnetic assistance: A review. *Journal of Hazardous Materials* **2010**, *180* (1-3), 38-49, DOI: 10.1016/j.jhazmat.2010.04.105.
- (11) Zaggia, A.; Conte, L.; Falletti, L.; Fant, M.; Chiorboli, A. Use of strong anion exchange resins for the removal of perfluoroalkylated substances from contaminated drinking water in batch and continuous pilot plants. *Water Research* **2016**, *91*, 137-146, DOI: 10.1016/j.watres.2015.12.039.
- (12) Johnson, B. R.; Eldred, T. B.; Nguyen, A. T.; Payne, W. M.; Schmidt, E. E.; Alansari, A. Y.; Amburgey, J. E.; Poler, J. C. High-Capacity and Rapid Removal of Refractory NOM Using Nanoscale Anion Exchange Resin. *ACS Applied Materials & Interfaces* **2016**, *8* (28), 18540-18549, DOI: 10.1021/acsami.6b04368.
- (13) Fantin, M.; Isse, A. A.; Matyjaszewski, K.; Gennaro, A. ATRP in Water: Kinetic Analysis of Active and Super-Active Catalysts for Enhanced Polymerization Control. *Macromolecules* **2017**, *50* (7), 2696-2705, DOI: 10.1021/acs.macromol.7b00246.
- (14) Fantin, M.; Isse, A. A.; Gennaro, A.; Matyjaszewski, K. Understanding the Fundamentals of Aqueous ATRP and Defining Conditions for Better Control. *Macromolecules* **2015**, *48* (19), 6862-6875, DOI: 10.1021/acs.macromol.5b01454.
- (15) Jakubowski, W.; Min, K.; Matyjaszewski, K. Activators regenerated by electron transfer for atom transfer radical polymerization of styrene. *Macromolecules* **2006**, *39* (1), 39-45, DOI: 10.1021/ma0522716.
- (16) Simakova, A.; Averick, S. E.; Konkolewicz, D.; Matyjaszewski, K. Aqueous ARGET ATRP. *Macromolecules* **2012**, *45* (16), 6371-6379, DOI: 10.1021/ma301303b.
- (17) Pettine, M.; Millero, F. J.; Macchi, G. HYDROLYSIS OF TIN(II) IN AQUEOUS-SOLUTIONS. *Anal. Chem.* **1981**, *53* (7), 1039-1043, DOI: 10.1021/ac00230a027.

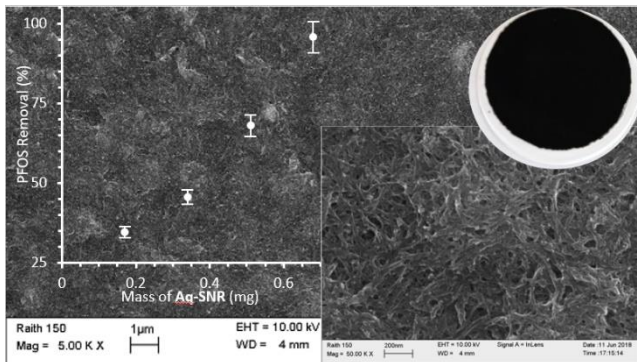
- (18) Cigala, R. M.; Crea, F.; De Stefano, C.; Lando, G.; Milea, D.; Sammartano, S. The inorganic speciation of tin(II) in aqueous solution. *Geochim. Cosmochim. Acta* **2012**, *87*, 1-20, DOI: 10.1016/j.gca.2012.03.029.
- (19) Dahl, J. A.; Maddux, B. L. S.; Hutchison, J. E. Toward Greener Nanosynthesis. *Chem. Rev.* **2007**, *107* (6), 2228-2269, DOI: 10.1021/cr050943k.
- (20) Bachilo, S. M.; Strano, M. S.; Kittrell, C.; Hauge, R. H.; Smalley, R. E.; Weisman, R. B. Structure-assigned optical spectra of single-walled carbon nanotubes. *Science* **2002**, *298* (5602), 2361-2366.
- (21) Ozcan, A.; Ozcan, A. A.; Demirci, Y. Evaluation of mineralization kinetics and pathway of norfloxacin removal from water by electro-Fenton treatment. *Chem. Eng. J.* **2016**, *304*, 518-526, DOI: 10.1016/j.cej.2016.06.105.
- (22) Haladjova, E.; Mountrichas, G.; Pispas, S.; Rangelov, S. Poly(vinyl benzyl trimethylammonium chloride) Homo and Block Copolymers Complexation with DNA. *J. Phys. Chem. B* **2016**, *120* (9), 2586-2595, DOI: 10.1021/acs.jpcc.5b12477.
- (23) Ishikawa, T.; Kikuchi, M.; Kobayashi, M.; Ohta, N.; Takahara, A. Chain Conformation of Poly 2-(methacryloyloxy)ethyltrimethylammonium chloride in Aqueous Sodium Chloride Solutions. *Macromolecules* **2013**, *46* (10), 4081-4088, DOI: 10.1021/ma4001868.
- (24) Alston, J. R.; Banks, D. J.; McNeill, C. X.; Mitchell, J. B.; Popov, L. D.; Shcherbakov, I. N.; Poler, J. C. Adsorption studies of divalent, dinuclear coordination complexes as molecular spacers on SWCNTs. *PCCP Phys. Chem. Chem. Phys.* **2015**, *17*, 29566 - 29573, DOI: 10.1039/c5cp05419b.
- (25) Darcy, H. Appendix - Note D, "Determination of the laws of flow of water through sand". In *Les Fontaines Publiques de la Ville de Dijon*; DALMONT, V., Ed.; Bookseller of the Imperial Corps of Bridges, Roads and Mines: Paris, France, 1856.
- (26) Silva, H. S.; Ramanitra, H. H.; Bregadiolli, B. A.; Begue, D.; Graeff, C. F. O.; Dagrón-Lartigau, C.; Peisert, H.; Chasse, T.; Hiorns, R. C. Oligo- and Poly(fullerene)s for Photovoltaic Applications: Modeled Electronic Behaviors and Synthesis. *J. Polym. Sci. Pol. Chem.* **2017**, *55* (8), 1345-1355, DOI: 10.1002/pola.28502.

- (27) Nair, N.; Kim, W.-J.; Braatz, R. D.; Strano, M. S. Dynamics of Surfactant-Suspended Single-Walled Carbon Nanotubes in a Centrifugal Field. *Langmuir* **2008**, *24* (5), 1790-1795, DOI: 10.1021/la702516u.
- (28) Cahill, J. D.; Furlong, E. T.; Burkhardt, M. R.; Kolpin, D.; Anderson, L. G. Determination of pharmaceutical compounds in surface- and ground-water samples by solid-phase extraction and high-performance liquid chromatography–electrospray ionization mass spectrometry. *J. Chromatogr. A* **2004**, *1041* (1), 171-180, DOI: <https://doi.org/10.1016/j.chroma.2004.04.005>.
- (29) Winslow, S. D.; Pepich, B. V.; Martin, J. J.; Hallberg, G. R.; Munch, D. J.; Frebis, C. P.; Hedrick, E. J.; Krop, R. A. Statistical Procedures for Determination and Verification of Minimum Reporting Levels for Drinking Water Methods. *Environ. Sci. Technol.* **2006**, *40* (1), 281-288, DOI: 10.1021/es051069f.
- (30) Sapsford, K. E.; Algar, W. R.; Berti, L.; Gemmill, K. B.; Casey, B. J.; Oh, E.; Stewart, M. H.; Medintz, I. L. Functionalizing Nanoparticles with Biological Molecules: Developing Chemistries that Facilitate Nanotechnology. *Chem. Rev.* **2013**, *113* (3), 1904-2074, DOI: 10.1021/cr300143v.
- (31) Albrecht, M. A.; Evans, C. W.; Raston, C. L. Green chemistry and the health implications of nanoparticles. *Green Chemistry* **2006**, *8* (5), 417-432, DOI: 10.1039/B517131H.

## 2.6 Figures and Tables

### TOC/Abstract Graphic

A new water purification ion exchange membrane has been synthesized using an all-aqueous and sustainable process. These thin film membranes exhibit a pin hole free, mesoporous architecture that rapidly removes several classes of pervasive and persistent contaminants from water.



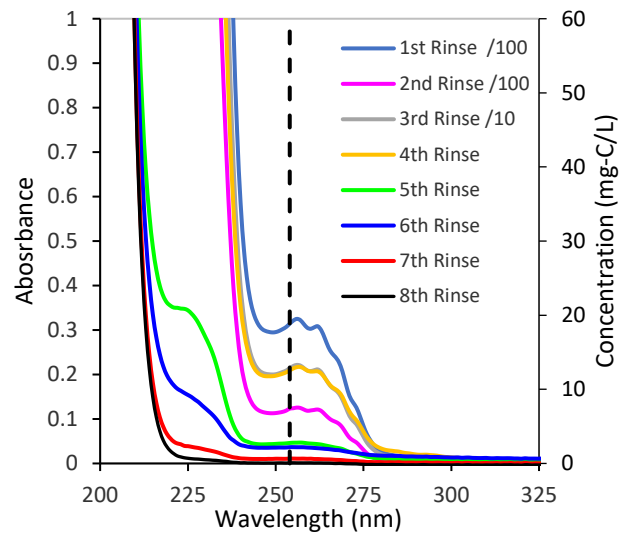


Figure 2.1. Removal of vbTMAC monomer and unbound polymer after successive centrifugation and dispersal into brine cycles. UV-Vis determination of concentration

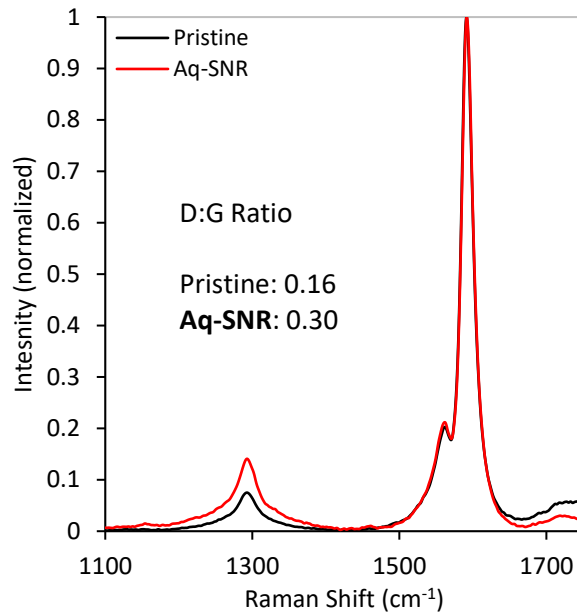


Figure 2.2. Normalized Raman spectra of a 2 h Pristine SWCNT and Aq-SNR after centrifugation at 20,000 RCF for 1 hr. Increase in the ratio of the area under the D and G bands (the D:G ratio) indicates covalent functionalization of ionomer strands to SWCNT wall.

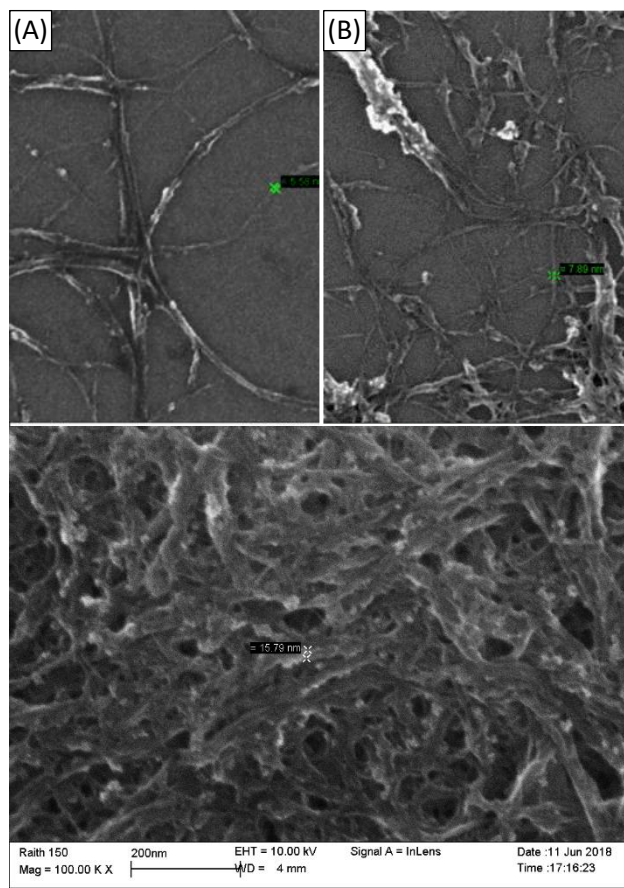


Figure 2.3. FE-SEM images of pristine SWCNTs (A) and Aq-SNR (B) drop cast from a dilute dispersion onto a Si chip. Scale bar 200 nm and column conditions identical for all images. Survey of Aq-SNR shows no residual free polymer or salts. In 4(C) we show typical film of Aq-SNR deposited on an MCE membrane.

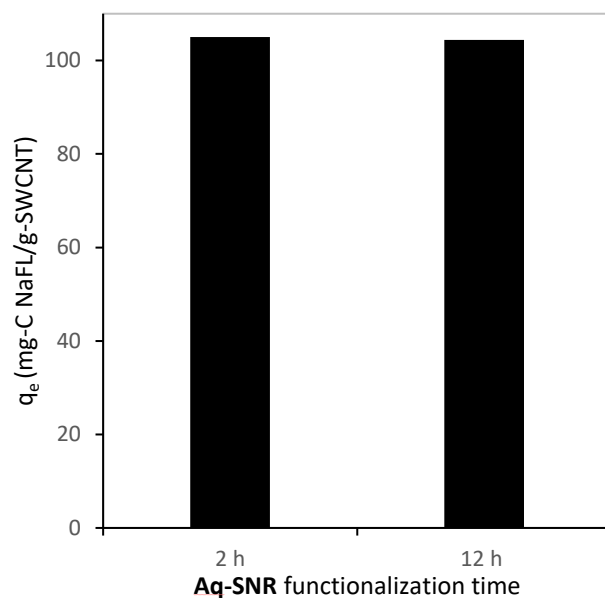


Figure 2.4. Equilibrium loading capacity of NaFL onto Aq-SNR using an initial concentration  $C_0 = 5.8$  mg-C/L. The mass of the adsorbent is the SWCNT mass only so we can directly compare the material based on number of nanotubes in the film.

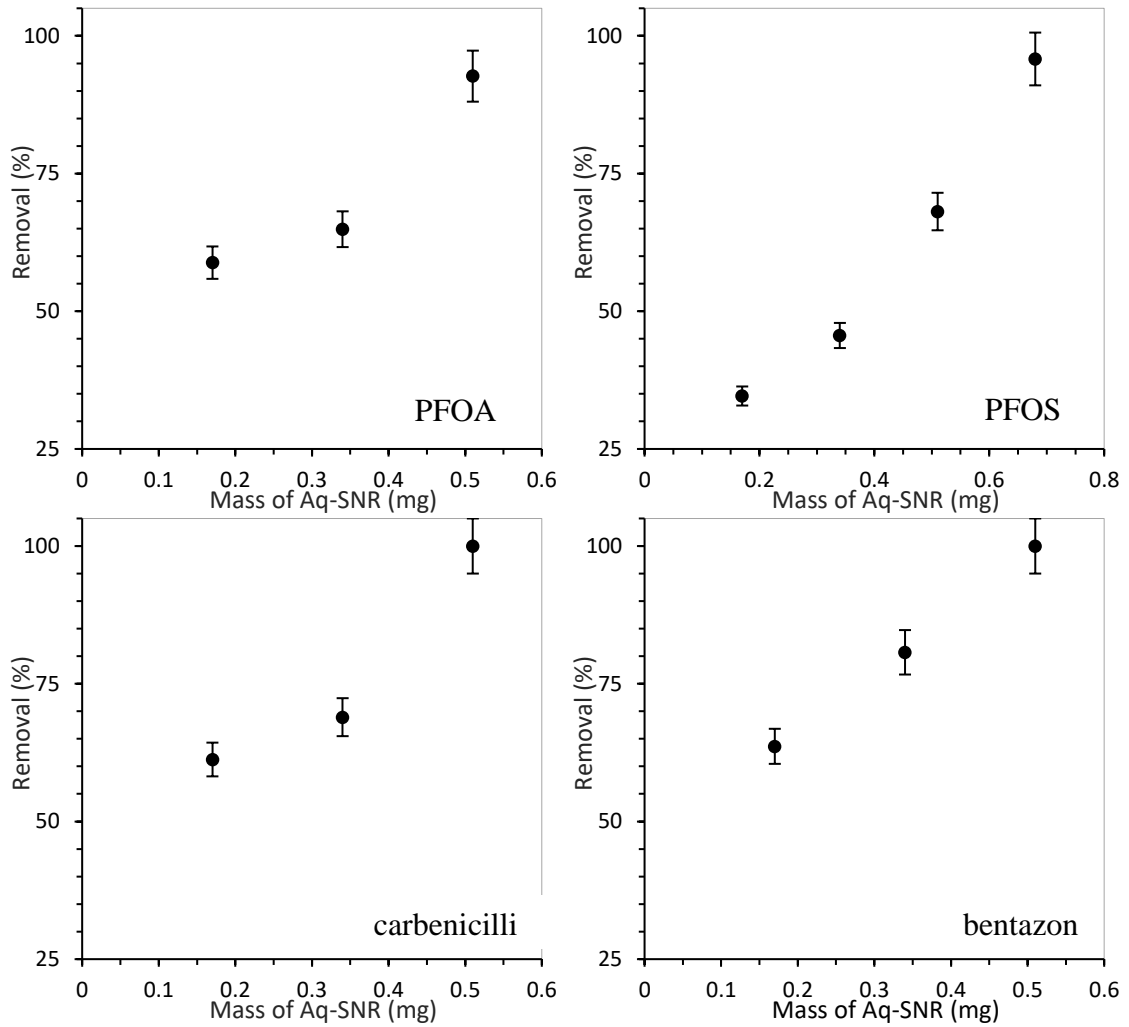


Figure 2.5. Percent removal of analyte versus Aq-SNR membrane mass. Membrane area for PFOA and PFOS is  $0.58 \text{ cm}^2$  and is  $3.78 \text{ cm}^2$  for carbenicillin and bentazon removal.

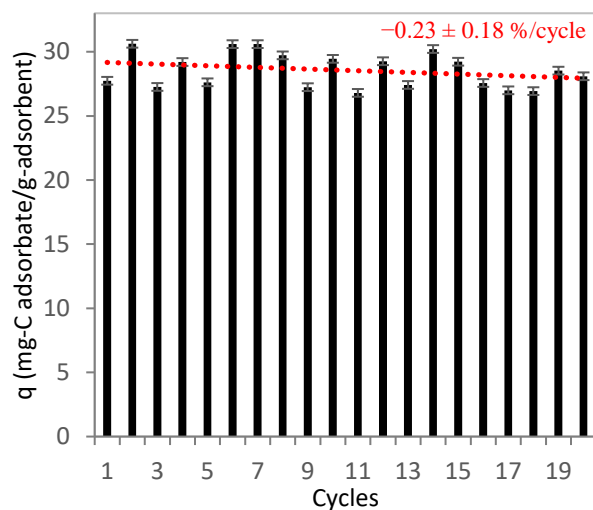


Figure 2.6. Regeneration and reusability study. Surrogate NaFL used to test adsorption by incubating against a thin film of Aq-SNR. 5 min brine incubation followed by water rinse before next exposure to surrogate adsorbate. Process repeated for 20 cycles. Experiment repeated in triplicate. 0.23% decrease in q per cycle is close to the 95% confidence interval error in the slope.

## 2.7 Supplementary figures and tables



Figure S2.1: After centrifugation at 100,000 RCF (1 h), the reaction mixture deposits at the wall of the polycarbonate tubes

## Removal of brine from NanoResin



Figure S2.2: Brine removal from Aq-SNR dispersion. (A) Aq-SNR is added in the form of dialyte and MilliQ is added as dialysate. The dialysate was replaced after every 2 h and then conductivity of dialysate was checked as a function of the number of iterations. This confirms maximal removal of brine ( $<1 \mu\text{S}/\text{cm}$ ).

ARGET-ATRP polymerization scheme:

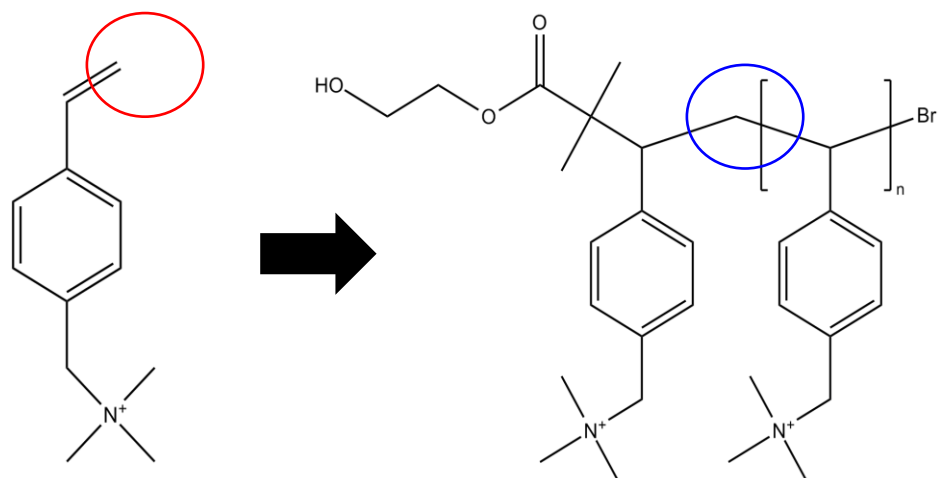


Figure S2.3: Reaction scheme showing the change from vinylic to allylic conditions for the terminal hydrogen.

Percent Conversion of Monomer:

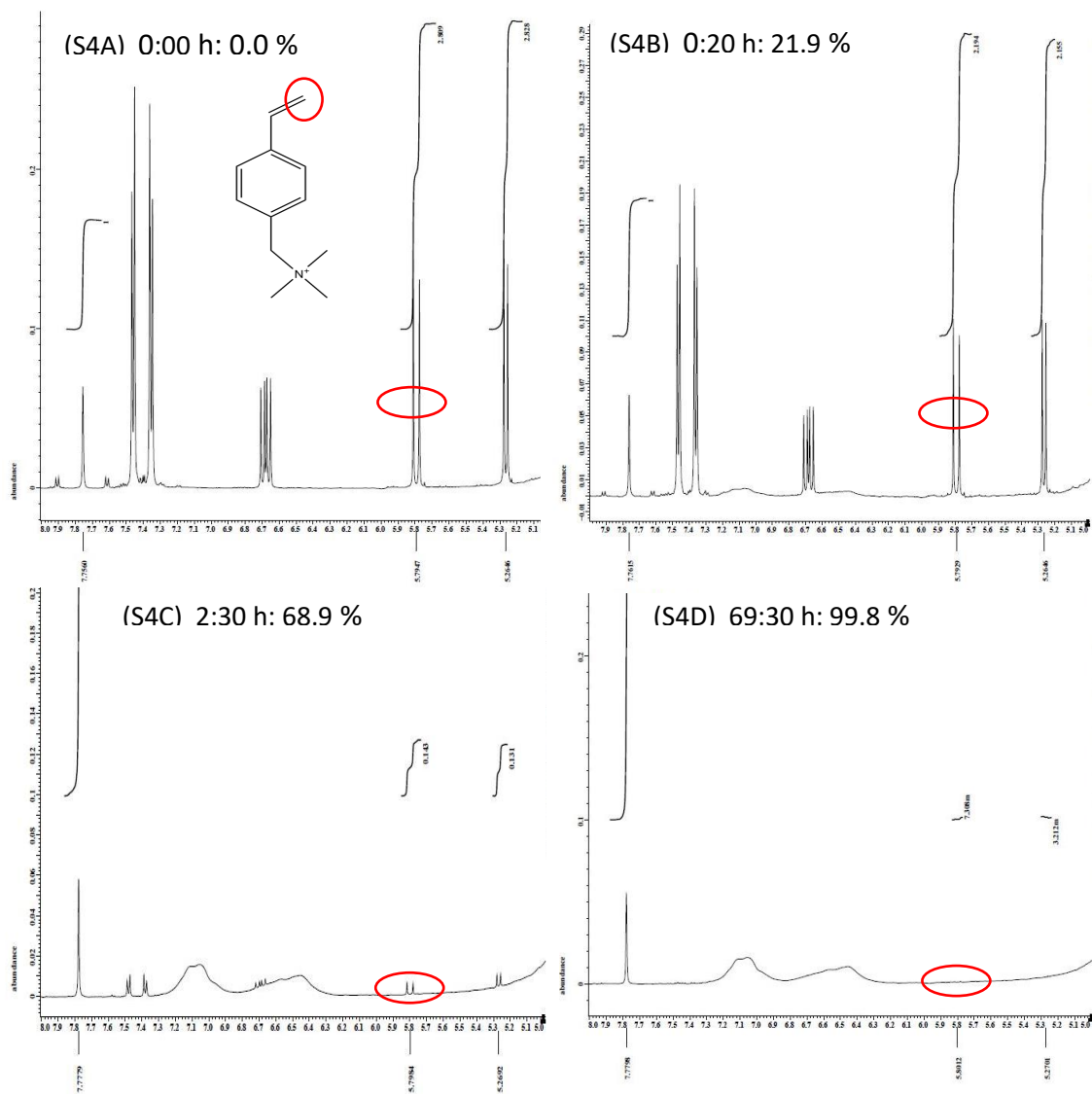


Figure S2.4: <sup>1</sup>H NMR spectra of reaction mixtures from polymerization reaction versus time. To monitor the conversion of vbTMAC monomer to polymer, the vinylic proton (5.8 ppm, 1H, d) decreases in relation to the DMF internal standard signal (7.8 ppm, 1H, s). The ratio between initial peak integration and the integration at time t is used to determine the percent conversion.

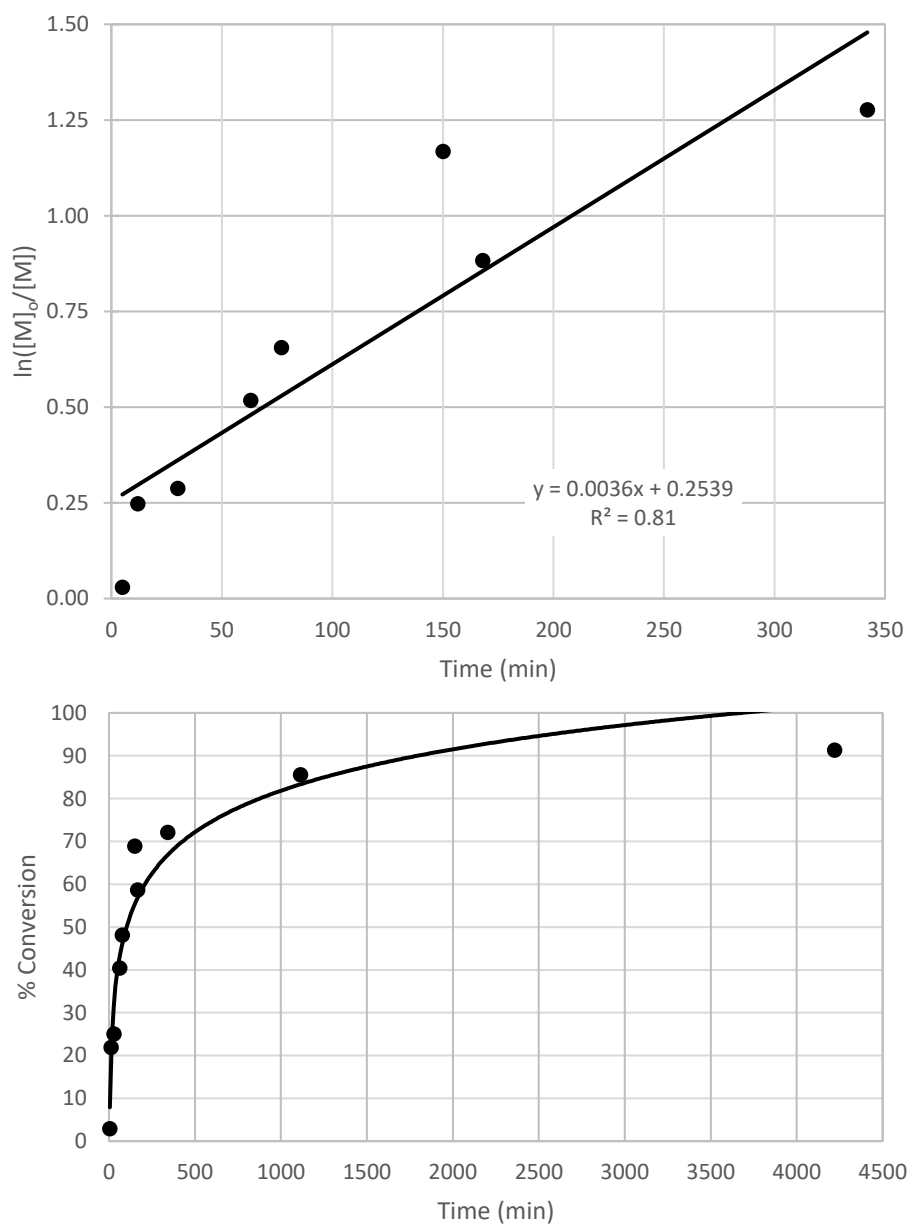


Figure S2.5: Percent conversion (lower) and  $\ln ([M]_0/[M])$  (upper) versus time. 40 min polymer growth results in 33% conversion of monomer.

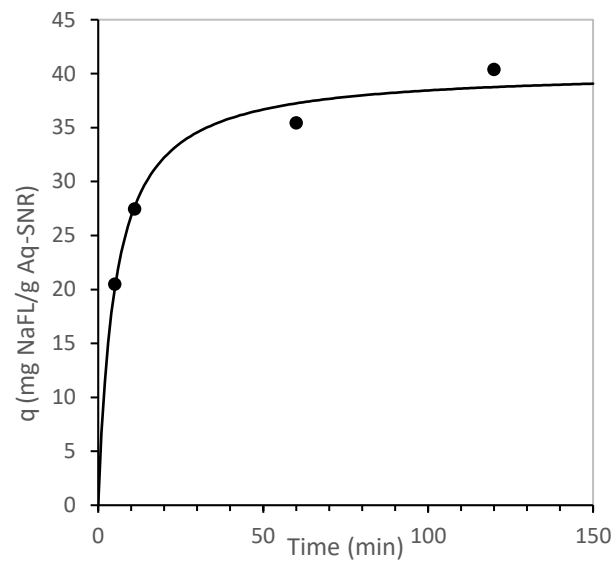
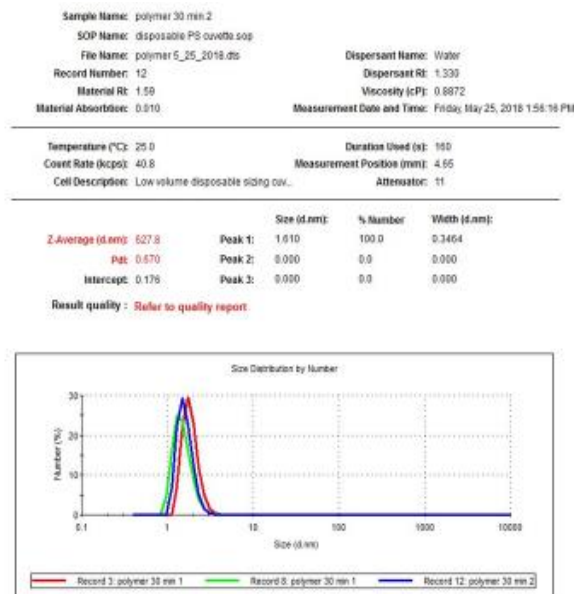


Figure S2.6: Adsorption kinetics of surrogate NOM NaFL into a thin Aq-SNR membrane. Pseudo-second order diffusive kinetics model fit to the data with a rate constant  $k = 0.0048 \text{ s}^{-1}$



**Figure :** Number distribution of polymer grown for 30 minutes (sample is centrifuged, dialyzed and pushed through Anapof filter 0.020  $\mu\text{m}$  pore size)

Sample name	Hydrodynamic diameter ( $\mu\text{m}$ )
Polymer 30 min 1 <sup>st</sup>	1.860
Polymer 30 min 2 <sup>nd</sup>	1.509
Polymer 30 min 3 <sup>rd</sup>	1.610

Figure S2.7: DLS characterization of ionomer after 30 min of growth or 25% conversion. Hydrodynamic effective diameter analyzed from three runs. Three syntheses with the same work up were measured. All data shown.

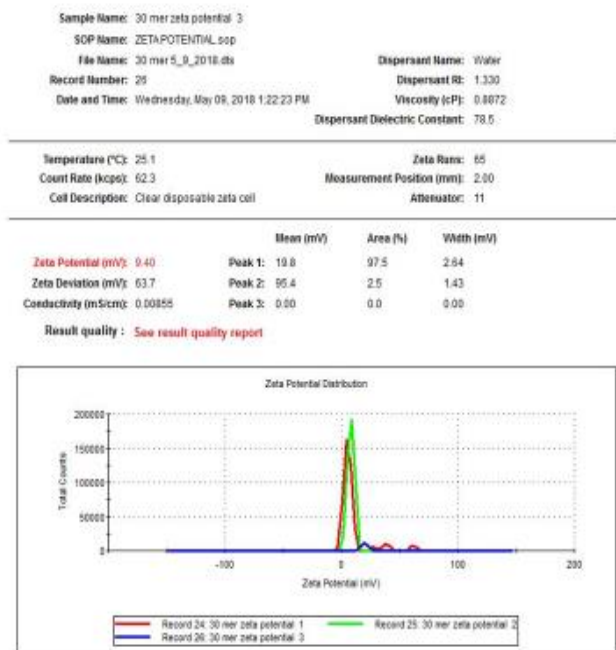


**Figure :** Zeta potential of polymer grown for 30 minutes (sample is centrifuged and dialyzed)

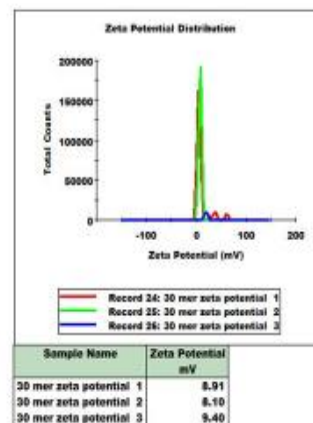


Figure S2.8: Zeta potential characterization of ionomer after 30 min of growth or 25% conversion. Average zeta potential is 8.8 mV. All data shown.

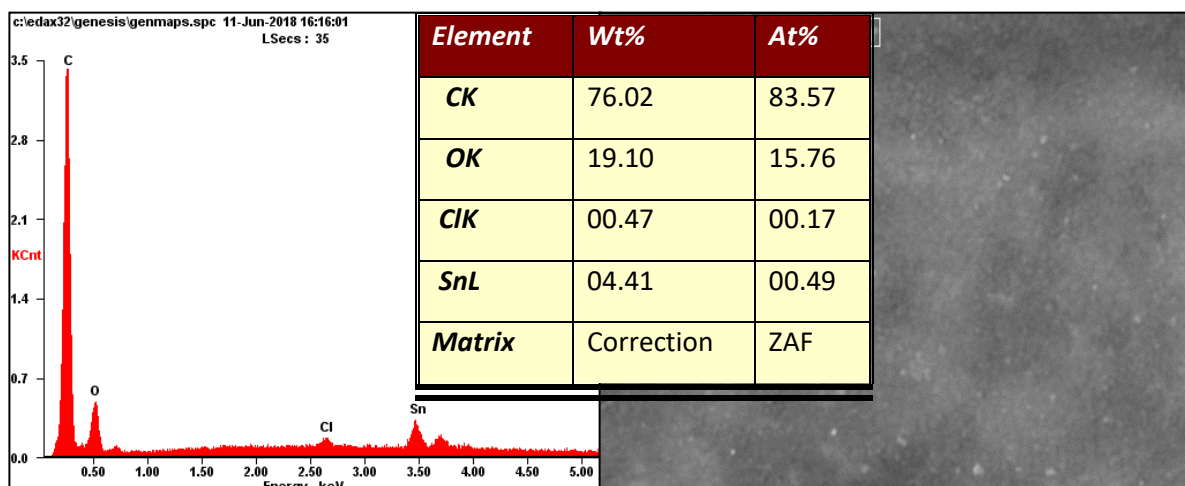
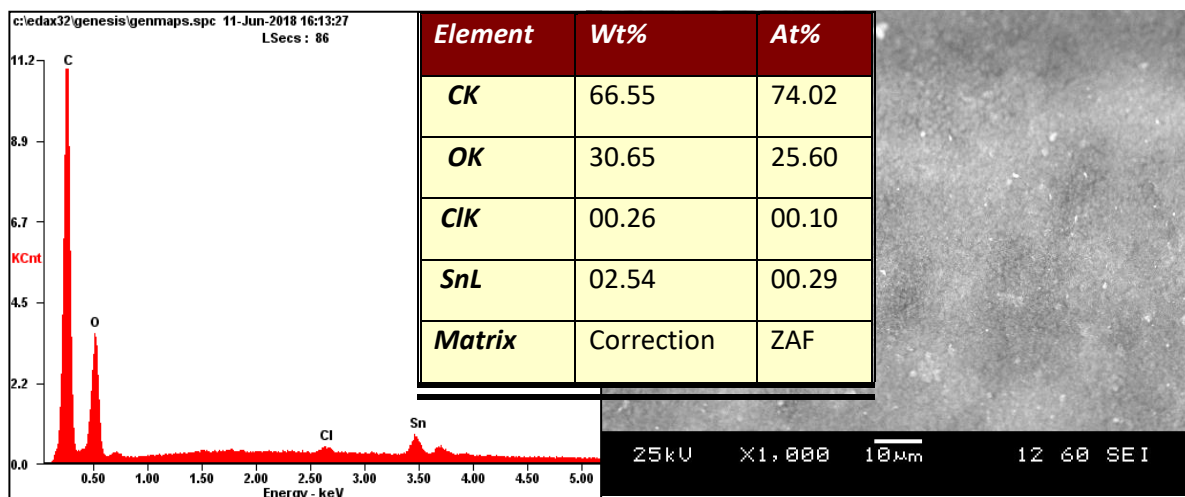


Figure S2.9: EDX of 2 h Aq-SNR thin film on MCE membrane. Small particles of tin compound still present after acid treatment. Could be tin(IV) oxide. Both images acquired at 25kV with the same 10  $\mu\text{m}$  scale bar as shown in upper image. Lower data is of the small area in the box surrounding a particle. Sn concentration is twice as high on that spot indicating the persistence of insoluble tin(IV) oxide.

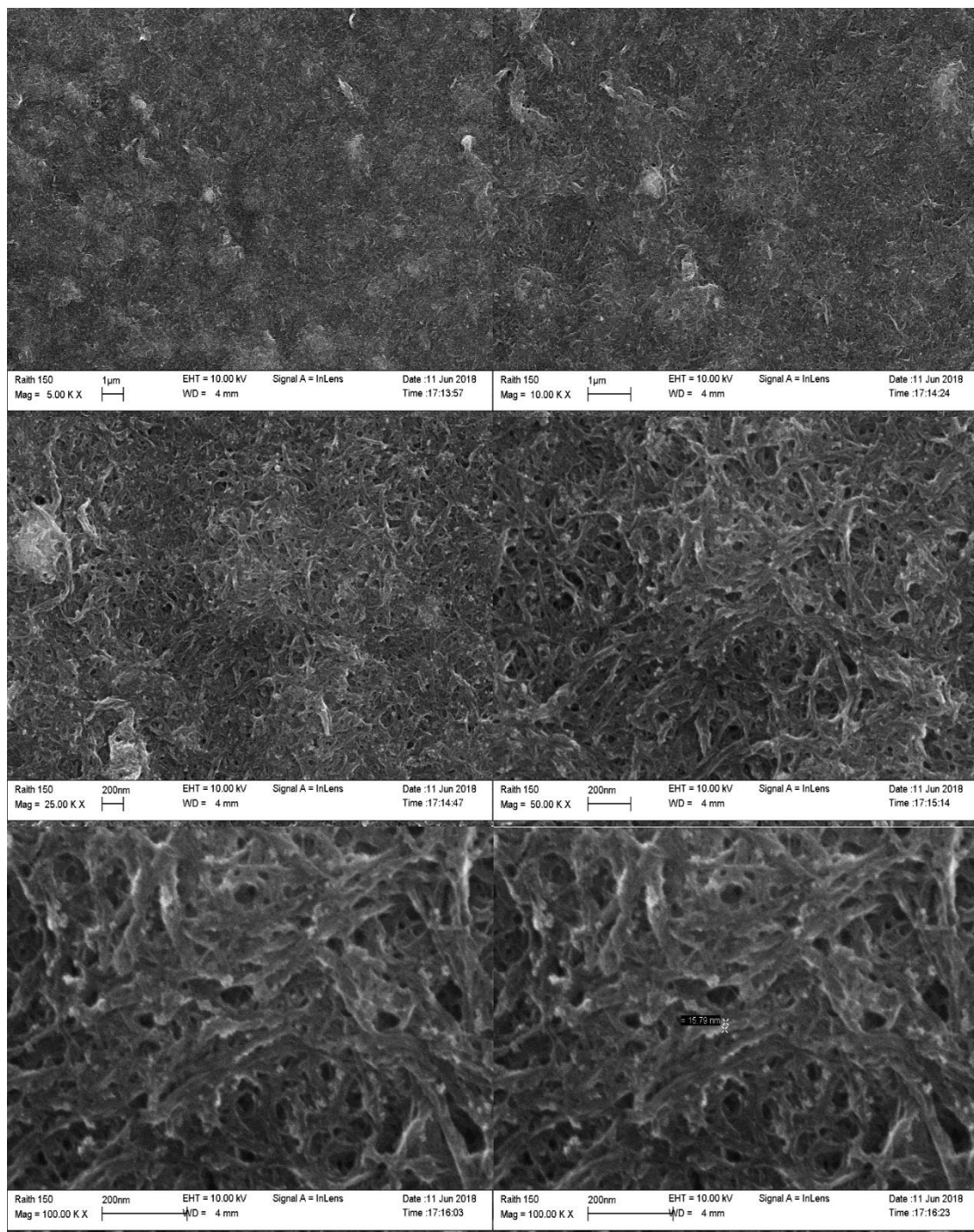


Figure S2.10: FE-SEM micrographs of Aq-SNR thin film on top of an MCE membrane. Pin hole free, smooth films were made with areas up to 16 cm<sup>2</sup>. Scale up to large area membranes is beyond the scope of this proof of principle study.

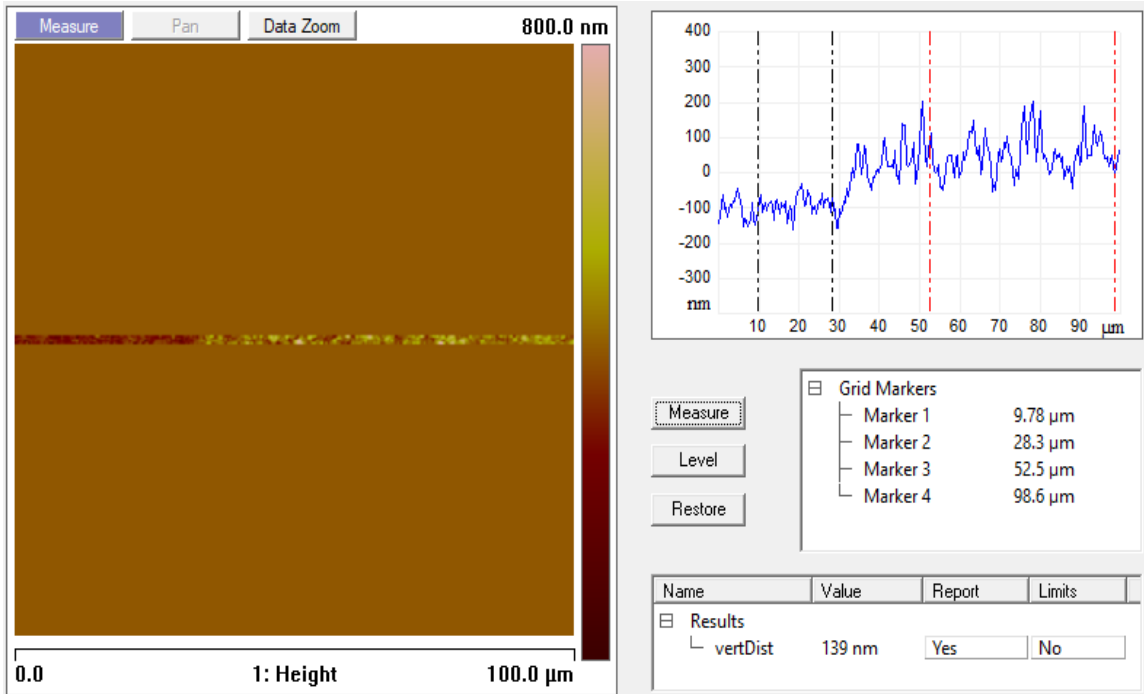


Figure S2.11: AFM micrographs of Aq-SNR thin film on top of an MCE membrane. Cross sectional analysis shows about 140 nm thick film. The AFM tip seems to be interacting strongly with the ionomer film. These films are not completely dry.

# Covalent attachment analysis

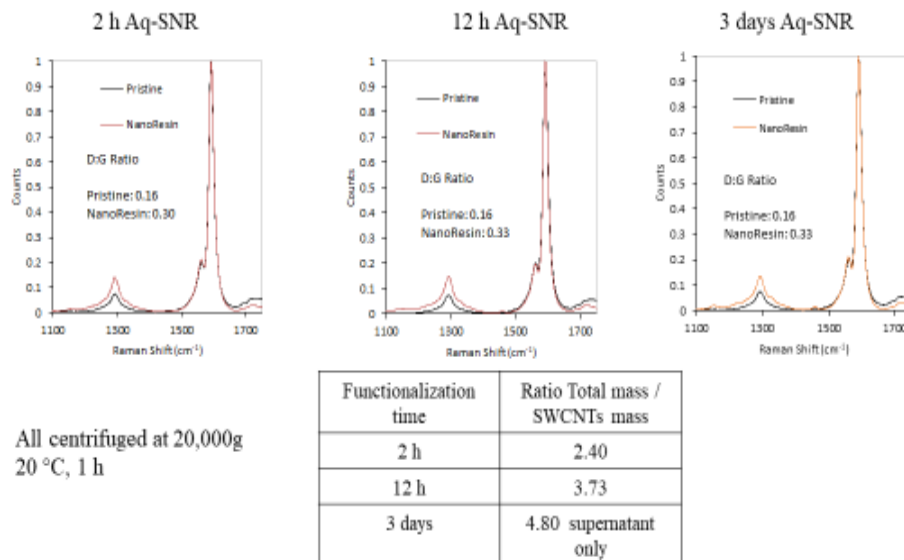


Figure S2.12: Baseline-Normalized Raman spectra of Pristine SWCNT compared to: 2h (left), 12h (center), and 3 day (right) Aq-SNR after centrifugation at 20,000 RCF for 1 h. Increase in the ratio of the area under the D and G bands (the D:G ratio) indicates covalent functionalization of ionomer strands to SWCNT wall. Total mass of Aq-SNR to SWCNT mass shown in table.

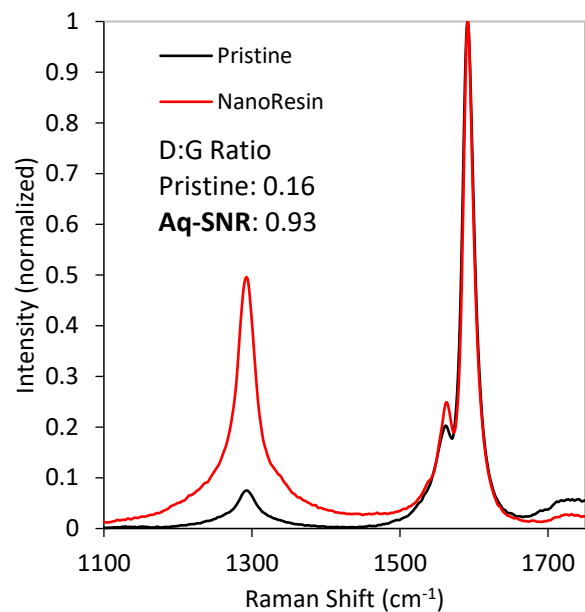
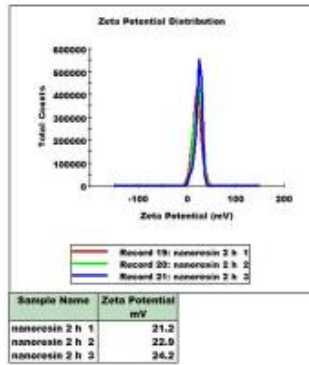
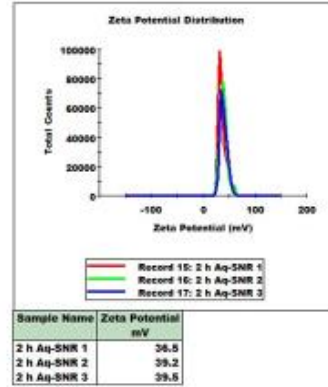


Figure S2.13: Baseline-Normalized Raman spectra of Pristine SWCNT and 3 day Aq-SNR after centrifugation at 200,000 RCF for 1 h. Increase in the ratio of the area under the D and G bands (the D:G ratio) indicates covalent functionalization of ionomer strands to SWCNT wall.

## DLS/Zeta analysis

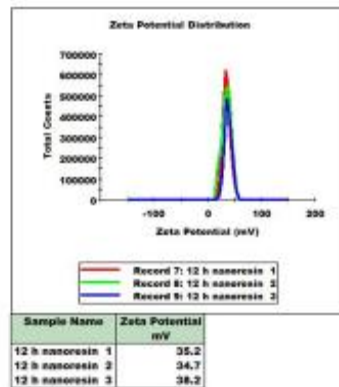


Before centrifugation

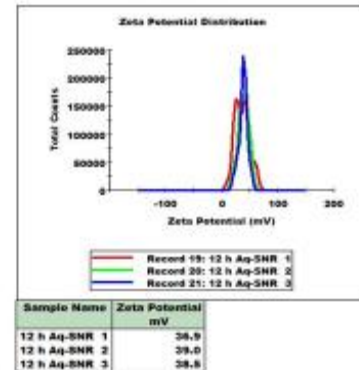


After centrifugation at 20,000 g

## DLS/Zeta analysis



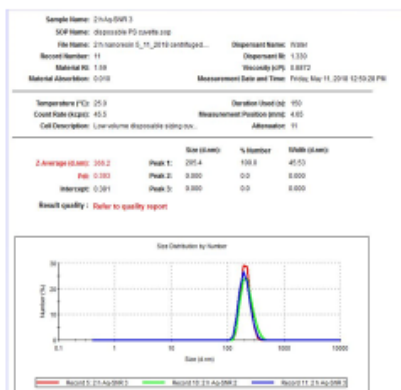
Before centrifugation



After centrifugation at 20,000 g

Figure S2.14: Zeta potential data for 2h (top) and 12h (bottom) functionalized Aq-SNR. Material from the supernatant after a 20,000 g centrifugation exhibit a more stable dispersion and higher zeta potential. All Zeta potentials were calculated from the measured electrophoretic mobility using the Smoluchowski model.

# DLS/Zeta analysis

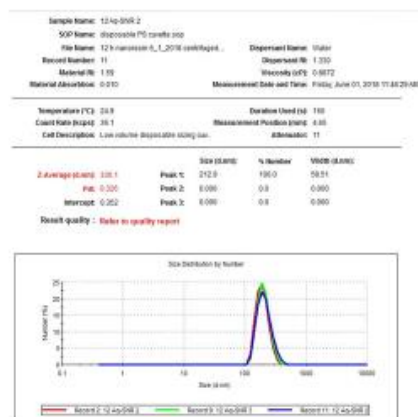


Number distributions of 2h Aq-SNR

Sample name	Hydrodynamic diameter (nm)
2 Aq-SNR 1 <sup>st</sup>	210.8
2 h Aq-SNR 2 <sup>nd</sup>	224.0
2 h Aq-SNR 3 <sup>rd</sup>	205.4

Centrifuged at 20,000g

Avg ± standard error: 213.4 ± 5.520 nm

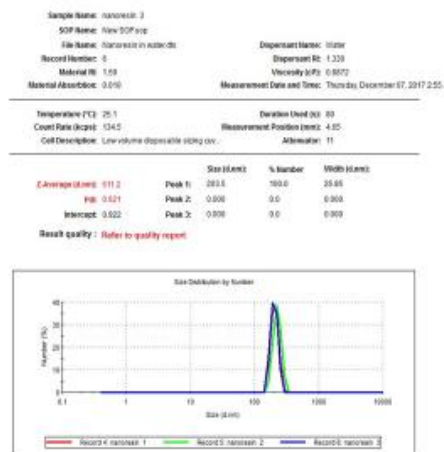


Number distributions of 12h Aq-SNR

Sample name	Hydrodynamic diameter (nm)
12 Aq-SNR 1 <sup>st</sup>	196.5
12 h Aq-SNR 2 <sup>nd</sup>	205.9
12 h Aq-SNR 3 <sup>rd</sup>	212.9

Centrifuged at 20,000g

Avg ± standard error: 205.1 ± 4.750 nm



Number distributions of 3 days Aq-SNR

Sample name	Hydrodynamic diameter (nm)
3 days Aq-SNR 1 <sup>st</sup>	208.6
3 days Aq-SNR 2 <sup>nd</sup>	226.8
3 days Aq-SNR 3 <sup>rd</sup>	203.5

Centrifuged at 20,000g

Avg ± standard error: 213.0 ± 7.070 nm

Figure S2.15: DLS data for 2h (top), 12h (middle) and 3 day (bottom) functionalized Aq-SNR. Material from supernatant after a 20,000 g centrifugation are consistent with a flexible rod model.

## Comparisons of NanoResins

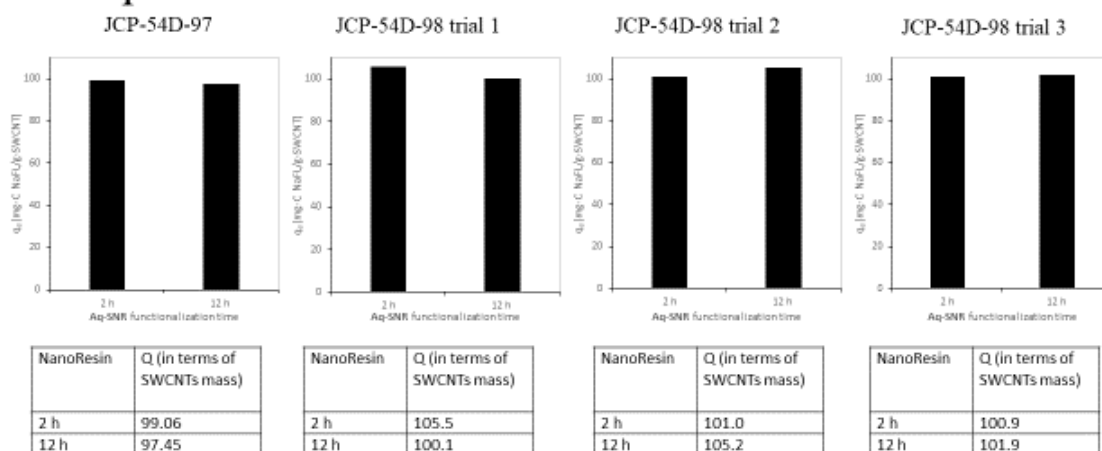


Figure S2.16: Equilibrium loading capacity of NaFL onto Aq-SNR using an initial concentration  $C_0 = 5.8$  mg-C/L. The mass of the adsorbent is the SWCNT mass only so we can directly compare the material based on number of nanotubes in the film. Value of  $q_e$  listed in tables.

Table S2.1: Adsorption of various analytes onto Aq-SNR thin films

<b>Adsorbate</b>	<b>Initial Conc. C<sub>i</sub> (mg-C/L)</b>	<b>Final Conc. C<sub>f</sub> (mg-C/L)</b>	<b>Adsorbate Volume (mL)</b>	<b>Mass of Adsorbate removed (mg)</b>	<b>Mass of Adsorbent (NanoResin) (mg)</b>	<b>q (mg-C adsorbate / g adsorbent)</b>
<b>NaFL</b>	5.49	3.79	3.00	5.11x10 <sup>-3</sup>	0.17	30.1
<b>PFOA</b>	4.31	1.82	3.00	7.47x10 <sup>-3</sup>	0.17	43.9
<b>PFOS</b>	5.07	1.41	3.00	1.09 x10 <sup>-2</sup>	0.17	64.6
<b>Tetracycline hydrochloride</b>	4.35	3.85	3.00	1.50x10 <sup>-3</sup>	0.17	8.82
<b>Carbenicillin disodium</b>	6.67	3.42	3.00	9.77x10 <sup>-3</sup>	0.17	57.5
<b>Bromoacetic acid</b>	3.41	1.87	3.00	4.65x10 <sup>-3</sup>	0.17	27.3
<b>Chloroacetic acid</b>	2.54	1.80	3.00	2.22x10 <sup>-3</sup>	0.17	13.1
<b>Bentazon</b>	6.81	3.93	3.00	8.66x10 <sup>-3</sup>	0.17	50.9
<b>Terbacil</b>	6.15	4.65	3.00	4.50x10 <sup>-3</sup>	0.17	26.5
<b>Bromacil</b>	5.55	3.90	3.00	4.95x10 <sup>-3</sup>	0.17	29.1

## CHAPTER 3

### GREEN SONOCHEMICAL SYNTHESIS, KINETICS AND FUNCTIONALIZATION OF NANOSCALE ANION EXCHANGE RESINS AND THEIR PERFORMANCE AS WATER PURIFICATION MEMBRANES

Abhispa Sahu, Rabia Sheikh, and Jordan C. Poler

#### Citation

Sahu, A.; Sheikh, R., Poler, J. C. Green sonochemical synthesis, kinetics and functionalization of nanoscale anion exchange resins and their performance as water purification membranes. *Ultrason Sonochem.* **2020**, *67*, 10  
10.1016/j.ultsonch.2020.105163

#### Keywords

Sonochemistry; Atom Transfer Radical Polymerization; kinetics; water purification; polyelectrolyte functionalized SWCNTs; Sustainable materials synthesis and reuse

#### Highlights

- Sonochemistry enables cost-effective, high-yield aqueous synthesis of polyelectrolytes and nanocomposites at low solution temperature.
- Kinetics and temperature dependence of sonochemically mediated atom transfer radical polymerization and aqueous nanostructure functionalization is quantified.
- Thin film membranes of nanocomposites demonstrated high adsorption capacity with fast adsorption kinetics and high Water Flux for water purification applications.

## Abstract

This paper reports on sonochemically catalyzed atom transfer radical polymerization (SONO-ATRP) polyelectrolyte synthesis and chain-end functionalization to single-walled carbon nanotubes (SWCNT). This all aqueous process is kinetically facile without use of initiator, or reducing agents and with very low concentrations of catalyst. The process achieves high functionalization density of polymer onto the SWCNTs. These functionalized nanoscale resins (NanoResins) exhibit high performance as fast and sustainable water purification materials. SONO-ATRP of vinyl benzyl trimethyl ammonium chloride (vbTMAC) was performed in aqueous medium resulting in short polyelectrolyte strands with high atom economy and high monomer conversions (93%) at room temperature using a thin probe sonicator ( $144 \text{ W cm}^{-2}$ , 20 kHz, for 4 h). Kinetics analysis showed first order kinetics with respect to monomer concentration in presence of or absence of sonication power. Low temperature SONO-ATRP functionalization of SWCNTs is achieved within two hours without added reducing agent while similar functionalization density using reducing agents without sonochemistry required 12 hours under reflux conditions. Functionalized NanoResin membranes were tested against surrogate analyte and demonstrated high performance Thomas Model breakthrough curves with a maximum adsorption capacity of  $139 \pm 1 \text{ mg g}^{-1}$  and water flux of  $692 \text{ L m}^{-2}\text{h}^{-1}\text{bar}^{-1}$  at one atmosphere pressure. Moreover, these materials are easily regenerated and reused without loss of performance or degradation.

### 3.1 Introduction

#### 3.1.1 Sonochemical ATRP

Atom transfer radical polymerization (ATRP) is an industrially significant polymerization processes that can be synergistically linked to sonochemistry for initiation, chain growth, and chain-end functionalization.<sup>1</sup> In a recent work, Matyjaszewski *et al.* demonstrated the efficient synthesis of methyl acrylate by SONO-ATRP in presence of initiator, Cu catalyst complex (CuBr<sub>2</sub>/tris(2-pyridylmethyl)amine (Cu/TPMA) and sodium carbonate in dimethyl sulfoxide solvent with 80% conversion in less than 2 h.<sup>2</sup> In another work, they used ultrasound to mediate aqueous ATRP without any additional conventional initiators or reducing agents and 40-4000 ppm levels of Cu/TPMA.<sup>3</sup> The proposed mechanism uses hydroxyl radicals, produced during sonolysis in aqueous medium, to regenerate deactivator species thereby replacing the role of reducing agent, required by the activators regenerated by electron transfer (ARGET) mechanism. Sonochemistry in reversible addition–fragmentation chain transfer (Sono-RAFT) polymerization in aqueous medium without any external radical initiator have also shown high monomer conversions.<sup>4,5</sup> To our knowledge we present the first demonstration of aqueous SONO-ATRP synthesis of polyelectrolytes and their subsequent functionalization onto pristine nanostructured carbon without addition of initiators, reducing agents, and at catalyst loading <5 ppm.

Polyelectrolytes are used in many applications, from biomaterials to water treatment,<sup>6-11</sup> ATRP has been an effective technique for grafting polymers from nanomaterial surfaces where surface initiated ATRP (SI-ATRP) is the most prevalent method.<sup>12-14</sup> Ikkala *et al.* functionalized poly(n-butyl acrylate) and poly(2-(dimethyl

amino)ethyl methacrylate) brushes on cellulose nanofibers using SI-ATRP. These nanocomposites demonstrated noticeable degradation on high grafting density of polymer brushes.<sup>15</sup> Recently, Héroguez *et al.* functionalized styrene and n-butyl acrylate onto cellulose nanocrystals using interface-initiated activator generated by electron transfer ATRP that led to stabilization of direct or inverted monomer emulsions produced under sonication.<sup>16</sup>

### 3.1.2 Ultrasonic debundling of nanomaterials

Aqueous sonochemical assisted functionalization of carbon and related nanostructures for sensors, drug delivery, and related biomedical applications has been reported.<sup>17-20</sup> In those examples, the role of sonication was to essentially debundle, disperse, or add functional moieties on surfaces of nanostructures for successful grafting in aqueous medium. In a recent work, Xu *et al.* prepared polyacrylonitrile grafted amino functionalized multi-walled carbon nanotubes nanocomposites in aqueous medium employing in situ polymerization in presence of initiator using ultrasonication horn for debundling, yielding a grafting content of 73.2% by weight.<sup>21</sup> Zhao *et al.* developed a green synthesis of chitosan modified amino functionalized graphene oxide under ultrasonication debundling to increase supercritical CO<sub>2</sub> penetration and reactivity.<sup>22</sup> Recently, Zhuiykov *et al.* prepared Se or Ag functionalized nanosheets of Ga<sub>2</sub>O<sub>3</sub> on surfaces of Galistan nanoparticles in aqueous medium for optoelectronic applications. The sonication power was effective at breaking native oxide layers and increasing reactivity due to the local heating effects.<sup>23</sup>

## 3.2 Materials and methods

### 3.2.1 Chemicals and Materials

All reagents were used as purchased without additional purification or modification. HiPCO (Grade P CNT, 0.8 – 1.2 nm diameter, 100 – 1000 nm length; Lot #P0276) SWCNT were used. Polymer synthesis chemicals: vinylbenzyl trimethylammonium chloride (vbTMAC) (Fisher, 97%; Lot #A0311318) monomer, copper(II) bromide (Acros, 99+%; Lot #A0344238), tris(2-pyridylmethyl)amine (TPMA) (TCI, >98.0%; Lot #Z8GMO-AD) for the catalyst, stannous octoate (SnOct) (Sigma-Aldrich, 92.5–100%, Lot #SLBP5072V) or ascorbic acid (AA) (Fisher Chemical, Lot #144594) for the reducing agents, 2-hydroxyethyl 2-bromo-isobutyrate (HEBiB) (Sigma-Aldrich, 95%, Lot #MKBW2607) as the initiator, 99.5% pure ethanol (Koptec, CAS #64-17-5). Other analytes include: sodium chloride (Mallinckrodt Chemical, Lot #E42589), sodium bromide (Fisher, Lot #067787) and disodium fluorescein (NaFL) (Sigma, Lot #BCBR1213V).

### 3.2.2 Workup and Purification

Workup and purification of the synthesis required: polypropylene membrane filters (0.45  $\mu\text{m}$  pore size, 47 mm wide, Lot #2075-5), nitrocellulose mixed ester (MCE) (Sterlitech Corp., Lot. # 31127255) with 0.45  $\mu\text{m}$  pore diameter and 13 mm width, 2 kDa MWCO dialysis membrane (Spectrum Labs, Lot. #3294218) 45 mm flat width and 29 mm diameter, and 50 kDa MWCO dialysis membrane (Spectrum Labs, Lot. #3292110) 34 mm flat width and 22 mm diameter. Membranes were activated by incubating for 10 minutes in Milli-Q water under constant stirring. Microcon® Centrifugal Filters (YM-100 lot# R1CN67003) 100 kDa MWCO were used to purify long polyelectrolytes.

### 3.2.3 ARGET ATRP synthesis of poly(vbTMAC)

Polymerization was performed using a Schlenk apparatus under Ar(g). TPMA (1.03 mg, 3.55  $\mu$ mol) and an aqueous CuBr<sub>2</sub> solution (34.5  $\mu$ l, 20.6 mM, 0.710  $\mu$ mol) were added into 1.0 mL of Milli-Q water to form the catalyst complex. Additional Milli-Q water (31.2 mL), vbTMAC (200.5 mg, 0.947 mmol) were added and fully dissolved. HEBiB (2.8  $\mu$ l, 19.3  $\mu$ mol) and ethanol (0.3% by volume) were then added. A temperature probe was immersed into the reaction mixture to monitor reaction temperature. The reaction mixture was sparged with Ar(g) for 20 minutes and then sealed. Aqueous AA solution (1.59 mM) was introduced at the rate of 20  $\mu$ l/min (32 nmol/min) and the reaction flask was heated/cooled in an oil/water-ice slush bath under reflux conditions for 2 h duration to study the influence of different temperatures. The reaction was then exposed to air to terminate the polymerization. 100  $\mu$ l samples were withdrawn with a syringe from the reaction mixture for proton nuclear magnetic resonance (<sup>1</sup>H NMR) analysis as a function of time. Activation parameters were calculated using Arrhenius and Eyring plots. All results are reported as values  $\pm$  standard error, 95% confidence.

#### 3.2.4 Sonochemically assisted ARGET ATRP poly(vbTMAC) syntheses (SONO-ARGET-ATRP)

Polymerization using ARGET-ATRP in combination with sonochemistry was performed using a Schlenk apparatus under Ar(g) with the opening for sonicator sealed around the probe. Materials and Methods similar to un-sonicated process in 2.3 above. See SI for detailed procedures.

#### 3.2.5 Sonochemically assisted ATRP initiation and propagation (SONO-ATRP-initiation and SONO-ATRP-propagation)

Materials and Methods similar to un-sonicated process in 2.3 above. See SI for detailed procedures. For SONO-ATRP-initiation polymerization, 60  $\mu\text{L}$  of stannous octoate was added and no initiator was used. For SONO-ATRP-propagation polymerization, HEBiB (10.3 – 20.6  $\mu\text{L}$ , 71.0 – 142  $\mu\text{mol}$ ) was added and no stannous octoate was used. The reaction mixture was sparged with  $\text{Ar}(\text{g})$  for 30 minutes and then sealed. Thin probe (0.111  $\text{cm}^2$ ) sonicator was used to initiate and propagate at different power intensities (36  $\text{W cm}^{-2}$ , 90  $\text{W cm}^{-2}$ , 135  $\text{W cm}^{-2}$ ). For SONO-ATRP-initiation, the reaction was sonicated under refrigerated bath ( $-2\text{ }^\circ\text{C}$ ) for two hours and then heated to reflux in a 110  $^\circ\text{C}$  oil bath for 13 h. For SONO-ATRP-propagation, the reaction heated to reflux in a 110  $^\circ\text{C}$  oil bath for one hour, resulting in 14% conversion and then sonicated under refrigerated bath ( $-2\text{ }^\circ\text{C}$ ) for 5 h. The reaction was then exposed to air and sonication was stopped to terminate the polymerization.

### 3.2.6 Sonochemically assisted ATRP poly(vbTMAC) synthesis (SONO-ATRP)

Materials and Methods similar to un-sonicated process in 2.3 above. See SI for detailed procedures. A temperature probe was immersed into the reaction mixture to monitor bulk solution temperature. Reducing agents and initiators were not used. The reaction mixture was sparged with  $\text{Ar}(\text{g})$  for 30 minutes and then sealed. The reaction was sonicated using probe sonicator. Reactions were performed using various power intensities (36  $\text{W cm}^{-2}$ , 81  $\text{W cm}^{-2}$ , 125.2  $\text{W cm}^{-2}$ ) under different temperatures each for two hours duration to measure the kinetics of SONO-ATRP polymerization. Thin probe sonicator was used to generate power intensities of 36 and 81  $\text{W cm}^{-2}$ , and thick probe (1.44  $\text{cm}^2$ ) used for 125  $\text{W cm}^{-2}$ . The reaction was then exposed to air and sonication was stopped to terminate the polymerization. 100  $\mu\text{l}$  samples were withdrawn

with a syringe from the reaction mixture for  $^1\text{H}$  NMR analysis as a function of time. The resulting polymer mixture was dialyzed overnight against Milli-Q water through a 2 kDa MWCO cellulose dialysis membrane in a Soxhlet extraction at reflux to remove any unreacted monomer and other reagents from the desired polyelectrolyte.

### 3.2.7 Aqueous sonochemically assisted ARGET ATRP functionalization of SWCNT NanoResin (Aq-SONO-ARGET ATRP-SNR)

Aq-SNR was synthesized in a one-step process. Short strands were synthesized by ARGET-ATRP then dispersed SWCNTs were added and the polymerization and functionalization proceeded in parallel. Materials and Methods similar to procedures above. See SI for detailed procedures. The reaction mixture was sparged with Ar(g) for 20 minutes, stannous octoate (30  $\mu\text{L}$ ) was added, then heated to reflux in a 110  $^\circ\text{C}$  oil bath for 10 min. Then, a 5.0 mL aliquot of the reaction mixture was removed and SWCNT (14.7 – 28.6 mg HiPCO) were sonicated in to disperse the tubes into the polymer solution (10 min, 36  $\text{W cm}^{-2}$ ) followed by ten min sparge under Ar(g). The small volume is more efficient than debundling in the larger reaction solution. SWCNT dispersion was added back into the polymerization reaction (10 – 20 min from the start of polymerization and ~10% conversion of monomer), re-sealed and sonicated at 117  $\text{W cm}^{-2}$  for (15 min – 2 h) duration while the reaction was held at room temperature. The sonication was stopped and the functionalization was exposed to air to quench the catalyst.

### 3.2.8 Aqueous sonochemically assisted ATRP functionalization of SWCNT NanoResin (Aq-SONO-ATRP-SNR) as function of reaction temperature

Aq-SNR was synthesized in a two-step process. First the polyelectrolytes were grown using ARGET-ATRP, then purified. Then the polymer strands were functionalized to the SWCNTs using SONO-ATRP. Materials and Methods similar to procedures above. See ESI for detailed procedures. The reaction temperature was maintained at reflux by an oil bath at 110 °C and polymer was grown for three hours resulting in 83-85% conversion. The reaction is then exposed to air to terminate the polymerization. The resultant mixture was centrifuged (200 000 RCF, 60 min, 20 °C) for 3 iterations. Polymer remained in the supernatant while oxidized Sn(OH)<sub>2</sub>(s), from the reducing agent, remained in the sediment. Centrifugation was stopped after no visible sedimentation of oxidized Sn(OH)<sub>2</sub>(s) was observed.<sup>11</sup> In a clean 3-necked Schlenk flask, TPMA (1.03 mg, 3.55 μmol) and CuBr<sub>2</sub> solution in water (34.5 μl, 20.6 mM, 0.710 μmol) were dissolved into 500 μL of Milli-Q water to activate the grown polymer. The purified polymer solution was then added and sparged with Ar(g) for 30 min. The different reaction temperatures (0 °C, 10 °C, 52 °C, 70 °C, 85 °C) were maintained using RTE-9 Endocal refrigerated circulating bath with coolant for below ambient temperatures and oil bath for above ambient temperatures. Then, a 5.0 mL aliquot of the reaction mixture was removed and SWCNT (15.02 mg HiPCO) were sonicated in to disperse the tubes into the polymer solution (10 min, 36 W cm<sup>-2</sup>) followed by five min sparge under Ar(g) and added back into the polymer solution, re-sealed again and sonicated at 117 W cm<sup>-2</sup>. The reaction was sonicated for 2 h at a set temperature. The sonication was stopped and the functionalization was exposed to air to quench the catalyst.

### 3.2.9 Purification of sonochemically functionalized NanoResins (Aq-SONO-ARGET ATRP-SNR and Aq-SONO-ATRP-SNR) and determination of percent functionalization

To purify Aq-SNR reaction mixtures, we added NaCl(s) to make 4M brine solution, sonicated for 10 min to detach physisorbed polymer strands and then centrifuged at 100,000 RCF at 20 °C for one hour. Unreacted reagents and physisorbed polymer stayed in the supernatant allowing Aq-SNR to be collected from the sediment. Supernatant was disposed of and this procedure was repeated until polymer detection limit in the supernatant reached <1 mg/L. The resulting dispersion of Aq-SNR was dialyzed overnight against Milli-Q water through a 2 kDa MWCO cellulose dialysis membrane in a Soxhlet extraction at reflux to remove any unreacted monomer, residual free polymer, salt, or other reagents from the dispersion of Aq-SNR. After overnight extraction, the stable dispersion was dialyzed against fresh MilliQ water in 1000 ml beaker for 2 h and conductivity of dialysate was measured to be  $\sim 1 \mu\text{S cm}^{-1}$  demonstrating removal of brine from Aq-SNR. Purified Aq-SNR was dispersed into known volume of Milli-Q water. Dispersions are stable for months. Concentration of SWCNT and total mass concentration was measured using our published procedures.<sup>11</sup>

### 3.2.10 Characterization techniques

Sonication experiments were performed under ultrasound irradiation using ultrasonic processor FS-450N or Fisher Scientific Sonic Dismembrator Model 100, both having frequency of 20 kHz. Monomer conversion was determined by <sup>1</sup>H NMR analysis using Oxford Instruments NMR AS500. Samples were withdrawn with a syringe from reaction mixture at known intervals to monitor growth kinetics. Each 80  $\mu\text{L}$  aliquot of

reaction mixture was mixed with 620  $\mu\text{L}$   $\text{D}_2\text{O}$ . Each  $^1\text{H}$  NMR spectra was recorded with 32 scans and 35 seconds relaxation time, following baseline correction. The percent monomer conversion is quantified using our published procedures.<sup>11</sup> The conversion was calculated by the decrease of monomer peak area relative to an internal standard peak area. Ethanol (triplet due to  $-\text{CH}_3$  group attached to  $-\text{CH}_2$  group, 1.01 ppm) was used as an internal standard. Pristine SWCNT or Aq-SNR were deposited as a thin films on 47 mm 0.45  $\mu\text{m}$  pore size polypropylene membrane filter using vacuum filtration. Kaiser Raman spectrometer with 785 nm laser was used for measuring integrated area under D band (disorder/diamonoid or  $\text{sp}^3$  hybridized C) and the G band (graphite or  $\text{sp}^2$  hybridized C). All Raman Spectra are baseline normalized and relative ratio between area under G and D bands is calculated. Since, we sonicated ARGET ATRP reagents with SWCNT for 2 h, hence, we performed control studies on pristine SWCNT along with ARGET ATRP reagents without monomer. We also analyzed D:G ratio for pristine SWCNT under different sonication durations (1 h, 2 h and 4 h) to analyze the effects of sonic irradiation on the D:G ratio of pristine SWCNT. All control studies and synthesis experiments were performed under same power per unit volume. As expected, D:G ratio increased for sonochemistry mediated functionalized SWCNT due to covalent functionalization.<sup>11,24</sup> Increasing sonication time did not significantly affect D:G ratio of pristine SWCNT. The hydrodynamic diameter and zeta potential of SONO-ATRP poly(vbTMAC), and 0  $^\circ\text{C}$  and 85  $^\circ\text{C}$  functionalized Aq-SONO-ATRP-SNR were measured using Malvern DLS Zetasizer instrument. 80  $\text{ng mL}^{-1}$  of poly(vbTMAC) and 10  $\text{ng mL}^{-1}$  of Aq-SONO-ATRP-SNR sample solutions were used for DLS measurements. Zeta potential measurements were performed using 2  $\text{mg/L}$  solution

samples. Sample cell temperature was maintained at 25 °C allowing an equilibrium time of 120 s. All results are reported as value  $\pm$  standard error, 95%.

### 3.2.11 Breakthrough studies

For breakthrough studies, 3 mg of total adsorbent mass (various Aq-SNR) were deposited as a thin film (4.63  $\mu\text{m}$  in height, 42.4 mm in width) on 47 mm 0.45  $\mu\text{m}$  pore size polypropylene membrane filter using vacuum filtration. Aqueous disodium fluorescein (NaFL) was used as analyte. The membrane holding the deposited Aq-SNR thin film was clamped firmly into the exit of the pressurized filtration unit. All breakthrough experiments were held at 1.39 bar (20.0 psi). Known concentration of aqueous NaFL (0.815 – 0.855  $\text{mg-C L}^{-1}$ ) was passed through the membrane with varying flow rates (3 – 15  $\text{mL min}^{-1}$ ). Effluent samples were collected at known intervals of time (and volume) until breakthrough saturation point is reached and were analyzed for NaFL concentration using UV-Vis Spectroscopy ( $\epsilon_{490} = 0.358 \pm 0.011 \text{ mg-C}^{-1} \text{ L cm}^{-1}$  at 490 nm). Breakthrough curves for NaFL adsorption by different Aq-SNR, were plotted as a function of effluent volume.

For regeneration of breakthrough curves, 3 mg of 2 h Aq-SONO-ATRP SNR was used. 0.2 L of brine solution (4.0 M NaCl(aq)) was flown through the freshly formed Aq-SNR film at flow rate of 3  $\text{ml min}^{-1}$  followed by washing with 0.2 L MilliQ water until the conductivity dropped down to  $<5 \mu\text{S cm}^{-1}$ . After measuring breakthrough capacity, the NaFL saturated films were regenerated by passing 4M NaCl(aq) brine until the concentration of desorbed NaFL solution dropped down below 0.04  $\text{mg-C L}^{-1}$ . Brine was removed by washing the Aq-SNR film with MilliQ water until the conductivity of

the effluent dropped below  $5 \mu\text{S cm}^{-1}$ . The procedure was repeated for 3 iterations. All  $k_T$  and  $q_e$  results are reported as values  $\pm$  standard error, 95% confidence.

### 3.3 Results and Discussion

Our results show that the ultrasound energy not only debundles the SWCNTs but also leads to enhanced reactivity and higher surface functionalization due to the sonochemically generated hydroxyl radicals in the aqueous system. Aqueous activators regenerated by electron transfer (ARGET)-ATRP requires reducing agents to maintain low catalysts loading ( $\sim 100$  ppm Cu/TPMA catalyst).<sup>25</sup> When combined with sonochemistry (SONO-ATRP), the mechanism facilitates polymerization without need of any external initiator, reducing agent or emulsifier and is kinetically facile with only  $<5$  ppm levels of Cu/TPMA catalyst. This current paper focusses on green SONO-ATRP that leads to fast growth kinetics and high chain-end functionalization onto the surface of SWCNTs resulting in excellent all aqueous nanostructured resin (Aq-SNR) membrane materials for water purification. We compare the kinetics of ARGET-ATRP to SONO-ARGET ATRP and SONO-ATRP and we compare percent functionalization of SWCNTs by SONO-ARGET-ATRP to SONO-ATRP processing. This work reports on a sustainable synthetic pathways for facile and green polymer synthesis and chain-end functionalization of nanostructured carbons.

#### 3.3.1 Sonochemical functionalization of SWCNTs

All aqueous SONO-ATRP reactions at all temperatures were performed without external reducing agent or initiator. Measured temperature of polymerization and functionalization reactions is of the reaction solution using an immersed thermocouple

probe. Actually, ultrasonic irradiation in aqueous medium generates cavitation bubbles that collapse to give rise to inhomogeneous local temperatures ( $\sim 5000$  °C) and high pressures ( $>500$  atm) resulting in localized short-lived adiabatic hot spots within the bubble and in the liquid surrounding the interfacial region.<sup>26-29</sup> This phenomena leads to sonolysis of water generating hydrogen/hydroxyl (H/OH) radicals that react with dissolved vinyl monomer to efficiently produce radicals at low frequency (20 kHz).<sup>26,28</sup> We found that a lower bulk temperatures leads to faster polymer growth and higher SWCNT functionalization. The kinetics and materials properties are discussed below.

### 3.3.2 Sonochemistry kinetics and NanoResin percent functionalization

As we have reported, ARGET-ATRP growth of poly(vbTMAC) is an efficient process.<sup>2</sup> The pseudo first order apparent rate constant measured at 19.5 °C bulk temperature without sonication was  $k_{app} = 3.0 \times 10^{-4} \text{ s}^{-1}$ . Whereas, the same reaction conditions at 19.5 °C bulk temperature with  $125.2 \text{ W cm}^{-2}$  sonic irradiation resulted in a significantly faster reaction with  $k_{app} = 3.2 \times 10^{-3} \text{ s}^{-1}$ . High temperature ARGET-ATRP growth at reflux where the bulk temperature was 106.2 °C, but without sonic irradiation yielded a  $k_{app} = 2.2 \times 10^{-3} \text{ s}^{-1}$ . We show that addition of sonic energy is more effective than simply raising the bulk temperature. In fact lowering the bulk temperature for all of our sonochemical processes increased the reaction rates. Additional polymerization kinetics data is listed in the Supplementary Information (SI).

The polyelectrolyte strands were then functionalized to SWCNTs. We measure the total mass of polymer plus the SWCNT scaffold by filtration of the dispersion onto a supporting membrane. The mass of the SWCNT in that volume of dispersion is determined from NIR absorption as described previously.<sup>11</sup> The ratio of total mass to the

SWCNT mass is proportional to the functionalization density (%Functionalization) for a given polyelectrolyte length. In Figure 3., we show the total mass to SWCNT mass for various functionalization processes.

Aq-ARGET-ATRP-SNR under high temperature reflux conditions (black bars - right) first received a 10 min low power sonication to debundle the SWCNTs and allow them to stay dispersed during the functionalization reaction.<sup>11</sup> The dispersed SWCNTs were then added back into the reaction solution for various functionalization times. During this time, the system was not being sonicated (ARGET-ATRP only) and the total-mass per SWCNT-mass ratio increased from 2.2 (120% polymer mass to SWCNT mass) after 2 h of reflux up to a ratio of 4.8 (380% polymer mass to SWCNT mass) after 3 days of refluxing functionalization. The y-intercept of %Functionalization versus time does not go through zero, so the 10 min sonication was also partially functionalizing the tubes.

Aq-SONO-ARGET ATRP-SNR and Aq-SONO-ATRP-SNR (green bars - left) did not receive any reflux conditions and the bulk temperature was kept near room temperature. We show here that sonicating SWCNT in polyelectrolyte for 25 min under ARGET-ATRP conditions at room temperature (Aq-SONO-ARGET-ATRP-SNR) and no additional reflux, resulted in a higher functionalization density (2.7 – 1<sup>st</sup> green bar ) than the 10 min sonication followed by 2h reflux (2.4 – 1<sup>st</sup> black bar). Increasing the sonication time of the Aq-SONO-ARGET ATRP-SNR experiment to 2 h we measured total-mass per SWCNT-mass ratio of 3.2 (2<sup>nd</sup> green bar ). The error bars on the data points are calculated by propagation of differential errors. The data labeled 2h SONO ATRP applied sonochemistry for 2 h to a reaction that did not include any reducing

agents and was held at 0 °C during the functionalization. The 2 h SONO-ATRP experiment was repeated four times and the 95% confidence interval error bars are shown.

We grew polymer for 40 min with initial molar ratio of [vbTMAC]:[HEBiB] = 35:1 in presence of reducing agent resulting in high monomer conversion (83-85 %). This polymer solution was then purified and subsequently used for Aq-SONO-ATRP-SNR functionalization at different temperatures without reducing agent added under sonic irradiation of 117 W cm<sup>-2</sup> for 2 h. In Figure 3., we show that decreasing the bulk temperature during Aq-SONO-ATRP-SNR functionalization leads to a higher %Functionalization. Aq-SONO-ATRP-SNR functionalization results at 52 °C (2 trials), and 70 °C were statistically the same and the data were combined. Functionalization below 0 °C was difficult because the aqueous solution started to solidify. The correlation coefficient from 9 trials is -0.64 which indicates significant dependence of %Functionalization versus decreasing temperature. This observation correlates with dependence of the temperature generated by the collapsing sono-cavitation bubble,  $T_{bubble}$  which is inversely proportional to the liquid's vapor pressure:

$T_{bubble} \propto T_{bulk} / P_{vapour}$ .<sup>30-31</sup> As the bulk temperature increases so does the vapor pressure of the water.

Stable radicals, like aryl diazonium salts, are known to react with the sidewalls or basal planes of graphenic carbon.<sup>32</sup> The reaction results in a stable tertiary radical on the carbon surface. Reaction of 2,2,6,6-tetramethylpiperidine-1-oxyl (TEMPO),<sup>33</sup> with the sp<sup>2</sup> C on the basal planes result in stable radical spin centers on the graphenic carbon that can then react with the primary radical at the living end of the poly(vbTMAC) chains as

described by the ATRP mechanism. Hydroxyl radicals, generated by sonolysis during aqueous SWCNT functionalization, play a similar role. At room temperature the aqueous hydroxyl radicals have a lifetime of  $\sim 6 \mu\text{s}$ ,<sup>34</sup> which is long enough to attack the sidewall of a SWCNT.

### 3.3.3 Sonochemistry kinetics and polymer percent conversion

Kinetics of ARGET-ATRP and SONO-ATRP of poly(vbTMAC) was measured at different temperatures in aqueous conditions and plotted as  $\ln([M]_0/[M])$ . Initial concentration  $[M]_0$  is set and  $[M]$  is measured from % conversion data versus time. The apparent propagation rate constants,  $k_{app}$  were calculated from slopes of  $\ln([M]_0/[M])$  vs time as shown in Figure 3.B. Additional kinetics are shown in the SI and. These data are consistent with a constant concentration of propagating radicals and first order kinetics with respect to monomer concentration in both the presence and absence of sonochemical irradiation.<sup>35</sup> The  $k_{app}$  values for ARGET-ATRP, SONO-ARGET-ATRP and SONO-ATRP at different temperatures and various power intensities are listed in. For all power intensities,  $k_{app}$  values of SONO-ATRP and SONO-ARGET-ATRP are smaller when the measured bulk temperature is higher. This is because at higher bulk temperatures, solvent vapor ‘cushions’ the sonic bubble collapse, leading to lower temperature hot spots.<sup>27-28</sup> This in turn affected the sonolysis efficiency and thereby decreased the formation rate of monomer radicals. This is consistent with our observations of the sonochemical functionalization of SWCNTs discussed above.

Low temperature (17.0 – 19.5 °C) SONO-ATRP and SONO-ARGET-ATRP reaction rates are higher than those measured from conventional ARGET-ATRP at similar temperatures (19.5 °C). With initial molar reagents ratio of

[vbTMAC]:[CuBr<sub>2</sub>]:[TPMA] = 1080:0.05:0.25 under SONO-ATRP 144 W cm<sup>-2</sup> is used, a 93% monomer conversion was achieved without reducing agent and initiator at room temperature within 4 h. To reach the same 93% conversion with the ARGET-ATRP under high temperature reflux conditions it took 37 h.

Without sonochemical irradiation, the polymer growth kinetics display simple Arrhenius behavior. Activation energy ( $E_a$ ), activation enthalpy ( $\Delta H$ ) and activation entropy ( $\Delta S$ ) were determined from Arrhenius ( $\ln k_{app}$  versus  $1/T$ ) and Eyring plots ( $\ln[k_{app}/T]$  versus  $1/T$ ) shown in Figure S3.3. Calculated  $E_a$  of poly(vbTMAC) for ARGET ATRP in aqueous medium is  $(+21.1 \pm 1.4)$  kJ mol<sup>-1</sup>, as shown in Figure S3.3A. This value is very similar to the activation energy of methacrylate type monomers in aqueous media.<sup>36</sup>  $\Delta H$  and  $\Delta S$  were calculated from slope and intercept of Eyring plot were  $(+18.3 \pm 1.41)$  kJ mol<sup>-1</sup> and  $(-249 \pm 14)$  J mol<sup>-1</sup>K<sup>-1</sup> respectively, as shown in Figure S3.3B.

With sonochemical irradiation, the polymer growth kinetics do not display Arrhenius behavior, whereas the reaction slows down at high bulk temperature. An apparent negative Arrhenius activation energy for poly(vbTMAC) using aqueous SONO-ATRP was calculated to be  $(-8.0 \pm 0.8)$  kJ mol<sup>-1</sup> using 36 W cm<sup>-2</sup> sonication intensity as shown in Figure S3.4. Similar negative Arrhenius activation energy have been reported in the literature. Ultrasonic initiation of styrene was reported to be  $-15$  kJ mol<sup>-1</sup><sup>31</sup> Apparent activation energy for ultrasonic initiation of methyl butyrate polymerization was reported to be  $-18.9$  kJ mol<sup>-1</sup><sup>30</sup> According to Kruss *et al.* the negative apparent  $E_a$  is consequence of using bulk monomer temperature in the Arrhenius plot instead of local cavitation temperature resulting from reversible adiabatic hot

spots.<sup>29,30</sup> They analyzed hydroxyl radical formation rate as a function of vapor pressure. Combining the Arrhenius equation with the large rise in local temperature during the reversible adiabatic collapse of the cavitation bubble, results in a positive value of  $E_a$ . The modified Arrhenius equation is:  $\ln(k) = \ln(A) - \frac{E_a P_{vapor}}{RT_{bulk} P_a^{(\gamma-1)}}$ , where  $k$  is the observed rate constant ( $s^{-1}$ ),  $A$  is pre-exponential factor obtained from y-intercept,  $P_{vapor}$  is liquid vapor pressure,  $R$  is universal gas constant,  $P_a$  is the pressure in the bubble at start of its collapse,  $\gamma$  is ratio between specific heat at constant pressure and specific heat at constant volume ( $C_p/C_v$ ) and  $T_{bulk}$  is measured bulk temperature of the reaction solution. Using the known vapor pressure of water at the measured bulk temperature (i.e.,  $P_{vapor} = 0.031$  atm when  $T_{bulk} = 298$  K) and the known adiabatic index for water  $\gamma = 1.32$ , where Kruss *et al.* assumed the value of  $P_a$ . While this is outside the scope of this paper an estimate of  $P_a = 1$  atm, results in a calculated  $E_a = +24.6$  kJ mol<sup>-1</sup> which is consistent with similar ATRP mechanisms with sonochemical irradiation. In addition to faster kinetics, the sonochemical polymerization of poly(vbTMAC) and its subsequent sonochemical functionalization to SWCNTs requires significantly less energy than the high temperature reflux conditions.

### 3.3.4 Sonochemical polymerization and control studies

Sonochemical assisted polymerization results in highly controlled molecular weight distributions. Kubo *et al.* measured a polydispersity index (PDI) below 1.3 when poly(2-hydroxymethyl methacrylate) was synthesized for 4 h under an ultrasonication intensity similar to ours (150–300 W dm<sup>-3</sup>).<sup>37</sup> To test the stability of poly(vbTMAC) against sonic irradiation we grew long polymers and measured the effective hydrodynamic radius of the strands. SONO-ATRP of poly(vbTMAC) polyelectrolyte

strands grown to 93% conversion, had a measured hydrodynamic radius  $R_h$  of  $11.1 \pm 1.3$  nm (see DLS data in Table S3.1 and Figure S3.5). Polyelectrolytes like proteins having a molecular weight range of 150 – 300 kDa have typical  $R_h$  values of 7 – 15 nm. Moreover, the polymer solution was spun through a 100 kDa MWCO filter (10,000 g for 20 min). The retentate was re-suspended in water and found to contain the poly(vbTMAC). The absolute molar mass of the polymer was determined to be  $208.9 \pm 1.7$  kDa, by Size Exclusion Chromatography – Multi Angle Light Scattering (SEC-MALS by Wyatt Technology). The polydispersity index (PDI) was measured to be 1.5, confirming that sonication does not result in the cutting of the long chain polymer strands formed during SONO-ATRP, consistent with Kubo *et al.* The radius of gyration  $R_g$  was measured to be  $23.0 \pm 0.1$  nm. The ratio of  $R_g/R_h$  is indicative of the particle's shape. When  $R_g/R_h = 0.778$  the particle is characterized as a hard sphere.<sup>38</sup> For the SONO-ATRP poly(vbTMAC) we measured a  $R_g/R_h = 1.9$ . This ratio is lower than that for a rigid rod ( $R_g/R_h \sim 2.2$ ) and suggests that the polyelectrolyte brushes exhibit a prolate-ellipsoidal shape in water.<sup>39,40</sup> This result is consistent with our molecular mechanics geometry optimization of the polymer brush attached to a SWCNT cluster, as shown in Figure 3. below.

While outside the scope of this work, the role of the hydroxyl radical during sonochemical polymerization was measured. From Matyjaszewski *et al.* we know that the hydroxyl radicals are effective at propagating the polymerization. We explored the effect of hydroxyl radicals on the initiation process too. In Table 3.1, we list % conversion data for two different mechanisms as a function of sonication power. Control experiments using the ARGET-ATRP mechanism with no sonication after 13 h reflux

with the same [vbTMAC]:[CuBr<sub>2</sub>]:[TPMA], +Reducing agent, and +Initiator yielded 78.4% conversion. During SONO-ATRP-I we do not add any initiator (-Initiator) and explore the role of the hydroxyl radicals on the initiation step. Without any initiator added we sonicated the reaction for 2 h under various power, followed by turning off the sonicator and heating the reaction at reflux for an additional 13 h. Control experiments under the same conditions (+Reducing agent, -Initiator, 5h reflux) but without sonic irradiation yielded no detectable polymerization (% conversion = 0). But after only 2 h of sonication, the SONO-ATRP-I mechanism yielded up to 93% conversion. Therefore, sonochemical addition of hydroxyl radicals acts to initiate the polymerization of vbTMAC. Once polymer strands are formed during the first 2 h of sonication, they continue to grow during reflux (no SONO) because of the added reducing agent. Moreover, the % conversion is proportional to the square root of the sonication power which is consisted with Price *et al.* studies of sonochemical initiation for poly(methyl methacrylate).<sup>30</sup>

During SONO-ATRP-P we do not add any reducing agent (-Reducing) and explore the role of the hydroxyl radicals in the propagation step. The solution is heated to reflux without sonication for 1 h to initiate growth. After the reaction was cooled to room temperature, the solution was sonicated for 5 h, yielding up to 55% conversion. Control experiments under the same conditions (-Reducing agent, +Initiator, no SONO) yielded 14% conversion after 1 h of reflux (and 19% conversion after 6 h of reflux) as expected for standard aqueous ATRP growth of poly(vbTMAC). Clearly, the sonochemical addition of hydroxyl radicals also increases the propagation step in the mechanism, as described by Matyjaszewski *et al.*

### 3.3.5 Covalent functionalization to SWCNTs

In previous works we grew short poly(vbTMAC) (~10 kDa) in dimethyl formamide (DMF) and then sonicated SWCNTs into the purified polymer solution. The tubes were dispersed into the DMF, but since there was no catalyst or reducing agents, the physisorbed polyelectrolyte strands were easily removed by brine and centrifugation.<sup>10</sup> During sonication we produce methyl radicals in the DMF.<sup>41</sup> Since there was no covalent attachment under SONO-ATRP conditions in DMF, the methyl radicals do not seem to be as effective at creating a stable tertiary radical on the SWCNT sidewall. We monitored the reactivity of the sidewall carbons by measuring the D:G ratio from Raman spectroscopy.<sup>11</sup>

The increase of the ratio between area under D and G bands for Aq-SNR as compared to pristine SWCNTs is a measure of the increase in  $sp^3$  hybridized C resulting from the covalent attachment of the polyelectrolyte brush polymers (as shown in Table 3.2). Aq-SNR samples were centrifuged at 200,000 g for 1 h at 20 °C and the supernatant was analyzed by Raman Spectroscopy. It is observed that 2 h Aq-SONO-ARGET-ATRP-SNR functionalized at room temperature results in a D:G = 0.35. This material had a %Functionalization of 3.2. After 10 min SONO and 2 h reflux without sonochemistry (see Figure 3. above) the D:G = 0.30 and the material had a %Functionalization of 2.4. Control studies of sonic irradiation (1 – 4 h) on pristine SWCNT (with and without reagents –monomer) showed a small increase in D:G ratio. Two hours SONO-ARGET ATRP-SNR and two hours SONO-ATRP-SNR (without reducing agent) have similar %Functionalization (D:G ratio = 0.35). This is consistent with our observations that hydroxyl radicals contribute to both propagation and initiation.

Our data suggest that sonochemically derived hydroxyl radicals lead to short - lived reactive surface sites, which are then attacked by the living end of the polyelectrolyte radical species at the SWCNT surface, even without the presence of added reducing agent. 2 h functionalized Aq-SONO-ATRP-SS-SNR has highest D:G ratio (0.36). This is a one pot reaction in which the SWCNTs are added before the strands grow to the prescribed length. Therefore, there are many more short strands with lower steric hindrance able to attack the active sites on the SWCNTs. Conversely, longer strands physisorb to or wrap around the tubes, which hinders covalent attachment due to steric crowding of the surface sites.

The zeta potential of 0 °C and 85 °C functionalized Aq-SONO-ATRP-SNR was measured before and after centrifugation of the dispersions. Centrifugation was performed at 20,000 g for 20 minutes at 20 °C, and the supernatant was diluted to 2 mg/L. As shown in Table S3.1 and Figure S3.6 – Figure S3.9, the zeta potential of functionalized NanoResin particles after centrifugation was higher than Aq-SNR without centrifugation. Nanoresins that are more debundled and have higher %Functionalization are more difficult to remove by centrifugation. This is consistent with a higher surface charge from attached polyelectrolytes and the resulting higher electrophoretic mobility. We observed that the zeta potential of 85 °C functionalized Aq-SONO-ATRP-SNR was higher than the 0 °C functionalized Aq-SONO-ATRP-SNR, with and without centrifugation, even though the %Functionalization is higher in 0 °C Aq-SONO-ATRP-SNR. The measured hydrodynamic diameter (as shown in Table S3.1, and Figure S3.10 and Figure S3.11) of the 0 °C functionalized Aq-SONO-ATRP-SNR ( $261.5 \pm 1.428$  nm) was higher than the 85 °C functionalized Aq-SONO-ATRP-SNR ( $220.6 \pm 1.576$  nm).

The effective hydrodynamic diameter of Aq-SNR is modeled as a rigid rod, as discussed in our previous publications.<sup>10,11</sup> The zeta potential is calculated from electrophoretic mobility using the Smoluchowski model. The larger 0 °C NanoResin particles have a lower mobility due to their higher mass resulting in lower translational diffusion coefficient (from Einstein-Stokes relation), smaller electrophoretic mobility and therefore smaller calculated zeta potential.

### 3.3.6 Nanoscale Anion Exchange Resins for Water Purification

We have already demonstrated the effectiveness of our nanoresins toward the removal of several classes of contaminants found in natural water resources.<sup>11</sup> In order to assess the potential for Aq-SNR as point-of-use membrane water purifiers, breakthrough testing was analyzed. The influence of sonochemistry assisted functionalization durations (25 min and 2 h SONO-ARGET ATRP functionalization) and different Aq-SNR synthesis mechanisms (SONO-ARGET ATRP and SONO-ATRP) were studied using breakthrough curves (shown in Figure S3.12 and Table S3.2). The non-linear form of Thomas Model<sup>42-44</sup> which can be expressed as:

$$\frac{[\text{NaFL}]}{[\text{NaFL}]_0} = \frac{1}{1 + e^{\frac{k_T}{Q} [q_e M - [\text{NaFL}]_0 V_{\text{eff}}]}}$$

was used to measure the kinetic parameters of the breakthrough curves of Aq-SNR membranes where  $[\text{NaFL}]$  ( $\text{mg-C L}^{-1}$ ) is concentration of adsorbate in the effluent,  $[\text{NaFL}]_0$  ( $\text{mg-C L}^{-1}$ ) is the initial concentration of adsorbate in the feed solution,  $k_T$  ( $\text{L mg}^{-1} \text{min}^{-1}$ ) is Thomas rate constant,  $q_e$  ( $\text{mg g}^{-1}$ ) is continuous flow or equilibrium adsorption capacity,  $Q$  ( $\text{mL min}^{-1}$ ) is volumetric flow rate,  $M$  is mass of adsorbent (g),  $t$  is time (min) and  $V_{\text{eff}}$  (L) is throughput volume. In Figure 3., we show two representative

breakthrough curves comparing short strand (one pot) NanoResin to longer strand (one pot, 30-mers) nanoresin. We have not yet optimized the length and mass of polyelectrolyte functionalization to achieve the best breakthrough curves. 2 h functionalized Aq-SONO-ATRP-SS-SNR data shown in red in Figure 3. has a total mass to SWCNT mass ratio of 1.42. Whereas the 2 h functionalized Aq-SONO-ARGET-ATRP-SNR has a total mass to SWCNT mass ratio of 3.24. Despite the larger polymer functionalization, the analyte breaks through the membrane sooner. The D:G ratio of the short strand NanoResin material is higher than the D:G ratio of the longer strand material indicating more sites along the SWCNT wall have been functionalized, but with shorter, less mass, polyelectrolyte brushes. The water flux through a 42.2 mm wide and 4.63  $\mu\text{m}$  thick membrane made from the short strand 2 h functionalized Aq-SONO-ATRP-SS-SNR NanoResin was  $692 \text{ L m}^{-2} \text{ h}^{-1} \text{ bar}^{-1}$  at 1 atm pressure. This flux is more than seven times higher than that of a graphene oxide membrane (thickness  $< 1 \mu\text{m}$ ) with water flux of  $95 \text{ m}^2 \text{ h bar}^{-1}$  at 1 atm pressure.<sup>45</sup> Therefore, these Aq-SNR membranes can be tailored to optimize both, good mechanical stability, high flux, and high adsorption capacity.

It may be possible to optimize the performance of these materials with regard to maximum flux,  $Q$ , and removal capacity,  $q_e$ . In Figure 3., we show the effective volume to reach 10% breakthrough as a function of the total mass to SWCNT mass ratio (%Functionalization). The 10% breakthrough volume is a metric that characterizes how easily the analyte can access and then bind to the quaternary ammonium sites on the polymer brushes. Shorter brushes will have more accessible binding sites. Also the brushes have more space to pack closer to the SWCNT within the thin film. Our

observation that the flux for short strand NanoResin is lower than it is for the longer strand material is consistent with this model. Longer strands do not allow close packing of the nanotubes, thereby increasing the water flux. Molecular dynamics calculations on functionalized graphene sheets shows similar phenomena where the flux increases as the space between the nanostructured carbon scaffold increases<sup>46</sup> Further computational studies of the fluid flow through NanoResin materials are needed and outside the scope of this work.

We have observed a general trend that as the %Functionalization of the NanoResin increases, the maximum equilibrium loading  $q_e$ , calculated from the Thomas model fitting, also decreases. This observation implies that the analyte is unable to access some of the binding sites in the thin film material. In Figure 3., we illustrate how these observations can be explained. Molecular mechanics calculations (Materials Studio, Forcite – Compass force field) started with an individual (7,7) SWCNT and a poly(vbTMAC) strand 30 monomer units long covalently functionalized to the tube. The length of the SWCNT was set to reach a total mass to SWCNT mass of 1.5 as shown in Figure 3. (left). The backbone of the randomized polyelectrolyte is shown in magenta (Figure 3. – bottom right). To model a %Functionalization = 3, four of these strands were functionalized to the same SWCNT, as shown in Figure 3.(right). After the cluster was geometry optimized it was placed in a 3D periodic cell. The cell lattice constants were minimized to reach closest contact between the polymer – tube (left) or polymer – polymer (right). Depending on the flow profile, it seems that the analyte can easily access most of the binding sites in the model on the left but not in the model on the right.

Regeneration and reusability of 2 h functionalized Aq-SONO-ATRP-SNR (two pot, 30-mer) NanoResin was performed to estimate long term stability of these thin films. We tested breakthrough behavior of Aq-SNR for 3 cycles (as shown in Figure S3.13). We found that the Thomas model does not fit the data from the regenerated films as well the initial breakthrough. The 10% breakthrough volume was measured and the equilibrium loading  $q_e$  per cycle was estimated from the saturation of the measured loading  $q$  shown in Figure 3.1. After three breakthrough – regeneration cycles, the 10% breakthrough volume did not change after the first two cycles and showed some decrease in the third ( $V_{\text{eff}}$  at 10% was  $0.21 \pm 0.02$ ,  $0.21 \pm 0.02$ , and  $0.18 \pm 0.02$  L for the 1<sup>st</sup>, 2<sup>nd</sup>, and 3<sup>rd</sup> reuse respectively). The loading data for the first three regeneration cycles shown in Figure 3.1 lay on top of each other for the first 200 mL. The capacity of the film seems to fall off after regeneration in brine from 103 (mg NaFL/g SWCNT) in the first breakthrough to 101 (mg NaFL/g SWCNT) in the second and finally 97 (mg NaFL/g SWCNT) in the third breakthrough. This 2% per cycle decrease is quite small, similar to other regenerated anion exchange materials.<sup>47,48</sup>

Images of the initial NanoResin film and the film after the 3<sup>rd</sup> regeneration, shown in Figure 3.2, demonstrate that the film is structurally intact with no cracks or pin holes even after multiple uses and over 5.0 L of feed solution (NaFL solution, brine regeneration media, and water). These films were exposed to turbulent flow each time the flow cell was refilled with liquid. There is no evidence that any nanostructured carbon released from the film surface or passed through the polypropylene support. Subsequent soaking of the unmounted membranes in water for more than a month did not result in any delamination or material loss. The yellow tinge of the film after

breakthrough is from the NaFL adsorption. This tinge is not observed after the film is regenerated with 4M NaCl brine.

### 3.4 Conclusions

We have developed a novel SONO-ATRP process without use of any external radical initiator or reducing agents and while using only a few ppm of catalyst complex.

Polyelectrolyte strands with high monomer conversion were synthesized with SONO-ATRP using thin probe sonicator at 25 °C. DLS and SEC-MALS analysis demonstrated long polyelectrolyte strands with low polydispersity. Kinetic plots exhibit linear semilogarithmic behavior with respect to monomer concentration. Apparent  $E_a$  of poly(vbTMAC) for radical initiation and polymerization using ARGET ATRP and SONO-ATRP have been determined, and are consistent with the literature values.

Negative  $E_a$  is the result of using bulk solution temperatures instead of local cavitation bubble temperatures. We successfully performed high-density functionalization of polyelectrolyte anion exchange resin strands onto SWCNT sidewalls using the described SONO-ATRP process while at low reaction temperatures thereby providing a less energy intensive alternative for green chemistry ATRP processes across several industrial applications. Total-mass per SWCNT-mass determination and Raman spectroscopy analysis demonstrate high density functionalization of polyelectrolyte stands onto the surface of SWCNTs after only 2 h of low temperature sonication. Finally, we demonstrated breakthrough properties of these ion exchange adsorbent membranes that exhibit good  $q_e$  values and 10% breakthrough volumes. High water flux through thicker Aq-SNR films is significantly larger than that through thinner graphene oxide membranes. Therefore, these materials can remove contaminants from water with a

higher loading capacity, less contact time, and lower transmembrane back pressures. Finally, these Aq-SNR membranes can be easily regenerated, and they do not significantly degrade or lose performance after multiple cycles. Atom efficient, energy minimized manufacturing, coupled with regeneration and reusability are central to developing sustainable next-generation nanomembrane water purification systems.

#### Declaration of Competing Interest

The authors declare that they have no known competing financial interests or personal relationships that could have appeared to influence the work reported in this paper.

#### Acknowledgments

The research work of Abhispa Sahu was supported by The Graduate School Summer Fellowship Program (2019), The Graduate Assistant Support Plan (2016-21) and Nanoscale Science Program at the University of North Carolina at Charlotte. We thank Wyatt Technology for their assistance with SEC-MALS data. We thank Dr. Juan Vivero-Escoto for use of his DLS and zeta potential instrumentation.

### 3.5 References

- [1] T.G. McKenzie, F. Karimi, M. Ashokkumar, G.G. Qiao, Ultrasound and Sonochemistry for Radical Polymerization: Sound Synthesis, *Chem.-Eur. J.*, 25 (2019) 5372-5388.
- [2] Z.H. Wang, F. Lorandi, M. Fantin, Z.Y. Wang, J.J. Yan, Z.H. Wang, H.S. Xia, K. Matyjaszewski, Atom Transfer Radical Polymerization Enabled by Sonochemically Labile Cu-carbonate Species, *Acs Macro Letters*, 8 (2019) 161-165.
- [3] Z.H. Wang, Z.H. Wang, X.C. Pan, L.Y. Fu, S. Lathwal, M. Olszewski, J.J. Yan, A.E. Enciso, Z.Y. Wang, H.S. Xia, K. Matyjaszewski, Ultrasonication-Induced Aqueous Atom Transfer Radical Polymerization, *Acs Macro Letters*, 7 (2018) 275-280.
- [4] T.G. McKenzie, E. Colombo, Q. Fu, M. Ashokkumar, G.G. Qiao, Sono-RAFT Polymerization in Aqueous Medium, *Angew. Chem.-Int. Edit.*, 56 (2017) 12302-12306.
- [5] S. Pioge, T.N. Tran, T.G. McKenzie, S. Pascual, M. Ashokkumar, L. Fontaine, G. Qiao, Sono-RAFT Polymerization-Induced Self-Assembly in Aqueous Dispersion: Synthesis of LCST-type Thermosensitive Nanogels, *Macromolecules*, 51 (2018) 8862-8869.
- [6] C.S. Peyratout, L. Dahne, Tailor-made polyelectrolyte microcapsules: From multilayers to smart containers, *Angew. Chem.-Int. Edit.*, 43 (2004) 3762-3783.
- [7] D.A.Z. Wever, F. Picchioni, A.A. Broekhuis, Polymers for enhanced oil recovery: A paradigm for structure-property relationship in aqueous solution, *Progress in Polymer Science*, 36 (2011) 1558-1628.
- [8] F. Nabeel, T. Rasheed, M. Bilal, H.M.N. Iqbal, Supramolecular membranes: A robust platform to develop separation strategies towards water-based applications, *Sep. Purif. Technol.*, 215 (2019) 441-453.
- [9] X.R. Hu, M.J. Feeney, E. McIntosh, J. Mullahoo, F. Jia, Q.B. Xu, S.W. Thomas, Triggered Release of Encapsulated Cargo from Photoresponsive Polyelectrolyte Nanocomplexes, *ACS Appl. Mater. Interfaces*, 8 (2016) 23517-23522.

- [10] B.R. Johnson, T.B. Eldred, A.T. Nguyen, W.M. Payne, E.E. Schmidt, A.Y. Alansari, J.E. Amburgey, J.C. Poler, High-Capacity and Rapid Removal of Refractory NOM Using Nanoscale Anion Exchange Resin, *ACS Applied Materials & Interfaces*, 8 (2016) 18540-18549.
- [11] A. Sahu, K. Blackburn, K. Durkin, T.B. Eldred, B.R. Johnson, R. Sheikh, J.E. Amburgey, J.C. Poler, Green synthesis of nanoscale anion exchange resin for sustainable water purification, *Environ. Sci.-Wat. Res. Technol.*, 4 (2018) 1685-1694.
- [12] C.J. Fristrup, K. Jankova, S. Hvilsted, Surface-initiated atom transfer radical polymerization-a technique to develop biofunctional coatings, *Soft Matter*, 5 (2009) 4623-4634.
- [13] C.M. Hui, J. Pietrasik, M. Schmitt, C. Mahoney, J. Choi, M.R. Bockstaller, K. Matyjaszewski, Surface-Initiated Polymerization as an Enabling Tool for Multifunctional (Nano-)Engineered Hybrid Materials, *Chem. Mat.*, 26 (2014) 745-762.
- [14] J.O. Zoppe, N.C. Ataman, P. Mocny, J. Wang, J. Moraes, H.A. Klok, Surface-Initiated Controlled Radical Polymerization: State-of-the-Art, Opportunities, and Challenges in Surface and Interface Engineering with Polymer Brushes, *Chemical Reviews*, 117 (2017) 1105-1318.
- [15] M. Morits, J.R. McKee, J. Majoinen, J.M. Malho, N. Houbenov, J. Seitsonen, J. Laine, A.H. Groschel, O. Ikkala, Polymer Brushes on Cellulose Nanofibers: Modification, SI-ATRP, and Unexpected Degradation Processes, *ACS Sustain. Chem. Eng.*, 5 (2017) 7642-7650.
- [16] A. Werner, V. Schmitt, G. Sebe, V. Heroguez, Convenient Synthesis of Hybrid Polymer Materials by AGET-ATRP Polymerization of Pickering Emulsions Stabilized by Cellulose Nanocrystals Grafted with Reactive Moieties, *Biomacromolecules*, 20 (2019) 490-501.
- [17] S.S. Maktedar, S.S. Mehetre, G. Avashthi, M. Singh, In situ sonochemical reduction and direct functionalization of graphene oxide: A robust approach with thermal and biomedical applications, *Ultrason. Sonochem.*, 34 (2017) 67-77.
- [18] Y.S. Li, Y.N. Song, Z. Ma, S. Niu, J.H. Li, N. Li, Synthesis of phosphonic acid silver-graphene oxide nanomaterials with photocatalytic activity through ultrasonic-assisted method, *Ultrason. Sonochem.*, 44 (2018) 106-114.

- [19] H. Hashemi, H. Namazi, Sonochemically synthesized blue fluorescent functionalized graphene oxide as a drug delivery system, *Ultrason. Sonochem.*, 42 (2018) 124-133.
- [20] S.S. Maktedar, G. Avashthi, M. Singh, Ultrasound assisted simultaneous reduction and direct functionalization of graphene oxide with thermal and cytotoxicity profile, *Ultrason. Sonochem.*, 34 (2017) 856-864.
- [21] H.L. Zhang, L. Quan, A.J. Gao, Y.P. Tong, F.J. Shi, L.H. Xu, The Structure and Properties of Polyacrylonitrile Nascent Composite Fibers with Grafted Multi Walled Carbon Nanotubes Prepared by Wet Spinning Method, *Polymers*, 11 (2019) 13.
- [22] J.F. Jia, Y.Z. Gai, W.C. Wang, Y.P. Zhao, Green synthesis of biocompatible chitosan-graphene oxide hybrid nanosheet by ultrasonication method, *Ultrason. Sonochem.*, 32 (2016) 300-306.
- [23] M. Karbalaei Akbari, Z. Hai, Z. Wei, R.K. Ramachandran, C. Detavernier, M. Patel, J. Kim, F. Verpoort, H. Lu, S. Zhuiykov, Sonochemical functionalization of the low-dimensional surface oxide of Galinstan for heterostructured optoelectronic applications, *Journal of Materials Chemistry C*, 7 (2019) 5584-5595.
- [24] S.M. Bachilo, M.S. Strano, C. Kittrell, R.H. Hauge, R.E. Smalley, R.B. Weisman, Structure-assigned optical spectra of single-walled carbon nanotubes, *Science*, 298 (2002) 2361-2366.
- [25] A. Simakova, S.E. Averick, D. Konkolewicz, K. Matyjaszewski, Aqueous ARGET ATRP, *Macromolecules*, 45 (2012) 6371-6379.
- [26] M. Bradley, F. Grieser, Emulsion polymerization synthesis of cationic polymer latex in an ultrasonic field, *J. Colloid Interface Sci.*, 251 (2002) 78-84.
- [27] K.S. Suslick, G.J. Price, Applications of ultrasound to materials chemistry, *Annual Review of Materials Science*, 29 (1999) 295-326.
- [28] G.J. Price, L. Garland, J. Comina, M. Davis, D.J. Snell, P.J. West, Investigation of radical intermediates in polymer sonochemistry, *Res. Chem. Intermed.*, 30 (2004) 807-827.

- [29] P. Kruus, T.J. Patraboy, INITIATION OF POLYMERIZATION WITH ULTRASOUND IN METHYL-METHACRYLATE, *J. Phys. Chem.*, 89 (1985) 3379-3384.
- [30] G.J. Price, D.J. Norris, P.J. West, POLYMERIZATION OF METHYL-METHACRYLATE INITIATED BY ULTRASOUND, *Macromolecules*, 25 (1992) 6447-6454.
- [31] P. Kruus, M. O'Neill, D. Robertson, ULTRASONIC INITIATION OF POLYMERIZATION, *Ultrasonics*, 28 (1990) 304-309.
- [32] G.L.C. Paulus, Q.H. Wang, M.S. Strano, Covalent Electron Transfer Chemistry of Graphene with Diazonium Salts, *Accounts Chem. Res.*, 46 (2013) 160-170.
- [33] W. Lai, D. Xu, X. Wang, Z. Wang, Y. Liu, X. Zhang, Y. Li, X. Liu, Defluorination and covalent grafting of fluorinated graphene with TEMPO in a radical mechanism, *PCCP Phys. Chem. Chem. Phys.*, 19 (2017) 24076-24081.
- [34] P. Attri, Y.H. Kim, D.H. Park, J.H. Park, Y.J. Hong, H.S. Uhm, K.-N. Kim, A. Fridman, E.H. Choi, Generation mechanism of hydroxyl radical species and its lifetime prediction during the plasma-initiated ultraviolet (UV) photolysis, *Scientific Reports*, 5 (2015) 9332.
- [35] X.C. Pan, N. Malhotra, J.N. Zhang, K. Matyjaszewski, Photoinduced Fe-Based Atom Transfer Radical Polymerization in the Absence of Additional Ligands, Reducing Agents, and Radical Initiators, *Macromolecules*, 48 (2015) 6948-6954.
- [36] S. Smolne, S. Weber, M. Buback, Propagation and Termination Kinetics of Poly(Ethylene Glycol) Methyl Ether Methacrylate in Aqueous Solution, *Macromol. Chem. Phys.*, 217 (2016) 2391-2401.
- [37] M. Kubo, T. Kondo, H. Matsui, N. Shibasaki-Kitakawa, T. Yonemoto, Control of molecular weight distribution in synthesis of poly(2-hydroxyethyl methacrylate) using ultrasonic irradiation, *Ultrason. Sonochem.*, 40 (2018) 736-741.
- [38] M. Antonietti, S. Heinz, M. Schmidt, C. Rosenauer, Determination of the Micelle Architecture of Polystyrene/Poly(4-vinylpyridine) Block Copolymers in Dilute Solution, *Macromolecules*, 27 (1994) 3276-3281.

- [39] A.K. Brewer, A.M. Striegel, Characterizing the size, shape, and compactness of a polydisperse prolate ellipsoidal particle via quadruple-detector hydrodynamic chromatography, *Analyst*, 136 (2011) 515-519.
- [40] P. Wiltzius, Hydrodynamic behavior of fractal aggregates, *Phys. Rev. Lett.*, 58 (1987) 710-713.
- [41] M.W. Forney, J.C. Poler, Sonochemical Formation of Methyl Hydroperoxide in Polar Aprotic Solvents and Its Effect on Single-Walled Carbon Nanotube Dispersion Stability, *J. Am. Chem. Soc.*, 132 (2010) 791-797.
- [42] S.M. Lee, Lalhmunsiam, S.I. Choi, D. Tiwari, Manganese and iron oxide immobilized activated carbons precursor to dead biomasses in the remediation of cadmium-contaminated waters, *Environ. Sci. Pollut. Res.*, 20 (2013) 7464-7477.
- [43] H.H. Hammud, A. Shmait, N. Hourani, Removal of Malachite Green from water using hydrothermally carbonized pine needles, *RSC Adv.*, 5 (2015) 7909-7920.
- [44] D.M. Guo, Q.D. An, Z.Y. Xiao, S.R. Zhai, Z. Shi, Polyethylenimine-functionalized cellulose aerogel beads for efficient dynamic removal of chromium(VI) from aqueous solution, *RSC Adv.*, 7 (2017) 54039-54052.
- [45] Y. You, X.H. Jin, X.Y. Wen, V. Sahajwalla, V. Chen, H. Bustamante, R.K. Joshi, Application of graphene oxide membranes for removal of natural organic matter from water, *Carbon*, 129 (2018) 415-419.
- [46] N. Wei, X. Peng, Z. Xu, Understanding Water Permeation in Graphene Oxide Membranes, *ACS Appl. Mater. Interfaces*, 6 (2014) 5877-5883.
- [47] L. Li, J. Zhang, Y. Li, C. Yang, Removal of Cr (VI) with a spiral wound chitosan nanofiber membrane module via dead-end filtration, *J. Membr. Sci.*, 544 (2017) 333-341.
- [48] J.M. Monteagudo, M.J. Ortiz, Removal of inorganic mercury from mine waste water by ion exchange, *Journal of Chemical Technology & Biotechnology*, 75 (2000) 767-772.

### 3.6 Figures and tables

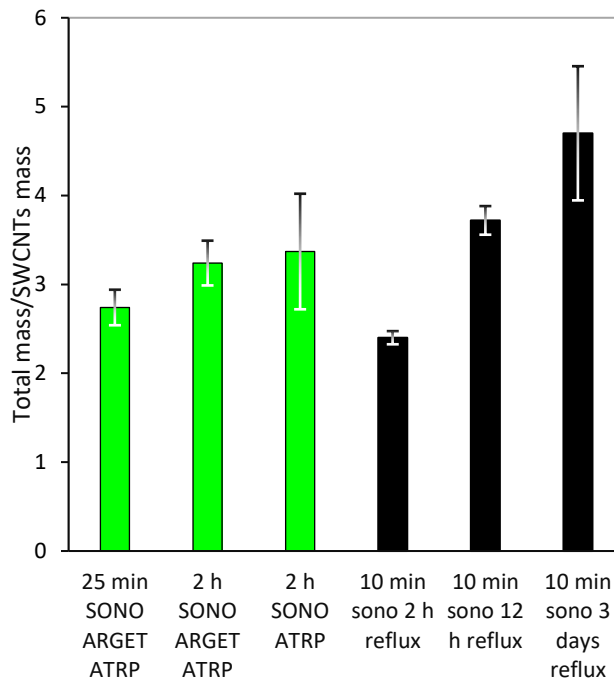


Figure 3.1: Total-mass per SWCNT mass ratio versus functionalization process. Aq-SONO-ARGET ATRP-SNR and Aq-SONO ATRP SNR presented in bars with green shades. Aq-SNR under normal reflux conditions for various functionalization time durations are shown as black bars. Error bars in all data points are due to propagation of differential errors except 2 h Aq-SONO-ATRPSNR  $\pm$  standard error  $n=4$ .

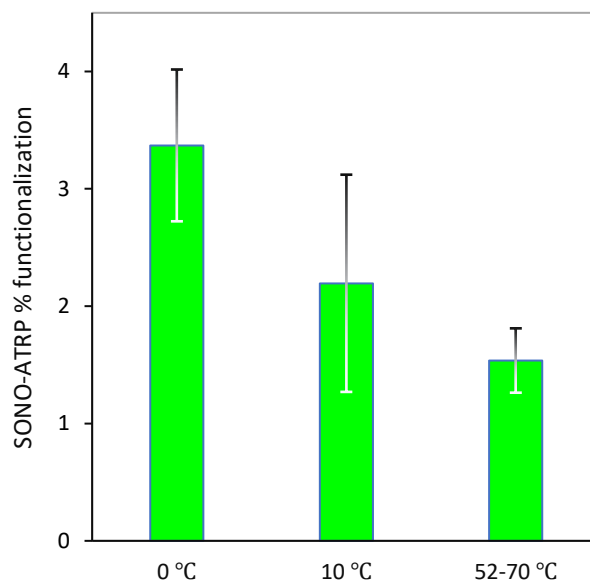


Figure 3.2: SONO-ATRP % functionalization as a function of temperature. Aq-SONO-ATRP-SNR at different temperatures presented in bars. All data points reported as average  $\pm$  standard error, 95% confidence error from 2–4

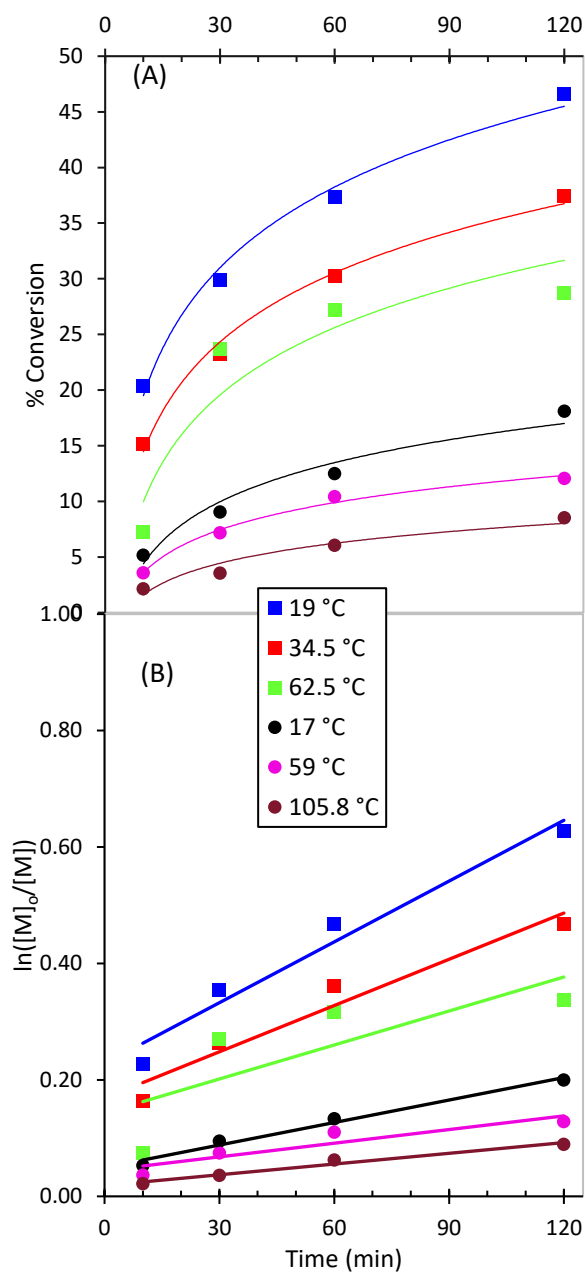


Figure 3.3: Growth kinetics of SONO-ATRP of poly(vbTMAC) as a function of temperature using ultrasonication under conditions  $[\text{vbTMAC}]:[\text{CuBr}_2]:[\text{TPMA}] = 67:0.05:0.25$  in aqueous medium (a) % monomer conversions (b) Semilogarithmic kinetic plots. (■ denotes 81 W cm<sup>2</sup> and ● denotes 36 W cm<sup>2</sup> ultrasonication intensity).

Table 3.1: % monomer conversions of SONO-ATRP-I and SONO-ATRP-P as a function of power intensities under conditions:  $T_{\text{bulk}} = 10$  °C during sonochemistry ( $\Delta t =$  sonication duration).  $T_{\text{bulk}} = \sim 100$  °C during reflux.  $[\text{vbtMAC}]:[\text{CuBr}_2]:[\text{TPMA}] = 1023:0.05:0.5$  in aqueous medium. Catalyst = 5 ppm

<b>Power</b> ( $\text{W cm}^{-2}$ )	<b>SONO-ATRP-I</b> + Reducing - Initiator $\Delta t = 2$ h Total time = 15 h	<b>SONO-ATRP-P</b> - Reducing + Initiator $\Delta t = 5$ h Total time = 6 h
	<b>% conversion</b>	
36	83.3	22.8
90	90.1	36.2
135	93.0	55.0

Table 3.2: D:G ratio of Raman spectra of Pristine SWCNT compared to Aq-SNR synthesized under different conditions. \*All samples are centrifuged at 20,000 g, 20 °C, 1 h and the supernatant is deposited on polypropylene membrane and analyzed.

Controls and NanoResins	D:G
Pristine SWCNT	0.13
Pristine SWCNT and reagents - without monomer	0.13
1 h SONO-Pristine SWCNT	0.19
2 h SONO-Pristine SWCNT	0.20
4 h SONO-Pristine SWCNT	0.22
2 h reflux Aq-SNR*	0.30
12 h reflux Aq-SNR*	0.33
3 days reflux Aq-SNR*	0.33
2h Aq-SONO-ARGET ATRP-SNR*	0.35
2 h Aq-SONO-ATRP-SNR	0.33
2 h Aq-SONO-ATRP-SNR*	0.35
2 h Aq-SONO-ATRP-SS-SNR	0.36

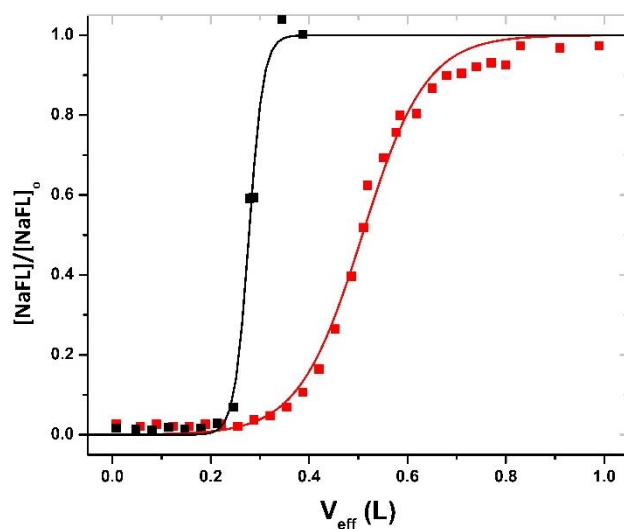


Figure 3.4: Breakthrough curves (ratio of effluent concentration,  $[\text{NaFL}]$  and feed concentration,  $[\text{NaFL}]_0$  as function of effective volume). Non-linear Thomas model was used for fitting. Short brush functionalization to SWCNTs (red) and longer brush functionalization to SWCNTs (black). Both

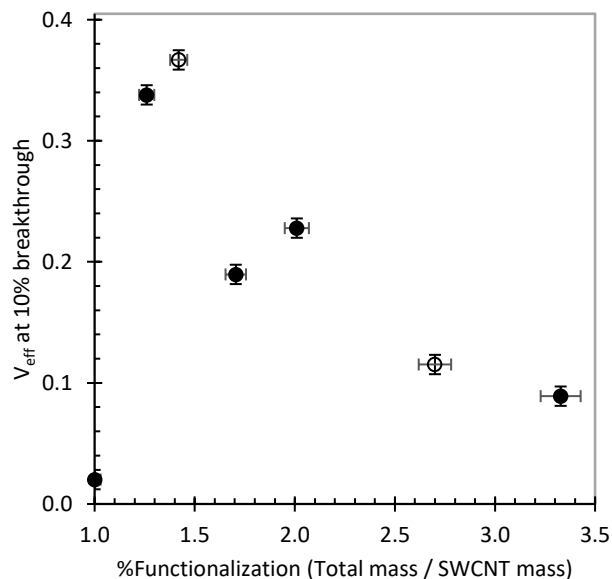


Figure 3.5: Effective volume at 10% breakthrough versus %Functionalization for various NanoResin membranes. Open circles are from one pot short strand NanoResin functionalization. %F = 1 is for pristine SWCNT film.

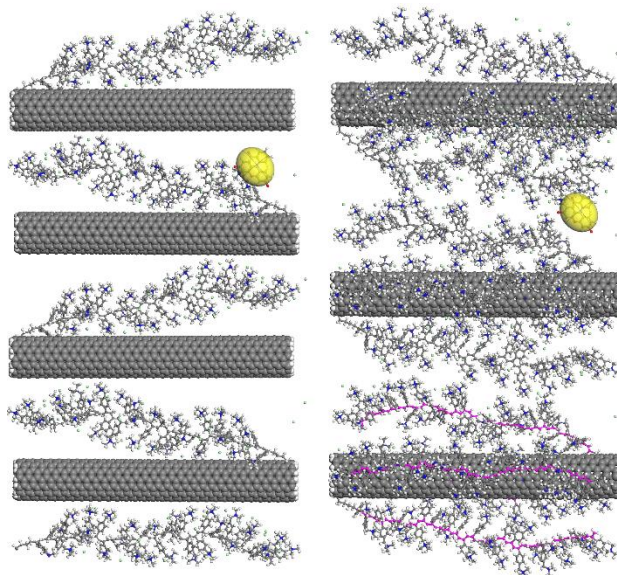


Figure 3.6: Molecular mechanics geometry optimization of Aq-SNR film. %Functionalization = 1.5 (left) and 3.0 (right). Closest contact spheroid of a fluorescein anion is shown (yellow) within the polyelectrolyte brushes.

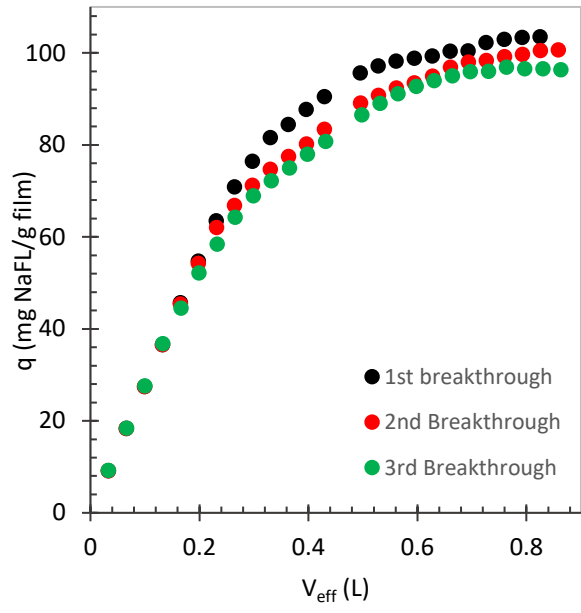


Figure 3.1: NaFL loading onto NanoResin thin film versus effective analyte volume. The material's performance after regeneration is demonstrated for three cycles.



Figure 3.2: NanoResin membrane before any breakthrough experiments (left) and then after the 3<sup>rd</sup> breakthrough experiment (right). Yellow tinge on thin film (right) is from the NaFL adsorption.

### 3.7 Supplementary figures and tables

Table S3.1: Apparent values of propagation rate constants ( $k_{app}$ ) of ARGET ATRP, SONO-ARGET ATRP and SONO-ATRP reactions calculated from slopes of  $\ln(M_0/M)$  vs time at different temperatures.

Polymerization mechanisms	Power Intensities ( $W\ cm^{-2}$ ) and	Bulk temperature of reaction ( $^{\circ}C$ )	Propagation rate constant $k_{app}$ ( $s^{-1}$ )
ARGET ATRP	-	19.5	$3.0 \times 10^{-4}$
		32.0	$5.0 \times 10^{-4}$
		45.0	$5.5 \times 10^{-4}$
		54.0	$7.0 \times 10^{-4}$
		74.0	$1.3 \times 10^{-3}$
		106.2	$2.2 \times 10^{-3}$
SONO-ATRP	18	17.0	$1.3 \times 10^{-3}$
		59.0	$8.0 \times 10^{-4}$
		105.8	$6.0 \times 10^{-4}$
	81	19.0	$3.5 \times 10^{-3}$
		34.5	$2.6 \times 10^{-3}$
		62.5	$1.9 \times 10^{-3}$
SONO-ARGET ATRP	125.2	19.5	$3.2 \times 10^{-3}$
SONO-ATRP	125.2	12.0	$3.5 \times 10^{-3}$
		24.0	$2.8 \times 10^{-3}$

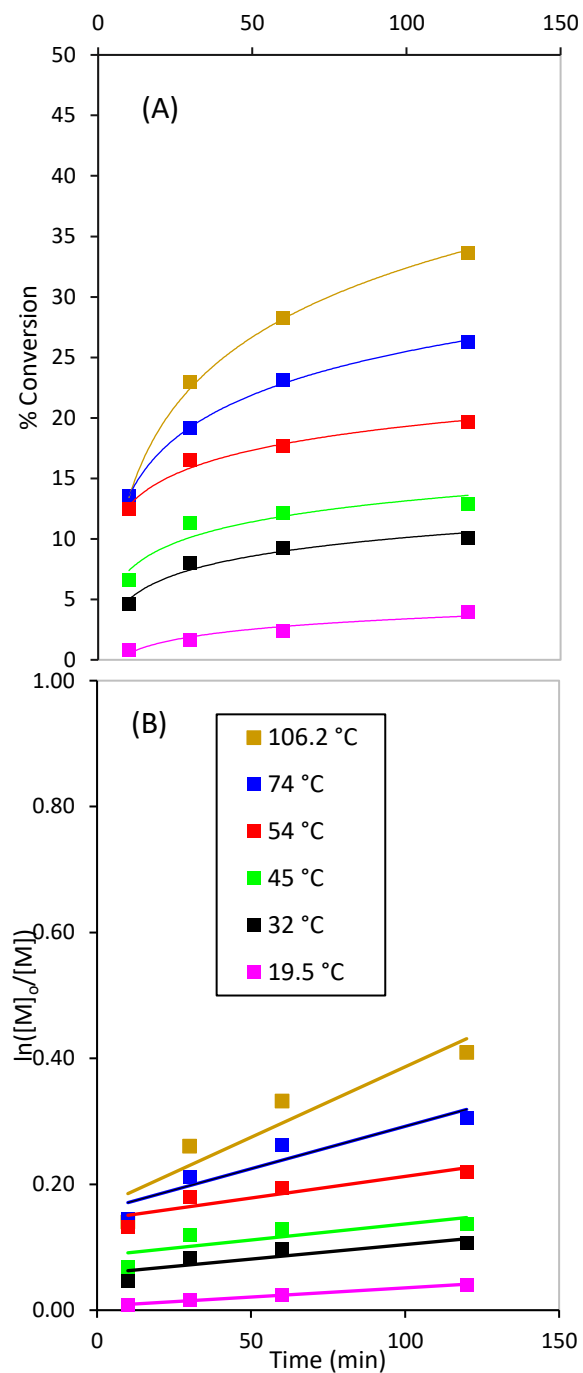


Figure S3.1: Growth kinetics of ARGET-ATRP of poly(vbTMAC) as a function of temperature under conditions  $[\text{vbTMAC}]:[\text{HEBiB}]:[\text{CuBr}_2]:[\text{TPMA}] = 67:1.36:0.05:0.25$  with AA flow rate of  $32 \text{ nmol min}^{-1}$  in aqueous medium (a) % monomer conversions (b) Semilogarithmic kinetic plots.

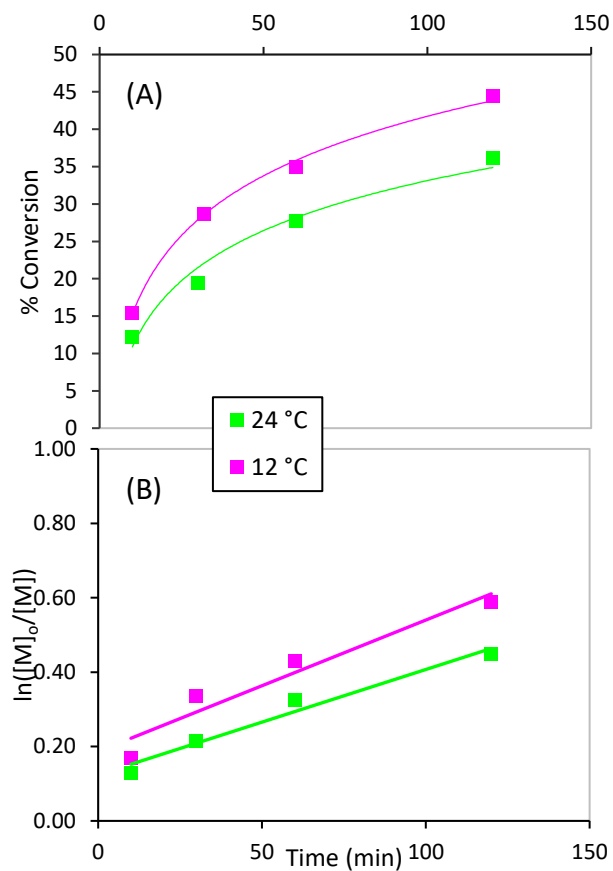


Figure S3.2: Growth kinetics of SONO-ATRP of poly(vbTMAC) as a function of temperature using  $125.2 \text{ W cm}^{-2}$  ultrasonication intensity under conditions  $[\text{vbTMAC}]:[\text{CuBr}_2]:[\text{TPMA}] = 67:0.05:0.25$  in aqueous medium (a) % monomer conversions (b) Semilogarithmic kinetic plots.

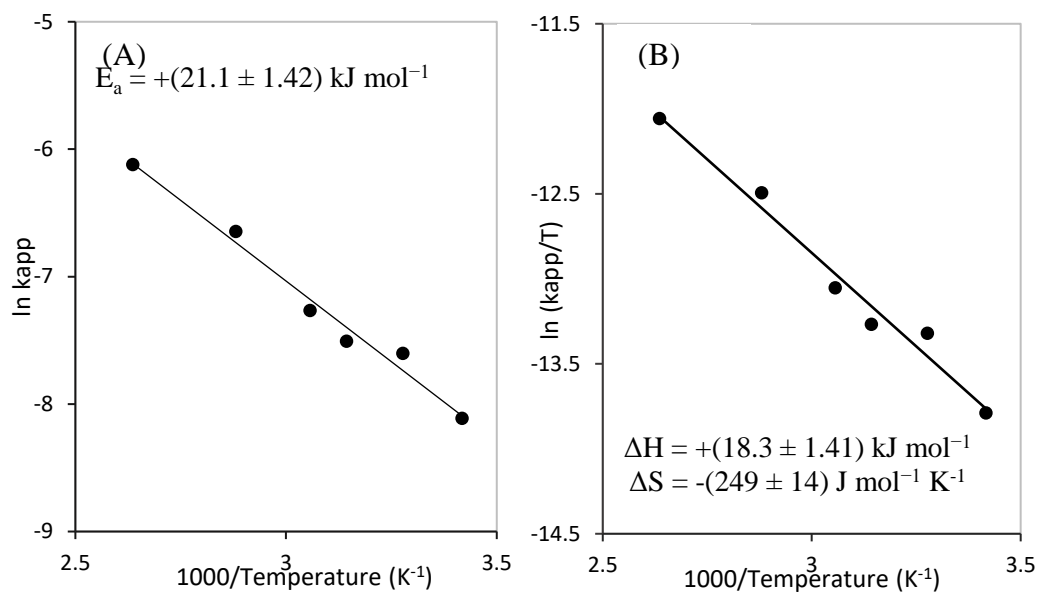


Figure S3.3: (a) Arrhenius and (b) Eyring plots for poly(vbTMAC) using ARGET ATRP in aqueous medium

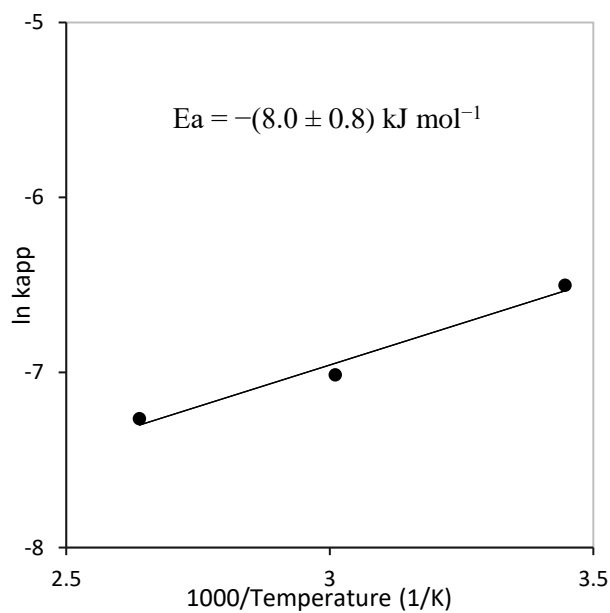


Figure S3.4: Arrhenius plot for poly(vbTMAC) using Aq-SONO-ATRP at  $36 \text{ W cm}^{-2}$  in aqueous medium performed using thin probe sonicator.

Table S3.1: DLS and Zeta potential measurements. Error bars are reported as average  $\pm$  standard error, 95% confidence interval error from 2-4 multiple runs.

	Hydrodynamic diameter (nm)	Zeta potential (mV)	Mobility ( $\mu\text{mcm/Vs}$ )
Aq-SONO-ATRP poly(vbTMAC)	$22.1 \pm 2.6$	-	-
0 °C functionalized Aq-SONO-ATRP-SNR	-	$36.0 \pm 0.94$ mV	$2.817 \pm 0.075$
0 °C functionalized Aq-SONO-ATRP-SNR (after centrifugation)	$261.5 \pm 1.4$	$40.3 \pm 1.2$	$3.157 \pm 0.093$
85 °C functionalized Aq-SONO-ATRP-SNR	-	$46.3 \pm 0.74$	$3.627 \pm 0.057$
85 °C functionalized Aq-SONO-ATRP-SNR (after centrifugation)	$220.6 \pm 1.6$	$55.3 \pm 0.54$	$4.337 \pm 0.044$

**Sample Name:** Aq-SONO-ATRP p(vbTMAC) 3  
**SOP Name:** size SWCNT.sop  
**File Name:** Size SONO-ATRP polymer.dts  
**Record Number:** 18  
**Material RI:** 1.59  
**Material Absorption:** 0.010  
**Dispersant Name:** Water  
**Dispersant RI:** 1.330  
**Viscosity (cP):** 0.8872  
**Measurement Date and Time:** Friday, November 08, 2019 6:49:37

**Temperature (°C):** 25.0  
**Count Rate (kcps):** 75.7  
**Cell Description:** Low volume disposable sizing cuv...  
**Duration Used (s):** 170  
**Measurement Position (mm):** 1.25  
**Attenuator:** 11

	Size (d.nm):	% Number	Width (d.nm):
<b>Z-Average (d.nm):</b> 212.3	<b>Peak 1:</b> 21.48	100.0	6.011
<b>Pdl:</b> 1.000	<b>Peak 2:</b> 0.000	0.0	0.000
<b>Intercept:</b> 0.124	<b>Peak 3:</b> 0.000	0.0	0.000

**Result quality :** Refer to quality report

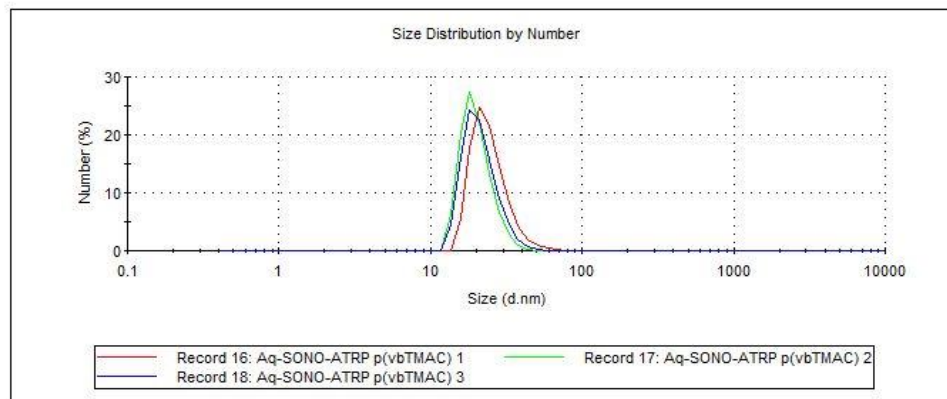


Figure S3.5: Effective hydrodynamic diameter (nm) of poly(vbTMAC) using Aq-SONO-ATRP at  $144 \text{ W cm}^{-2}$  for 4 h resulting in 93% conversion. Multiple runs were measured and averaged. All data shown.

## MALS

### characterization of SONO ARGET-ATRP polymerization

Analysis conditions HPLC/UHPLC	1260 Infinity II (Agilent)
MALS detectors	DAWN multi-angle light scattering detector (Wyatt)
dRI detectors	Optilab differential refractometer (Wyatt)
Columns	Tosoh TSKgel G5000PWxl-CP
Mobile phase	PBS (50 mM Na <sub>2</sub> PO <sub>4</sub> , 50 mM NaCl) at 1 mL/min
Software	ASTRA 7.3 (Wyatt)

### Data

Mw(kg/mol)	Mn(kg/mol)	PDI	rms radius (nm)	Rh(nm)
208.9 ±1.7	143.6 ±0.7	1.5 ±0.0	23.0 ±0.1	10.1 ±0.1

Sample Name: zero degrees functionalized Aq-NanoResin (before centrifugation) 5

SOP Name: zeta SWCNT.sop

File Name: A.dts

Dispersant Name: Water

Record Number: 5

Dispersant RI: 1.330

Date and Time: Tuesday, November 05, 2019 9:10:07 AM

Viscosity (cP): 0.8872

Dispersant Dielectric Constant: 78.5

Temperature (°C): 25.0

Zeta Runs: 14

Count Rate (kcps): 224.5

Measurement Position (mm): 2.00

Cell Description: Clear disposable zeta cell

Attenuator: 10

	Mean (mV)	Area (%)	Width (mV)
Zeta Potential (mV): 35.7	Peak 1: 35.7	100.0	6.48
Zeta Deviation (mV): 6.48	Peak 2: 0.00	0.0	0.00
Conductivity (mS/cm): 0.0329	Peak 3: 0.00	0.0	0.00

Result quality : Good

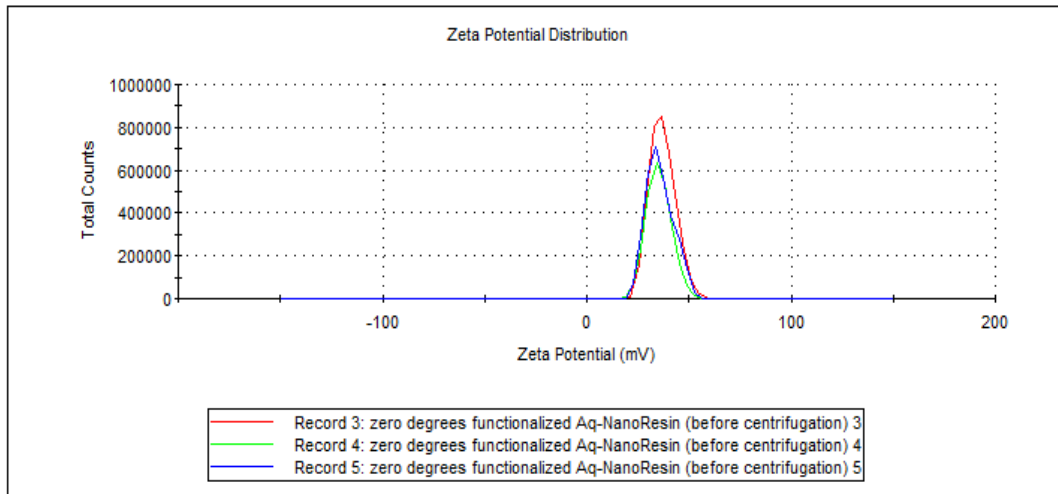


Figure S3.6: Zeta potential of 0 °C functionalized Aq-SONO-ATRP-SNR with total mass per SWCNT-mass ratio of 3.04. Multiple runs were measured and averaged. All data shown.

**Sample Name:** zero degrees functionalized Aq-NanoResin (after centrifugation) 10  
**SOP Name:** zeta SWCNT.sop  
**File Name:** A.dts **Dispersant Name:** Water  
**Record Number:** 50 **Dispersant RI:** 1.330  
**Date and Time:** Tuesday, November 05, 2019 9:57:47 AM **Viscosity (cP):** 0.8872  
**Dispersant Dielectric Constant:** 78.5

**Temperature (°C):** 25.0 **Zeta Runs:** 12  
**Count Rate (kcps):** 46.9 **Measurement Position (mm):** 2.00  
**Cell Description:** Clear disposable zeta cell **Attenuator:** 10

	Mean (mV)	Area (%)	Width (mV)
<b>Zeta Potential (mV):</b> 41.2	Peak 1: 41.2	100.0	5.92
<b>Zeta Deviation (mV):</b> 5.92	Peak 2: 0.00	0.0	0.00
<b>Conductivity (mS/cm):</b> 0.0230	Peak 3: 0.00	0.0	0.00

**Result quality :** Good

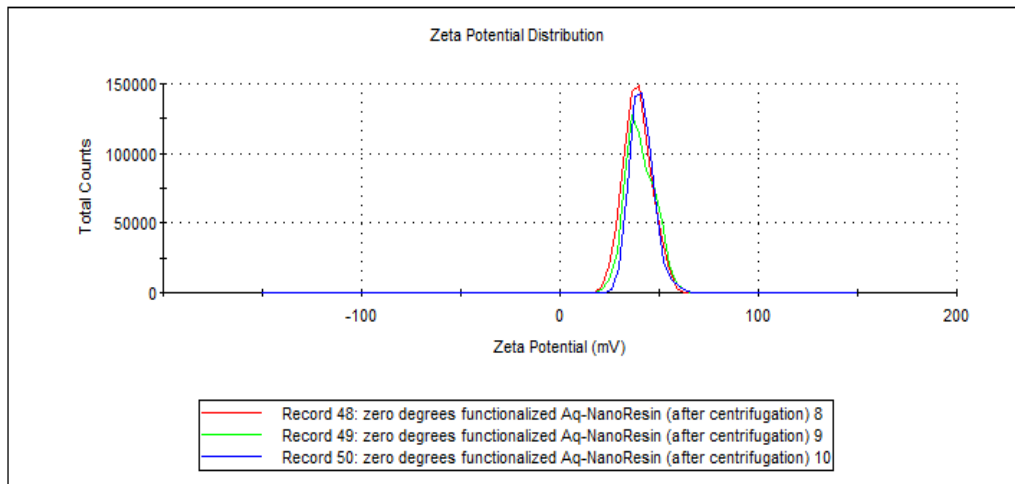


Figure S3.7: Zeta potential of stable dispersion from supernatant of 0 °C functionalized Aq-SONO-ATRP-SNR centrifuged at 20,000 g. Multiple runs were measured and averaged. All data shown.

**Sample Name:** eighty five degrees functionalized Aq-NanoResin (before centrifugation) 7  
**SOP Name:** zeta SWCNT.sop  
**File Name:** A.dts **Dispersant Name:** Water  
**Record Number:** 27 **Dispersant RI:** 1.330  
**Date and Time:** Tuesday, November 05, 2019 9:34:34 AM **Viscosity (cP):** 0.8872  
**Dispersant Dielectric Constant:** 78.5

**Temperature (°C):** 25.0 **Zeta Runs:** 12  
**Count Rate (kcps):** 331.5 **Measurement Position (mm):** 2.00  
**Cell Description:** Clear disposable zeta cell **Attenuator:** 10

	Mean (mV)	Area (%)	Width (mV)
<b>Zeta Potential (mV):</b> 46.3	<b>Peak 1:</b> 46.3	100.0	6.22
<b>Zeta Deviation (mV):</b> 6.22	<b>Peak 2:</b> 0.00	0.0	0.00
<b>Conductivity (mS/cm):</b> 0.00437	<b>Peak 3:</b> 0.00	0.0	0.00

**Result quality :** Good

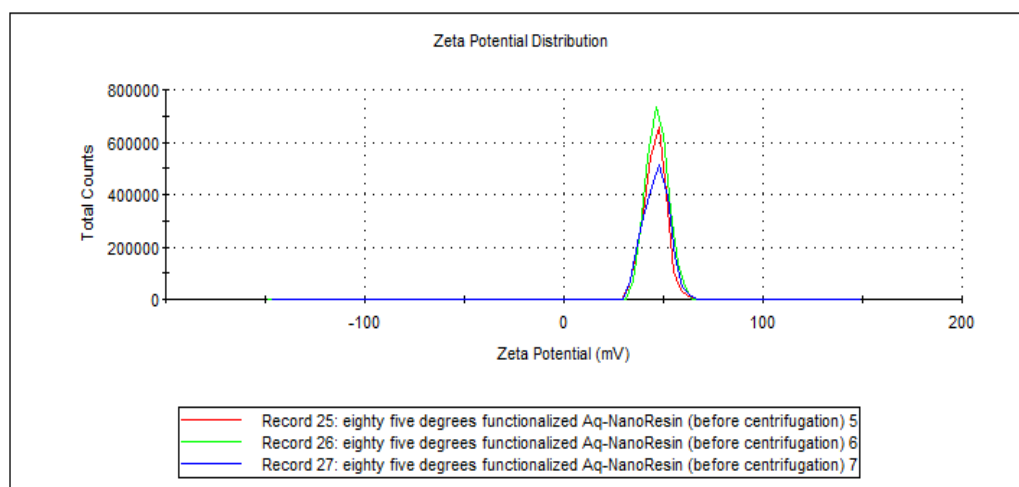


Figure S3.8: Zeta potential of 85 °C functionalized Aq-SONO-ATRP-SNR with total mass per SWCNT-mass ratio of 1.74. Multiple runs were measured and averaged. All data shown.

**Sample Name:** eighty five degrees functionalized Aq-NanoResin (after centrifugation) 10  
**SOP Name:** zeta SWCNT.sop  
**File Name:** A.dts **Dispersant Name:** Water  
**Record Number:** 60 **Dispersant RI:** 1.330  
**Date and Time:** Tuesday, November 05, 2019 10:10:19 AM **Viscosity (cP):** 0.8872  
**Dispersant Dielectric Constant:** 78.5

**Temperature (°C):** 25.1 **Zeta Runs:** 12  
**Count Rate (kcps):** 141.3 **Measurement Position (mm):** 2.00  
**Cell Description:** Clear disposable zeta cell **Attenuator:** 11

	Mean (mV)	Area (%)	Width (mV)
<b>Zeta Potential (mV):</b> 55.5	<b>Peak 1:</b> 55.5	100.0	7.59
<b>Zeta Deviation (mV):</b> 7.59	<b>Peak 2:</b> 0.00	0.0	0.00
<b>Conductivity (mS/cm):</b> 0.00552	<b>Peak 3:</b> 0.00	0.0	0.00

**Result quality :** Good

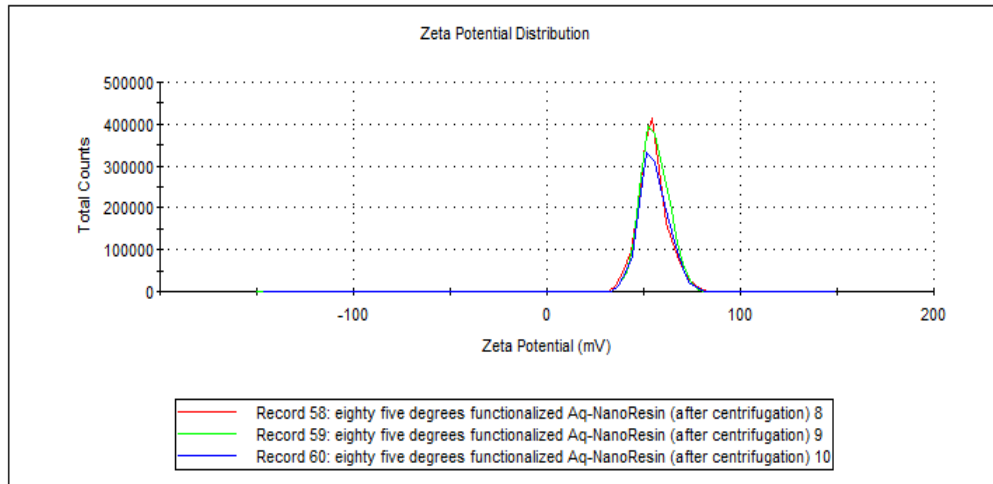


Figure S3.9: Zeta potential of stable dispersion from supernatant of 85 °C functionalized Aq-SONO-ATRP-SNR centrifuged at 20,000 g. Multiple runs were measured and averaged. All data shown.

**Sample Name:** 0 degree Aq-SONO-ATRP-SNR 9  
**SOP Name:** size SWCNT.sop  
**File Name:** size SWCNT trial 3.dts  
**Record Number:** 96  
**Material RI:** 1.59  
**Material Absorbtion:** 0.010  
**Dispersant Name:** Water  
**Dispersant RI:** 1.330  
**Viscosity (cP):** 0.8872  
**Measurement Date and Time:** Thursday, November 07, 201

**Temperature (°C):** 25.1  
**Count Rate (kcps):** 55.7  
**Cell Description:** Low volume disposable sizing cuv...  
**Duration Used (s):** 160  
**Measurement Position (mm):** 4.65  
**Attenuator:** 11

	Size (d.nm):	% Number	Width (d.nm):
<b>Z-Average (d.nm):</b> 449.6	<b>Peak 1:</b> 263.5	100.0	49.65
<b>Pdl:</b> 0.441	<b>Peak 2:</b> 0.000	0.0	0.000
<b>Intercept:</b> 0.509	<b>Peak 3:</b> 0.000	0.0	0.000

**Result quality :** Refer to quality report

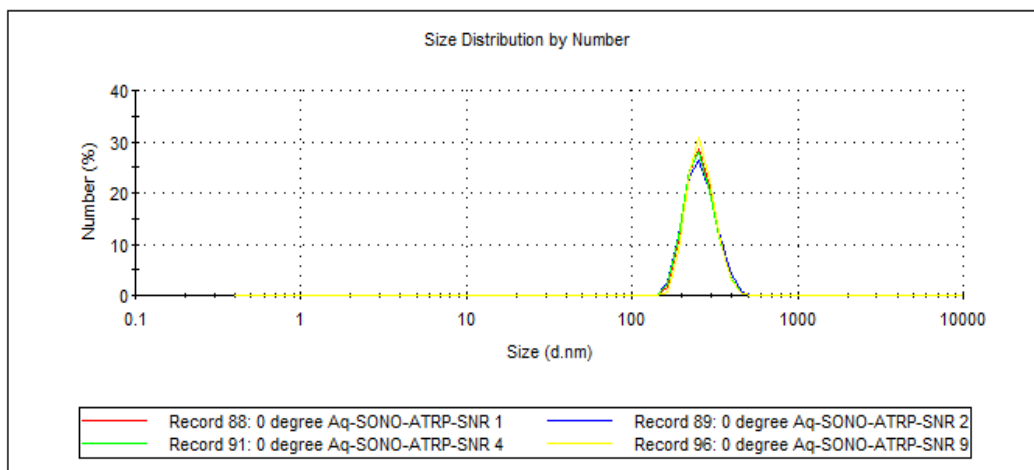


Figure S3.10: Effective hydrodynamic diameter (nm) of stable dispersion from supernatant of 0 °C functionalized Aq-SONO-ATRP-SNR centrifuged at 20,000 g. Multiple runs were measured and averaged. All data shown.

**Sample Name:** 85 degrees Aq-SONO-ATRP-SNR 20  
**SOP Name:** size SWCNT.sop  
**File Name:** size SWCNT trial 3.dts  
**Record Number:** 67  
**Material RI:** 1.59  
**Material Absorbtion:** 0.010  
**Dispersant Name:** Water  
**Dispersant RI:** 1.330  
**Viscosity (cP):** 0.8872  
**Measurement Date and Time:** Wednesday, November 06, 2

**Temperature (°C):** 25.0  
**Count Rate (kcps):** 37.3  
**Cell Description:** Low volume disposable sizing cuv...  
**Duration Used (s):** 170  
**Measurement Position (mm):** 4.65  
**Attenuator:** 11

	Size (d.nm):	% Number	Width (d.nm):
<b>Z-Average (d.nm):</b> 661.8	<b>Peak 1:</b> 221.5	100.0	36.43
<b>Pdl:</b> 0.573	<b>Peak 2:</b> 0.000	0.0	0.000
<b>Intercept:</b> 0.527	<b>Peak 3:</b> 0.000	0.0	0.000

**Result quality :** Refer to quality report

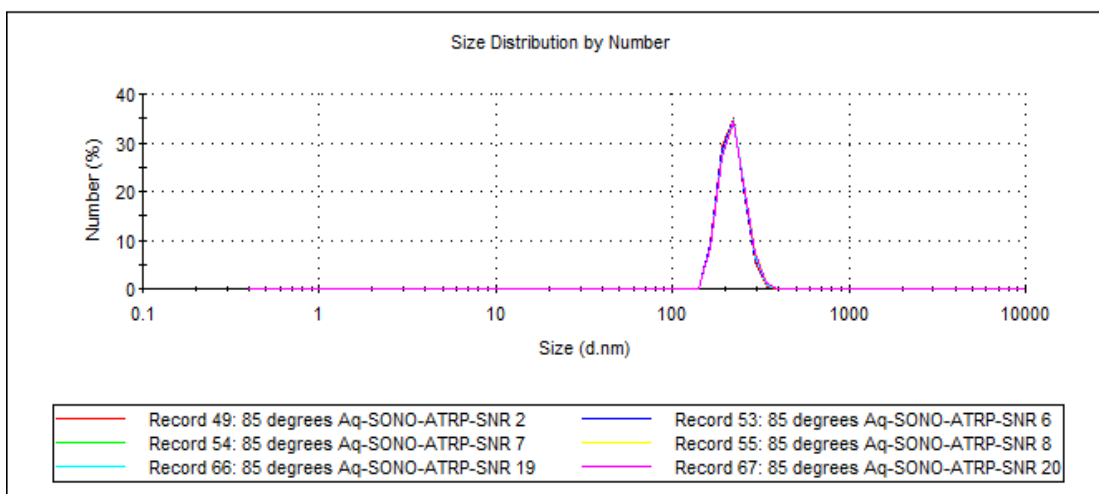


Figure S3.11: Effective hydrodynamic diameter (nm) of stable dispersion from supernatant of 85 °C functionalized Aq-SONO-ATRP-SNR centrifuged at 20,000 g. Multiple runs were measured and averaged. All data shown.

Table S3.2. Membrane kinetic parameters analyzed for adsorption of 0.86 mg-C L<sup>-1</sup> NaFL onto 3 mg of NanoResin thin film. Non-linear Thomas model was used for prediction of kinetic parameters.

NanoResin	[NaFL] <sub>o</sub> (mg-C L <sup>-1</sup> )	Flow rate (mL min <sup>-1</sup> )	k <sub>T</sub> (L min <sup>-1</sup> mg <sup>-1</sup> )	q <sub>e,cal</sub> (mg g <sup>-1</sup> )	q <sub>e,exp</sub> (mg g <sup>-1</sup> )	R <sup>2</sup>	χ <sup>2</sup>
Aq-SNR	0.819	3.87	0.0701 ± 0.00586	60.5 ± 1.67	59.5	0.977	0.0028
25 min SONO- ARGET ATRP	0.816	3.96	0.0951 ± 0.00708	61.1 ± 1.16	59.7	0.988	0.0018
2 h SONO- ARGET ATRP	0.816	3.96	0.335 ± 0.0500	75.4 ± 0.430	72.5	0.99	0.0014
2 h SONO- ATRP	0.855	5.21	0.135 ± 0.0154	48.0 ± 1.62	47.8	0.974	0.0036
2 h SONO- ATRP-SS	0.821	3.84	0.0723 ± 0.00372	139 ± 1	138.	0.992	0.0012

The non-linear form of Thomas Model<sup>67-69</sup> which can be expressed as:

$$\frac{[NaFL]}{[NaFL]_o} = \frac{1}{1 + e^{\frac{k_T}{Q}[q_e M - [NaFL]_o V_{eff}]}}$$

was used to measure the kinetic parameters of the breakthrough curves of Aq-SNR membranes where [NaFL] (mg-C L<sup>-1</sup>) is concentration of adsorbate in the effluent, [NaFL]<sub>o</sub> (mg-C L<sup>-1</sup>) is the initial concentration of adsorbate in the feed solution, k<sub>T</sub> (L mg<sup>-1</sup> min<sup>-1</sup>) is Thomas rate constant, q<sub>e</sub> (mg g<sup>-1</sup>) is continuous flow or equilibrium adsorption capacity, Q (mL min<sup>-1</sup>) is volumetric flow rate, M is mass of adsorbent (g), t is

time (min) and  $V_{\text{eff}}$  (L) is throughput volume. 2 h functionalized Aq-SONO-ARGET ATRP-SNR has higher  $q_e$  value compared to 25 min functionalized Aq-SONO-ARGET ATRP-SNR due to higher total-mass per SWCNT-mass at same flow rate. 25 min functionalized Aq-SONO-ARGET-ATRP-SNR has an earlier breakthrough (89 mL) compared to 2 h-Aq-SONO ARGET-ATRP-SNR (246 mL) withstanding higher flow rate, which explains the importance of higher functionalization of SWCNT in imparting good mechanical strength and high adsorption capacity (as shown in Figure ). 2 h functionalized Aq-SONO-ATRP-SS-SNR demonstrates highest adsorption capacity ( $139 \pm 1 \text{ mg g}^{-1}$ ). We have not optimized the length and content of polyelectrolyte

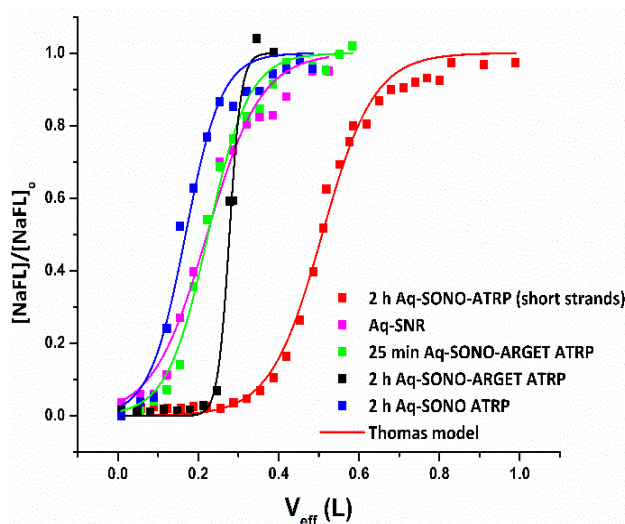


Figure S3.12: Breakthrough curves (ratio of outlet NaFL concentration,  $[\text{NaFL}]$  and feed concentration,  $[\text{NaFL}]_0$  as function of effective volume) for NaFL adsorption by Aq-SNR of different mechanisms and durations of functionalization. NaFL concentration:  $0.816 - 0.855 \text{ mg-C L}^{-1}$ , temperature  $20 \text{ }^\circ\text{C}$ , flow rate:  $3.84\text{-}5.21 \text{ mL min}^{-1}$ . Non-linear Thomas model was used for fitting.

functionalization to achieve best breakthrough curves yet. 2 h functionalized Aq-SONO-ATRP-SS-SNR holds maximum resistance compared to other Aq-SNR due to higher SWCNTs content.

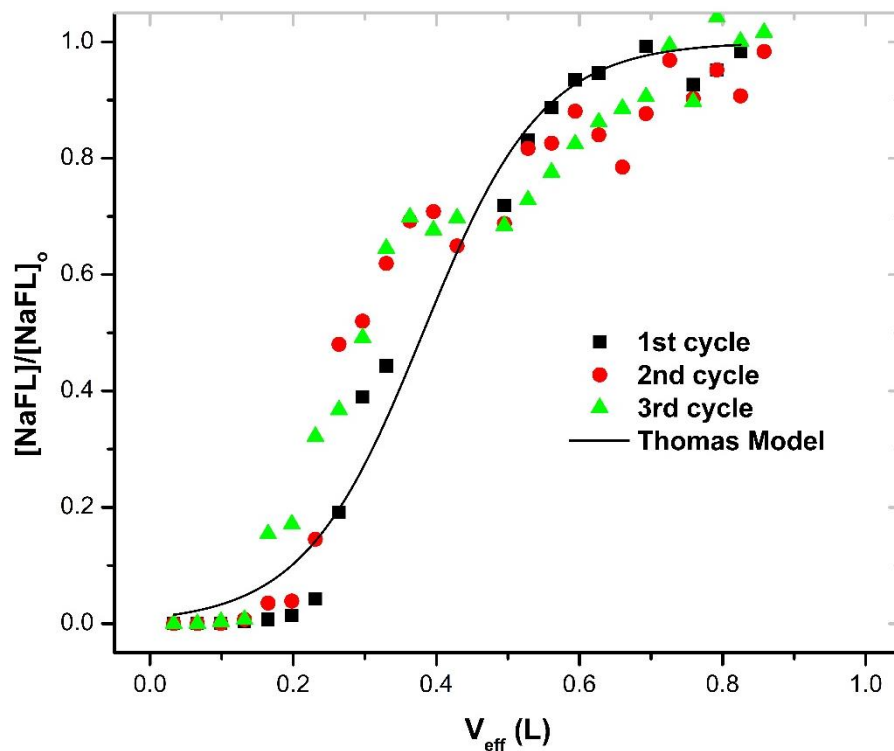


Figure S3.13: Breakthrough curves (ratio of outlet NaFL concentration,  $[\text{NaFL}]$  and feed concentration,  $[\text{NaFL}]_0$  as function of effective volume) for NaFL adsorption by 2 h functionalized Aq-SONO-ATRP-SNR (two pot, 30-mer) NanoResin. NaFL concentration:  $0.831 \text{ mg-C L}^{-1}$ , temperature  $20 \text{ }^\circ\text{C}$ , flow rate:  $14 \text{ mL min}^{-1}$ . Non-linear Thomas model was used for fitting the first breakthrough curve only.

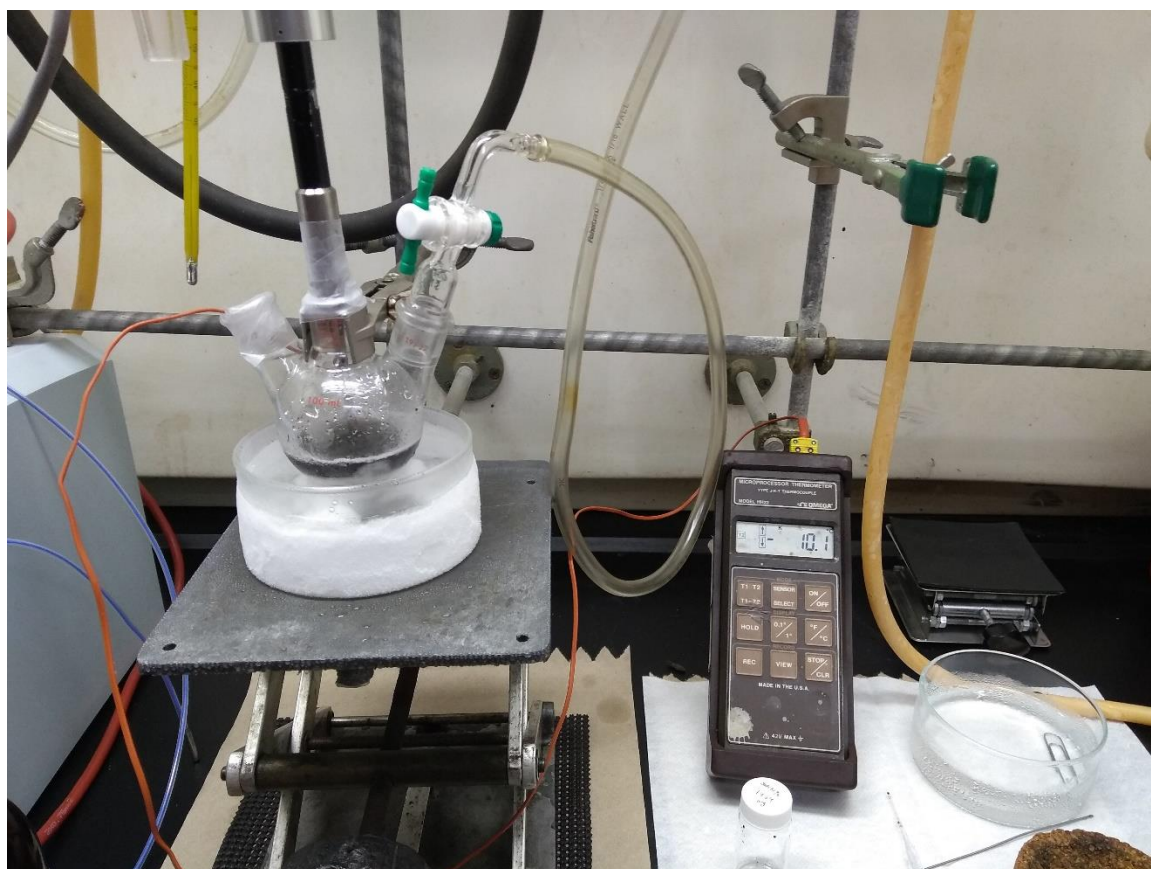
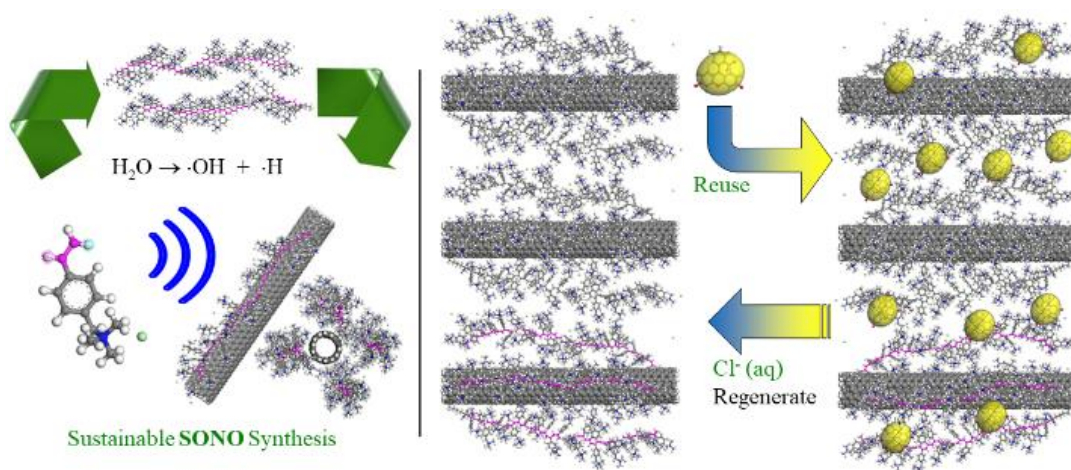


Figure S3.14: Schlenk apparatus with sonicator probe sealed and vessel under Ar(g) positive pressure

References for Supplementary work:

1. Sahu, A.; Blackburn, K.; Durkin, K.; Eldred, T. B.; Johnson, B. R.; Sheikh, R.; Amburgey, J. E.; Poler, J. C. Green synthesis of nanoscale anion exchange resin for sustainable water purification. *Environ. Sci.-Wat. Res. Technol.* **2018**, 4 (10), 1685-1694 DOI: 10.1039/c8ew00593a.
2. Bachilo, S. M.; Strano, M. S.; Kittrell, C.; Hauge, R. H.; Smalley, R. E.; Weisman, R. B. Structure-assigned optical spectra of single-walled carbon nanotubes. *Science* **2002**, 298 (5602), 2361-2366 DOI: 10.1126/science.1078727.
3. Lee, S. M.; Lalmunsiam; Choi, S. I.; Tiwari, D. Manganese and iron oxide immobilized activated carbons precursor to dead biomasses in the remediation of cadmium-contaminated waters. *Environ. Sci. Pollut. Res.* **2013**, 20 (10), 7464-7477 DOI: 10.1007/s11356-013-1609-x.
4. Hammud, H. H.; Shmait, A.; Hourani, N. Removal of Malachite Green from water using hydrothermally carbonized pine needles. *RSC Adv.* **2015**, 5 (11), 7909-7920 DOI: 10.1039/c4ra15505j.
5. Guo, D. M.; An, Q. D.; Xiao, Z. Y.; Zhai, S. R.; Shi, Z. Polyethylenimine-functionalized cellulose aerogel beads for efficient dynamic removal of chromium(VI) from aqueous solution. *RSC Adv.* **2017**, 7 (85), 54039-54052 DOI: 10.1039/c7ra09940a.

# TABLE OF CONTENTS



## CHAPTER 4

### AQUEOUS DEFLUORINATION AND COVALENT GRAFTING OF FLUOROGRAPHITE WITH ANION EXCHANGE RESINS FOR WATER PURIFICATION

Abhispa Sahu, Jeffry Alston, Clifford Carlin, Matt Craps, Klint Davis, Haley Harrison,  
Terawit Kongruengkit, Rachel Rollins, Jordan C. Poler

Keywords: fluorographite, defluorination, functionalization, aqueous, polyelectrolyte,  
emerging contaminants, water purification

## Abstract

Defluorination of fluorographite is a complex procedure involving nucleophilic agents or reactive radicals in caustic or toxic reaction conditions. We have developed a novel green synthetic technique to defluorinate and covalently graft fluorographite surface with living end of quaternary ammonium polyelectrolyte chains under mild reaction conditions in water. This surface derivatization is achieved by the interaction of radical centers on fluorographite surface with incoming electron rich living ends of short strands of anion exchange resins and does not require any external reactive agents. Selected area electron diffraction pattern revealed onion like rings due to evolution of  $sp^2$  hybridized hexagonal patterns of graphitic structure from  $sp^3$  hybridized fluorographite. Transmission electron microscopy revealed few layered graphitic structures with clear domains of functionalization of globular polymer brushes. Water dispersible polyelectrolyte functionalized fluorographite (PFG) formulations have potential applications in water purification against emerging contaminants at environmentally relevant concentrations. Physiochemical properties, kinetics, adsorption isotherm, water flux and morphology of thin film assemblies of PFG resins have been discussed in detail. The developed methodology is a facile approach towards high performance 2D materials for sustainable applications.

## Introduction

Graphene based materials have been explored for use in drinking water purification technologies. This is mostly due to their exceptional mechanical<sup>1</sup> and chemical stability, large specific surface area and their assembly into nanoscale multi-layer laminate thin films. Membrane purification technology requires the optimization of high water flux and efficient impurity removal. In general graphene does not possess an intrinsic strong binding mechanism to water soluble impurities. Moreover, most graphene based membranes have very low water flux and are thus not commercially viable. To improve these properties, graphene exfoliation and chemical modification has received significant study. The modification and surface functionalization of graphite or graphene typically starts with a chemically caustic process. Hummers and Offeman's oxidation of graphene to form graphene oxide (GO) uses strong oxidizing environments.<sup>2</sup> Furst et al. demonstrated chemical reduction of GO by hydrazine or hydrazine hydrate.<sup>3</sup> Most of these chemical methods require compounds that are harmful to human health and to the environment. Consistent with the principles of green chemistry, materials synthesis and processing should avoid caustic reagents and non-aqueous solvents. Thus, alternative graphene derivatives are required to allow easy green processability and achieve highly functionalized nanoscale materials, capable of removing known and emerging contaminants to very low levels in water.

Fluorographene as emerged as a graphene derivative that is widely used in various applications like corrosion resistant coatings,<sup>4</sup> thermoelectric devices,<sup>5</sup> supercapacitors,<sup>6</sup> biosensing,<sup>7</sup> solar cells,<sup>8</sup> organic field effect transistors.<sup>9,10</sup> Although the C-F bonds have high chemical stability, due to low lying  $\sigma^*$  orbital of tertiary C-F bond they do react as

an electrophiles.<sup>11,12</sup> Studies have shown that the defluorination of fluorographene follows an  $S_N2$  nucleophilic substitution mechanism. Additionally, the generation of spin centers/radical centers (fluorine vacancies) due to radical addition mechanisms from the solvent or from the presence of electron rich species, has been shown to facilitate defluorination.<sup>11,13-15</sup> Medved et al. proposed that the defects in fluorographene contributes to its higher reactivity relative to other, more stable, perfluorocarbons. It was postulated that point defects initiate a radical mechanism that cause defluorination in presence of methyl radicals in an N,N-dimethylformamide environment.<sup>11</sup> Lai et al. defluorinated fluorographene by heating in presence of 2,2,6,6-tetramethylpiperidine-1-oxyl (TEMPO) radical and demonstrated the reduction of atomic percent (At%) of F from 44.69% in pristine FG to 16.28 At% after defluorination.<sup>13</sup> Koulompis et al. demonstrated defluorination of fluorographene under highly basic conditions (pH = 10-11) postulating  $S_N2$  nucleophilic substitution of F atom by hydroxyl moieties.<sup>15</sup> Rajeena et al. performed a similar F substitution reaction in fluorographite using 2.5 M NaOH in ethanol that exfoliated into hydroxy substituted graphene, which was converted into graphene in hydrazine hydrate solution.<sup>16</sup>

We have achieved defluorination of fluorographite using an all-aqueous environment in presence of short strands of polyelectrolyte of vinylbenzyl trimethylammonium chloride (vbTMAC) with a living radical chain end at neutral pH. We have achieved defluorination to below 15 At% using this green and sustainable method. Radical centers on fluorographite can interact with electron rich or electron donating species. Delocalization of spin centers, due to the presence of C-F  $\sigma^*$  orbitals in the neighboring atoms, can stabilize these Singly Occupied Molecular Orbitals

(SOMO).<sup>11</sup> These defects can act as the initiation sites of defluorination which eventually increase upon reaction with electron rich species. Baumgartner et al. postulated that the byproduct of defluorinated fluorobenzene, <sup>under</sup> aqueous conditions, is the fluoride anion.<sup>17</sup> Hence, the defluorinated carbon will carry slightly positive charge due to highly electronegative fluorine atoms bound to neighboring carbon atoms. These sites are potential centers for polyelectrolyte radical attack and subsequent covalent attachment. The number of spin centers increase during the reaction, resulting in a well functionalized PFG resin material. It has been demonstrated in previous research works that the defluorination and delocalization of spin centers gave rise to cascade of C=C bonds (or  $\pi$  conjugated regions) in fluorographite.<sup>11,13</sup> We have observed similar behavior as discussed in the results section below.

Per- and polyfluoroalkyl substances (PFAS) have notoriously high thermal and chemical stability, making them resistant to environmental degradation. Therefore, these persistent and toxic impurities are pervasive throughout natural water systems. Recent studies have shown presence of PFAS in human blood serum, breastmilk,<sup>18</sup> human urine,<sup>19</sup> human embryonic fetal organs,<sup>20</sup> etc. and are emerging threats to the environment and to human health due to lack of regulation. The maximum concentration level (MCL) of PFAS set by the US EPA is  $70 \text{ ng L}^{-1}$ . Diatrizoic acid (DTZA) is one of the iodinated X-ray contrast media (ICM) that are used for medical imaging. ICM are found in natural water resources in the range of  $100 \text{ } \mu\text{g L}^{-1}$  and conventional wastewater treatment systems are not effective in removing them.<sup>21</sup> Oxyanions of As, W, V, Cr and other species are commonly found emerging metal contaminants in wastewater streams. Metalloid oxyanions are non-biodegradable, highly water soluble and extremely mobile

species that are also deleterious to human health and the environment.<sup>22,23</sup> All these contaminants have been specifically mentioned by US EPA as contaminants of emerging concern. Our PFG materials have been designed from the perspective of removal of these and many other contaminants. Our materials can perform efficient, and high capacity removal of contaminants with less contact time and high water flux. Pérez et al. formulated hybrid sorbent of aluminum oxyhydroxide and poly(vbTMAC) and tested removal of As. However, the  $K_f$  values of these hybrid materials calculated from Freundlich isotherms were extremely low ( $0.012\text{-}0.90\text{ mg g}^{-1}$ ) which confirms weak binding.<sup>24</sup> Our materials have stronger binding ( $K_f = 14.4 \pm 0.8\text{ (mg/g)(L/mg)}$ ) and the dynamics of achieving pseudoequilibrium is rapid. We achieved  $\geq 90\%$  removal of all tested contaminants, and these PFG resins are easily regeneratable and readily reusable without any significant performance degradation. Hence, PFG resins provide an efficient platform for tailoring graphene derivatives with a high degree of functionalization toward sustainable industrial applications.

## 4.2 Materials

### 4.2.1 Chemicals and Materials

All reagents were used as purchased without additional purification or modification. Graphite, fluorinated, polymer (Fluorographite,  $> 61\text{ wt \% F}$ ) (Aldrich, Lot #MKCJ1629) was used. Polymer synthesis and functionalization chemicals: vinylbenzyl trimethylammonium chloride (vbTMAC) (Fisher, 97%; Lot #A0311318) monomer, copper(II) bromide (Acros, 99+%; Lot #A0344238), tris(2-pyridylmethyl)amine (TPMA) (TCI,  $>98.0\%$ ; Lot #Z8GMO-AD) for the catalyst, stannous octoate (SnOct) (Sigma-

Aldrich, 92.5–100%, Lot #SLBP5072V) for the reducing agent, 2-hydroxyethyl 2-bromo-isobutyrate (HEBiB) (Sigma-Aldrich, 95%, Lot #MKBW2607) as the initiator. 2,2,6,6-tetramethylpiperidine-1-oxyl (TEMPO) (Sigma Aldrich, Lot # BCBZ3312) is the external radical. Other analytes include sodium chloride (Mallinckrodt Chemical, Lot #E42589), and disodium fluorescein (NaFL) (Sigma, Lot #BCBR1213V). Contaminants include perfluorooctanoic acid (PFOA) (Aldrich, Lot #MKCC6736), Potassium perfluorooctanesulfonate, 98% (PFOS) (Matrix Scientific, Lot #M22Q), Diatrizoic acid (DTZA) (Alfa Aesar, Lot #W24F030). Contaminants in the form of metalloids oxyanions of interest include Potassium Chromate ( $\text{CrO}_4^{2-}$ ) (Alfa Aesar, Lot #9186184), sodium orthovanadate ( $\text{VO}_4^{3-}$ ) (Alfa Aesar, Lot #Q21G501), Arsenic trioxide/sodium hydroxide ( $\text{AsO}_3^{3-}/\text{OH}^{1-}$ ) (Spectrum, Lot # 2JH0192), Ammonium Tungstate ( $\text{WO}_4^{2-}$ ) (Alfa Aesar, Lot #227051), Arsenic (V) oxide hydrate ( $\text{H}_2\text{AsO}_4^{1-} / \text{HAsO}_4^{2-}$ ) (SPEX CertiPrep, Lot #25-72AS5M). Poly(ethylene glycol) methyl ether (Sigma Aldrich, Lot #B2BR0088V).

#### 4.2.2 Workup and purification

Workup and purification of the synthesis required: polypropylene membrane filters (0.45  $\mu\text{m}$  pore size, 47 mm wide, Lot #2075-5), nitrocellulose mixed ester (MCE) (Advantec, Lot. # 70419200) with 0.2  $\mu\text{m}$  pore diameter and 13 mm width and (Advantec, Lot. #61202200) with 0.2  $\mu\text{m}$  pore diameter and 25 mm width, 2 kDa MWCO dialysis membrane (Spectrum Labs, Lot. #3294218) 45 mm flat width and 29 mm diameter, 15 ml polypropylene centrifuge tubes (Corning®, Lot.# 430052) and 50 kDa MWCO dialysis membrane (Spectrum Labs, Lot. #3292110) 34 mm flat width and

22 mm diameter. Membranes were activated by incubating for 10 min in Milli-Q water under constant stirring. Microcon® Centrifugal Filters (YM-100 lot# R1CN67003).

#### 4.3 Method.

##### 4.3.1 Synthetic methods.

##### 4.3.1.1 Aqueous synthesis of polyelectrolyte functionalized fluorographite in presence of external radical, catalyst complex and reducing agent using sonochemistry and reflux (PFG-I)

PFG-I was synthesized in one-step process. Polyelectrolyte of vbTMAC (Fisher, 97%; Lot #A0311318) was grown using ARGET ATRP process as discussed in our previous publications to attain >95% conversion. In this case, molar ratio between vbTMAC (1.60, 7.57 mmol) and HEBiB (31  $\mu$ L, 214  $\mu$ mol) was 35. Copper(II) bromide (Acros, 99%; Lot #A0344238) and tris(2-pyridylmethyl)amine (TPMA) were used to form catalyst complex, and stannous octoate (SnOct) (Sigma-Aldrich, 92.5–100%, Lot #SLBP5072V) was used as reducing agent for ARGET ATRP mediated synthesis.<sup>32,50</sup> 9.0 mL aliquot of polymer reaction mixture (16.1 mL) was extracted and injected into a scintillation vial containing fluorographite (15.1 mg). Since fluorographite is superhydrophobic, its dispersion in aqueous medium is quite a challenge. This mixture was sonicated using sonication probe in a 10 °C bath (RTE-9 Endocal refrigerated circulating bath with coolant) at 72 W cm<sup>-2</sup> for one hour. During this period, the mixture was removed from the set up and manually shaken every 15 minutes at most to get the flakes of fluorographite into aqueous phase. These steps aided in intercalation and physical wrapping of polyelectrolyte in between the fluorographite sheets, resulting in better dispersion. After one hour, mixture was added back in Schlenk flask (SF) and

vial was rinsed with MilliQ-water to obtain most of the fluorographite particles stuck to the glass surface and added to the reaction mixture making a final volume of 22 mL. The mixture was sparged for 10 min, sealed and sonicated at  $100 \text{ W cm}^{-2}$  for another 20 min. After 20 min, ~75 mg of external radical TEMPO were directly added into the reaction mixture and sonicated for one more hour at  $100 \text{ W cm}^{-2}$ . The sonication probe was removed, reaction mixture was sparged for 20 minutes, sealed and then heated to reflux in a  $110^\circ\text{C}$  oil bath for different time durations (one or three days) under  $\text{Ar(g)}$  positive pressure. As the reaction proceeds, color of the reaction mixture changes to darkish grey. After the required duration, functionalization is stopped by removing the heat and exposing to air. Reaction mixture was purified using the same steps as done in our previous publications.<sup>32,50</sup> Dispersion was centrifuged (200,000 g, one hour,  $20^\circ\text{C}$ ) at high ionic strength (4 M  $\text{NaCl(aq)}$ ) to mechanically disrupt physisorbed polymer, and sediments were collected and this process was repeated till the concentration of unbound polymer in the supernatant goes below the detection limit. An overview of rest of the processes are presented in Supplementary Information (Table S4.).

4.3.1.2 Aqueous synthesis of polyelectrolyte functionalized fluorographite in presence of reducing agent, catalyst complex and absence of external radical using sonochemistry and reflux (PFG-II)

PFG-II was synthesized in one-step process. Polyelectrolyte of vbTMAC (Fisher, 97%; Lot #A0311318) was grown using ARGET ATRP process as discussed in our previous publications to attain >95% conversion,<sup>1,2</sup> where molar ratio between vbTMAC (1.60, 7.57 mmol) and HEBiB (31  $\mu\text{L}$ , 214  $\mu\text{mol}$ ) was 35. Additional TPMA (1.04 mg, 3.55  $\mu\text{mol}$ ) and  $\text{CuBr}_2$  solution in water (34.5  $\mu\text{L}$ , 20.6 mM, 0.710  $\mu\text{mol}$ ) were dissolved

in 500  $\mu\text{L}$  of Milli-Q water and purified polymer was added to the SF. The mixture was sparged with  $\text{Ar(g)}$  for 15 min, and 9.0 mL aliquot of polymer reaction mixture (16.6 mL) was extracted and injected into a scintillation vial containing  $\sim 15$  mg of fluorographite. This mixture was sonicated using sonication probe in ice water bath ( $10\text{ }^\circ\text{C}$ ) at  $72\text{ W cm}^{-2}$  for one hour along with manual shaking once every 15 min. After one hour, the mixture was added back in SF and vial was rinsed with MilliQ-water to obtain most of the fluorographite particles stuck to the glass surface and added to the reaction mixture making a final volume of 22 mL. This dispersion was sparged for 10 min, sealed and sonicated at  $100\text{ W cm}^{-2}$  for 1 h 20 min at  $100\text{ W cm}^{-2}$ . The sonication probe is removed, reaction mixture is sparged for 20 more minutes, sealed and then heated to reflux in a  $110\text{ }^\circ\text{C}$  oil bath for 3 days under  $\text{Ar(g)}$  positive pressure. As the reaction proceeds, color of the reaction mixture changes to darkish grey. After the required duration, functionalization is stopped by removing the heat and exposing to air. The reaction mixture is purified using the same steps as done in our previous publications.<sup>1,2</sup> Dispersion was centrifuged (200,000 g, one hour,  $20\text{ }^\circ\text{C}$ ) at high ionic strength (4 M  $\text{NaCl(aq)}$ ) to mechanically disrupt physisorbed polymer, and sediments were collected and this process was repeated till the concentration of unbound polymer in the supernatant goes below the detection limit.

4.3.1.3 Aqueous synthesis of polyelectrolyte functionalized fluorographite in presence of catalyst complex and absence of reducing agent and external radical under sonochemistry and reflux (PFG-III)

PFG-III was synthesized in two-steps processes. Polyelectrolyte of vbTMAC (Fisher, 97%; Lot #A0311318) was grown using ARGET ATRP process as discussed in our previous publications to attain >95% conversion.<sup>1,2</sup> where molar ratio between vbTMAC (1.60, 7.57 mmol) and HEBiB (31  $\mu$ L, 214  $\mu$ mol) was 35. Aqueous reaction mixture of polyelectrolyte was purified off reducing agent using the procedure similar to our previous publication.<sup>2</sup> Reaction mixture was centrifuged (200,000 g, 60 min, 20 °C) for 3 iterations till there was no visible sedimentation of oxidized Sn(OH)<sub>2</sub>(s) observed. Additional TPMA (1.04 mg, 3.55  $\mu$ mol) and CuBr<sub>2</sub> solution in water (34.5  $\mu$ L, 20.6 mM, 0.710  $\mu$ mol) were dissolved in 500  $\mu$ L of Milli-Q water and purified polymer was added to the SF. The mixture was sparged with Ar(g) for 15 min, and 9.0 mL of this reaction mixture (16.6 mL) was injected into a scintillation vial containing ~15 mg of fluorographite. This mixture was sonicated using sonication probe in ice water bath at 72 W cm<sup>-2</sup> for one hour for one hour along with manual shaking once every 15 min. After one hour, the mixture was added in SF, and vial was rinsed with MilliQ-water to obtain most of the fluorographite particles stuck to the glass surface and added to the reaction mixture making a final volume of 22 mL. This dispersion was sparged for 10 min, sealed and sonicated at 100 W cm<sup>-2</sup> for 1 h 20 min at 100 W cm<sup>-2</sup>. The sonication probe is removed, reaction mixture is sparged for 20 more minutes, sealed and then heated to reflux in a 110 °C oil bath for 3 days under Ar(g) positive pressure. As the reaction proceeds, color of the reaction mixture changes to darkish grey which is visual representation of defluorination process. After the required duration, functionalization is stopped by removing the heat and exposing to air to quench the catalyst. The reaction

mixture is purified using the same steps as done in our previous publications.<sup>1,2</sup> and suggested in PFG-I and PFG-II synthesis.

4.3.1.4 Aqueous synthesis of polyelectrolyte functionalized fluorographite in absence of catalyst complex, reducing agent and external radical under sonochemistry and reflux (PFG-IV)

PFG-IV followed the exact same protocol as PF-II. The only difference being no activation by  $\text{CuBr}_2/\text{TPMA}$  complex before sonication with fluorographite.

4.3.1.5 Aqueous synthesis of polyelectrolyte functionalized fluorographite in absence of catalyst complex, reducing agent and external radical under reflux (PFG-V)

PFG-V was synthesized in two-steps processes. Polyelectrolyte of vbTMAC (Fisher, 97%; Lot #A0311318) was grown using ARGET ATRP process as discussed in our previous publications to attain >95% conversion.<sup>1,2</sup> Aqueous solution of polyelectrolyte was purified off reducing agent using the procedure similar to our previous publication.<sup>2</sup> Reaction mixture was centrifuged (200,000 g, 60 min, 20 °C) for 3 iterations till there was no visible sedimentation of oxidized  $\text{Sn}(\text{OH})_2(\text{s})$  observed. Purified polymer<sup>2</sup> solution was sparged with  $\text{Ar}(\text{g})$  for 15 min, and directly added to SF holding ~15 mg of fluorographite. This mixture is shaken vigorously before sealing and heating to reflux in a 110 °C oil bath for 3 days under  $\text{Ar}(\text{g})$  positive pressure. As the reaction proceeds, color of the reaction mixture changes to darkish grey which is visual representation of defluorination process. After the required duration, functionalization is stopped by removing the heat. The reaction mixture is purified using the same steps as done in our previous publications.<sup>1,2</sup> This method did not use sonication.

#### 4.3.1.6 Control studies

Control studies were performed using Schlenk apparatus under Ar where fluorographite (15 mg) was added to MilliQ (22 mL) in a round bottomed flask, and refluxed in a 110 °C oil bath and maintained in a 10 °C RTE-9 Endocal refrigerated circulating bath with coolant, both under stirring for 3 days. Similar experiment was conducted where fluorographite and water mixture was maintained at low temperature using cold bath (10 °C) under sonication at 90 W cm<sup>-2</sup> for 2 h. In another two set of experiment, Poly(ethylene glycol) methyl ether (PEG) (1.01 g, 0.20 mmol) with a molecular weight of 5000 Da was added to fluorographite (15 mg) and MilliQ (22 mL) mixture in SF, and stirred under reflux reaction conditions and in cold bath conditions (10 °C), separately for 3 days.

#### 4.3.2 Characterization Methods.

##### 4.3.2.1 Dynamic Light Scattering

Hydrodynamic diameter and zeta potential of various functionalized PFG batches were measured using Malvern DLS Zetasizer instrument. 10 ng mL<sup>-1</sup> of PFG sample solutions were used for DLS measurements. For Zeta measurements, 2 mg L<sup>-1</sup> of samples were used. An equilibrium time of 15 minutes was allowed in a normal room temperature sample cell. All results were reported as value ± standard error, 95% and outliers were removed.

##### 4.3.2.2. Attenuated Total Reflectance Fourier Transform Infrared Spectroscopy

ATR FTIR spectrometer (PerkinElmer, Spectrum 100) was used to evaluate the presence of constituents of the PFG and fluorographite materials.

#### 4.3.2.3 Raman Spectroscopy

Samples were prepared by drop casting onto silicon wafers as a thin film for all surface enhanced Raman scattering measurements (XploRA Raman confocal microscope system, JY Horiba, Edison, NJ). Raman spectrometer with an excitation wavelength of 532 nm was used to analyze the relative integrated area under D band ( $sp^3$  hybridized carbon), G band ( $sp^2$  hybridized carbon) and 2D band of different samples between 600-3000  $cm^{-1}$ . Peak frequencies were calibrated with silicon at 520  $cm^{-1}$  prior to each use. Data was analyzed and optimizations, like baseline and noise corrections were performed using LabSpec 6 software. In our previous studies, we have already performed control studies on sonication to provide evidence that ultrasonication has very little effect on D:G ratio under similar sonication duration.<sup>50</sup>

#### 4.3.2.4 X-Ray Photoelectron Spectroscopy

Samples were prepared by drop casting PFG sample solutions on Si chips as a thin film. For X-Ray Photoelectron spectroscopy (XPS, EscaLab 250Xi) analysis, monochromatic (1487.6 eV) Al  $K\alpha$ -ray source was used to probe the surface, with a spot size of 250  $\mu m$  and a flood gun was used to limit charging at the surface of the materials. Avantage Processing software package was used to analyze all XPS spectra.

#### 4.3.2.5 X-Ray Powder Diffraction

Crystal phase of PFGs were analyzed using X-Ray Powder Diffraction (XRD, PANalytical (Netherlands) X'Pert PRO). XRD patterns were measured over 2Theta range of 5 – 60 having a step size 0.1000 with 10.0 s per step and scan rate of 0.010° per step.

#### 4.3.2.6 Transmission Electron Microscopy

Morphology of the samples was analyzed by transmission electron microscope (TEM, JEOL JEM-2100Plus, acceleration voltage: 120 kV). For sample preparations, known concentrations of required dispersions were bath sonicated for five minutes at 5 °C with occasional manual shaking. Prepared carbon mesh TEM grids were dipped into the dispersion and dried overnight. For Electron Energy Loss Spectroscopy (EELS) analysis, emission current was set to 12  $\mu\text{A}$ , acquisition time was one second, energy filter aperture was 30  $\mu\text{m}$  and illumination angle was set to 1.250 mrad. Selected area diffraction (SAED) were measured of all the samples deposited in TEM grids.

#### 4.3.2.7 Thermogravimetric Analysis

Thermogravimetric analysis (TGA/SDTA851) of PFG, fluorographite and TEMPO samples were done in Air mode. Mettler software was used to analyze all the measurements.

### 4.3.3 Purification and performance evaluation.

#### 4.3.3.1 Water flux studies

For water flux measurements, thin films of PFGs of different mass densities ( $0.233 \text{ mg cm}^{-2}$ ,  $0.466 \text{ mg cm}^{-2}$ ,  $0.699 \text{ mg cm}^{-2}$ ) were used to evaluate the water flux using Milli-Q as permeate. A known mass of PFG was deposited on 25 mm wide  $0.2 \mu\text{m}$  pore diameter MCE membranes as thin film and a known volume of Milli-Q was pushed through under vacuum with known pressure. Time duration for a known volume of Milli-Q to flow through was recorded and this process was repeated for several (>3) iterations. These thin films were dried for 30 minutes under vacuum and permeate flux

was recorded again for several measurements. Water flux value was estimated from the following equation:  $J_w = \frac{Q}{A\Delta t}$  where  $J_w$  is water flux ( $L\ m^{-2}h^{-1}bar^{-1}$ ),  $Q$  is volume of water (L),  $A$  is the surface area of the layers or film ( $m^2$ ),  $P$  is the pressure (bar) and  $\Delta t$  is the time (h) required for volume  $L$  of Milli-Q to flow through.

#### 4.3.3.2 Kinetic studies

A known amount of PFG-II was added to microcentrifuge tubes holding known concentration of analyte, NaFL and was vortexed for different time durations at 500 rpm at room temperature and neutral pH. At known time intervals, NaFL and PFG-II dispersions were pushed through 13 mm wide 0.2  $\mu m$  pre diameter MCE membranes and concentrations of filtrates were measured using UV-vis-NIR Spectrophotometer (Cary 5000, Agilent Technologies). NaFL stock concentration was measured through control studies where same amount of NaFL was pushed through 13 mm wide MCE membrane without adsorbent. Control experiments were performed in the same conditions without addition of adsorbents.

#### 4.3.3.3 Adsorption Isotherm

A known amount of PFG material was added to the vial holding different known concentration of analyte, NaFL which was vortexed for 4 h at 500 rpm at room temperature and neutral pH. Samples were filtered through 13 mm wide 0.2  $\mu m$  pore size MCE membranes before analysis under UV-vis-NIR Spectrophotometer for adsorbent removal. Control studies were performed using fluorographite where known concentration of NaFL was incubated for 24 h using known mass of fluorographite powder and mixture was filtered and analyzed under UV-vis-NIR Spectrophotometer.

#### 4.3.3.4 Analyte adsorption studies

We tested removal of compounds under emerging contaminants category, especially those mentioned by US EPA to evaluate the potential of our materials as smart point-of-use water purification systems that can remove contaminants of immediate concern. We demonstrated removal of perfluoroalkylated substances (PFAS) (viz., perfluorooctanoic acid (PFOA) and perfluorooctanesulfonate (PFOS)), iodinated X-ray contrast media (diatrizoic acid, DTZA)<sup>21</sup> and oxyanions of metalloids specifically  $\text{CrO}_4^{2-}$ ,  $\text{VO}_4^{3-}$ ,  $\text{WO}_4^{2-}$ , arsenic (V) oxide hydrate ( $\text{H}_2\text{AsO}_4^{-1}/\text{HAsO}_4^{2-}$ ) and arsenic trioxide/sodium hydroxide ( $\text{AsO}_3^{3-}/\text{OH}^{-1}$ ). Quantitative analysis of all oxyanions was performed using inductively coupled plasma atomic emission spectroscopy (ICP OES, 5100 Agilent California) and rest of the analytes were measured using liquid chromatograph (LC) equipped with electrospray mass spectrometry (MS, Thermo Scientific, LTQ Velos Pro) using MS mode only. The detections were in negative ion mode for PFOA and PFOS while in positive ion mode for DTZA with mobile phase A comprising of 0.5% formic acid in 100% LC-MS grade water and mobile phase B of 100% LC-MS grade acetonitrile. All oxyanions standards for calibration of ICP OES were made using 2% (v/v) nitric acid and all stock solution for water testing were made using MilliQ water. Concentrations were calculated from standard concentration curves and limits of quantification of each compound was analyzed. Concentrations of all compounds were determined by linear least square regression model of standard concentrations. For MS and ICP OES, every sample was run in duplicates or triplicates.

#### 4.3.3.5 Regeneration Studies

A known mass of PFG was deposited onto 25 mm wide 0.2  $\mu\text{m}$  MCE membrane and that membrane placed in a glass vial. The film was allowed to incubate in brine

solution (1.5 mL, 2.0 M NaCl(aq)) for 5 min. Brine was disposed of and MilliQ was used to rinse the remaining brine (3 replicates, 1.5 ml). A known volume and concentration of NaFL(aq) was added and allowed to incubate for 5 min and concentration of NaFL(aq) solution after incubation was measured using UV-vis spectroscopy. In the subsequent brine rinses, the NaFL saturated films were regenerated by incubating in successive brine solutions (1.5 mL, 2.0 M NaCl(aq)) until the concentration of desorbed NaFL solution dropped down to 0.02 mg-C L<sup>-1</sup>.

#### 4.4 Results and Discussion

##### 4.4.1 Synthesis, morphological and physicochemical characterization of poly(vbTMAC) functionalized fluorographite (PFG):

Fluorographite is an insulator with highly stable C-F bonds, and its bond dissociation energy is higher than 418 kJ mol<sup>-1</sup>.<sup>25</sup> However, a lot of research have demonstrated the instability of C-F bonds in fluorographite in presence of nucleophiles and/or external radical agents. Yet, little/no research has been done in the field of covalent grafting of functional polymer brushes on defluorinated domains of fluorographite for sustainable applications. In this study, we have investigated surface modification and functionalization of fluorographite in presence of grown (>95% conversion) polyelectrolyte brushes generated by activators regeneration by electron transfer assisting atom transfer radical polymerization (ARGET ATRP) in water under neutral pH conditions. Fluorographite is insoluble in water but after defluorination and functionalization in presence of polyelectrolyte, it turns into black dispersion (as shown in Figure S4.1). Our observations have been consistent with the reaction mechanism of fluorographite defluorination in presence of TEMPO radicals as discussed by Lai et al.<sup>13</sup>

The incoming polyelectrolyte radicals attack the F atoms on fluorographite and generates spin centers. Spin centers are a good source of polyelectrolyte functionalization centers. Two spin centers adjacent to one another may lead to the formation of C=C bonds. This generation of graphitic regions is prominent in XPS analysis where the deconvolutions of carbon peak fit of PFG-V exhibited an intensified C=C bond peak (as shown in Figure 4.1(d)). In addition to this, functionalization with styrenic polymers will also add to the detection of C=C bonds. Hence, thermogravimetric analysis (TGA) was performed to understand functionalization. Tuning to maximum functionality of polyelectrolyte brushes is beyond the scope of this paper. Attenuated Total Reflectance Fourier Transform Infrared Spectroscopy (ATR FTIR) spectra of purified PFG-V confirmed the functionalization of polyelectrolyte strands of vbTMAC due to presence of  $1487\text{ cm}^{-1}$  and  $1638\text{ cm}^{-1}$  owing to the presence of C-N stretching vibration due to ammonium group and stretching of double bonded carbon in the styrene ring of vbTMAC.<sup>24</sup> Additionally, defluorination and graphitic regions in PFG-V also contributed to  $1638\text{ cm}^{-1}$  vibration peak. Fluorographite exhibited a sharp C-F absorption stretch at  $1199\text{ cm}^{-1}$  while PFG-V exhibited a reduced blue-shifted C-F stretch at  $1207\text{ cm}^{-1}$ .<sup>26</sup> In PFG-V spectra, C-H stretch at  $2967\text{ cm}^{-1}$  corresponded to polymerized vbTMAC.<sup>27</sup> For comparison, ATR FTIR analysis of PFG-II has been shown in Figure S4.2. We compared defluorination of fluorographite mediated by ARGET ATRP assisted polyelectrolyte in presence (PFG-I) and absence (PFG-V) of TEMPO. Defluorination of PFGs was confirmed with X-ray photoelectron spectroscopy (XPS) analysis (as shown in Figure 4.1(b) and Table 4.1). Comparison of C 1s spectra of fluorographite and PFG-I demonstrated (as illustrated in Figure 4.1) decrease in intensity of binding energy of C-F bond peaks at 288.4 eV. C 1s

spectra of PFG-I can be found as Figure S4.3 in the supplementary information. There is appearance of new peak at 284.6 eV due to the  $sp^2$  hybridized carbon as an outcome of defluorination and functionalization of poly(vbTMAC). It was observed that PFG-V resulted in higher defluorination without the requirement of any external radical. Additionally, TEMPO is capable of capturing carbon radicals (i.e., polyelectrolyte radicals in our case) which would have decreased the yield of active polymer radical chains.<sup>28</sup> This analysis of effective defluorination was further corroborated by the EELS analysis when comparing the F-K edge of fluorographite with F-K edge of PFG-V at 700 eV (as shown in Figure 4.2).

Control studies were performed to analyze behavior of fluorographite without the presence of polymeric agents. When fluorographite was refluxed in MilliQ, the color of fluorographite turned dark grey/blackish sitting in water showing no visible signs of dispersibility (as shown in Figure 4.11). Reactions involving refluxing with PEG showed some dispersion of fluorographite as the physisorbed polymer acted as a surfactant wrapped around fluorographite but showed no change in elemental composition. This concluded the fact that high temperature reflux and soluble polymers are ineffective in stimulating defluorination and role of poly(vbTMAC) is significant in defluorination process.

TGA was used to investigate the thermal stability of purified PFG resins (as shown in Figure S4.4). There was initial 2-4% weight loss in all the PFG samples due to remnants of solvents. Residual TEMPO was lost within 125 °C and does not contribute to weight loss by polymer or fluorographite in PFG-I sample. Initial drop from 125° C to 400 °C was ascribed to the mass loss pertaining to poly(vbTMAC) due to styrene and

quaternary ammonium decomposition.<sup>29</sup> Second significant weight loss from 400-600 °C was due to loss of F in graphite.<sup>30,31</sup> Transmission electron micrographs (TEM) of fluorographite and PFG-I were compared to understand the difference in morphology. TEM of Fluorographite is opaque due to thickness from stacking of large sheets. PFGs have slightly different morphology. They resemble smaller crystallites of fluorographite with functionalization of poly(vbTMAC) brushes having globular morphology. From our previous works,<sup>32</sup> we have calculated the radius of gyration of 26 mer polyelectrolyte to be 1.7 nm and on resolving the TEM images, the globular shaped polyelectrolyte brushes in highly functionalized domains resembled fully grown polymers of 33 mer. TEM image of PFG-V is shown in Figure S4.5.

To investigate structural parameters, X-Ray Powder Diffraction (XRD) analysis of PFG-I was compared with fluorographite. In XRD, as shown in Figure 4.4, when compared with fluorographite, the peak intensity of (002) reflection peak at  $2\theta = 26.8^\circ$  of PFG-I is significantly pronounced, which indicated the preservation of graphitic structure in PFG-I due to defluorination.<sup>33</sup> This  $2\theta$  value corresponds to d-spacing (or interlaminar spacing) of 0.33 nm (calculated from Bragg equation), which was consistent with the selected area electron diffraction (SAED) patterns of PFG-I and PFG-V obtained by Transmission Electron Microscopy (TEM) analysis (Table 1 shown in Supplementary Information).  $2\theta = 12.9^\circ$  demonstrated (001) reflection peak corresponding to hexagonal structure with high fluorine content in fluorographite. After polyelectrolyte functionalization, this peak was significantly reduced in intensity in PFG-I without any trace in XRD or selected area electron diffraction (SAED) analysis. Another characteristic (004) reflection peak of PFG-I was prominent at  $2\theta = 51.7^\circ$  which

corroborates with the crystalline structure of graphite due to defluorination.<sup>34,35</sup> This peak corresponds to d-spacing of 0.18 nm which was supported by SAED patterns of PFG-I and PFG-V. Fluorographite reflection peak at  $2\theta = 41.0^\circ$  was visible in the SAED pattern of PFG-V corresponding to a d-spacing of 0.22 nm. This (100) reflection peak corresponds to C-C in plane length in the reticular system.<sup>30,36,37</sup> There is a reflection peak at  $2\theta = 33.9^\circ$ , which corresponds to d-spacing of 0.26 nm in XRD of PFG-I that agrees well with SAED patterns of PFG-I and PFG-V.

The number of layers in graphitic materials can be calculated by combining Debye-Scherrer ( $D = \frac{K\lambda}{\beta\cos\theta}$ ) and Bragg equation ( $d = \frac{\lambda}{2\sin\theta}$ ) resulting in  $N = \left(\frac{D}{d} + 1\right)$  where D is the average crystal height, d is the interplanar spacing,  $\beta$  is full width half maxima and  $\lambda$  is wavelength of X-ray source. Considering (002) reflection peak contributing to inter-layer spacing for PFG-I, K is a crystallite shape constant equal to 0.89 for spherical crystals with cubic unit cells,<sup>38</sup>  $\beta$  as  $1.887^\circ$ ,  $\lambda$  as 0.154 nm, D and d was calculated to be 4.52 and 0.34 nm, respectively. This results in N being equal to 14 layers and when the number of layers are close to 10, they define graphitic properties.<sup>39</sup> Hydrodynamic diameter and zeta potential of PFGs were measured using DLS Zetasizer (as shown in Figure S4.6-S4.9 and Table S4.2). These particle sizes corroborated with size of graphene sheets.<sup>40</sup> Zeta potential is positive for all the PFG batches denoting positively charged polyelectrolyte bound to fluorographite.

Functionalization density is proportional to the intensity ratio between D ( $I_D$ ) and G band ( $I_G$ ) (D:G ratio). Since, fluorographite is already covalently modified with F atoms attached to every single C atom and we functionalize the defluorinated regions simultaneously with incoming polymer, D:G ratio does not play an important role in

determining the % functionalization in this case. Measured D:G ratio of fluorographite, PFG-I and PFG-V were 0.99, 0.93 and 1.30, respectively. These values corroborate the inadequacy of D:G ratio in establishing accountability on functionalization. Raman spectra of fluorographite and PFG-V are shown in Figure 4.5. 2D peak in Raman is an important metric for understanding the exfoliation of graphite into graphene layers but due to high functionalization of PFG-V, there is broadening of Raman bands which also includes 2D band ( $2717\text{ cm}^{-1}$ ) that makes it difficult to infer much information about 2D band.<sup>41,42</sup> Crystallite size (L) of graphitic materials can be calculated using the equation  $L\text{ (nm)} = (2.4 \times 10^{-10})\lambda \frac{I_D}{I_G}^{-1}$  where  $\lambda$  is the laser wavelength.<sup>43</sup> The crystallite sizes are listed in Table 3.

#### 4.4.2 Morphology of thin films, Adsorption Kinetics and Isotherm, Water Purification Testing:

Understanding the morphology of thin film assembly of PFG resins is important in order to predict the structure-property-function relationship. We performed SEM analysis on thin films of PFG-II to understand the assembly of graphitic layers for effective target contaminant removal and high water flux (as shown in Figure 4.6). It was observed that PFG films exhibited stacking assembly of oblong shaped crystallites without pin holes or cracks (as shown in Figure 4.6(a)). In Figure 4.6(b), the presence of cavity is the result of dislodging of a particle that formed part of the film during sample preparation. The stacking assembly of the bottom layers were clearly observed with glimpses of various layers making up the film. Bosch-Navarro et al. demonstrated

similar morphology of exfoliated fluorographite functionalized with amine functionalities.<sup>44</sup>

Adsorption kinetics of PFG-II was plotted as shown in the Figure 4.7. On extrapolating the trendline, it was observed that pseudoequilibrium “ $q_e$ ” is achieved within few seconds. This behavior is similar to polyelectrolyte functionalized single walled carbon nanotubes (NanoResin) published in our previous works.<sup>27,32</sup> It is due to the fact that these PFGs are open resins with large specific surface area making most of the binding sites accessible. We analyzed adsorption isotherm behavior of PFG materials where we have plotted adsorption loading,  $q$  as a function of equilibrium concentration,  $C_e$  (as shown in Figure 4.8). Adsorption isotherm curves of PFG resins were fit using Langmuir and Freundlich models, and AIC testing was performed to understand the probability of better fit. Parameters derived from all the curve fittings are shown in Table S4. According to Akaike’s Information Criterion test (AIC), Freundlich demonstrated better fitting with an AIC of 21.4 compared to Langmuir with AIC of 31.6 in PFG-V. Control studies were performed to analyze the sorption ability of fluorographite. 2 ml of 3.00 mg-C/L of NaFL was incubated overnight with 1.0 mg of fluorographite and sample was filtered through 13 mm wide 0.2  $\mu\text{m}$  pore size MCE membranes after 24 hours, and analyzed using UV-vis-NIR Spectrophotometer. It resulted in negligible removal (0.60 mg-C/L).

Studies have shown that composites rich in fluorine content demonstrate high capacity removal of fluorinated contaminants. Yang et al. investigated removal of GenX with an initial adsorption concentration of 10  $\mu\text{g L}^{-1}$  and incubated with 100  $\text{mg L}^{-1}$  of cross-linked  $\beta$ -cyclodextrin containing fluoropolymers for 24 h for batch adsorption

studies. They demonstrated low removal (<10%) at neutral pH compared to acidic conditions (pH = 3.9) that resulted in 50-90% removal. They performed low concentration kinetics studies at  $1 \mu\text{g L}^{-1}$  stock concentrations of PFAS and  $100 \text{ mg L}^{-1}$  of adsorbent, and achieved >90% after 48 h.<sup>45</sup> Shetty et al. evaluated adsorption of PFOA with an initial concentration of  $1 \mu\text{g L}^{-1}$  and stirred with 0.5 mg of fluorine-rich calixarene based porous polymers at neutral pH that demonstrated 79 – 100% removal within 80 hours compared to 23 – 64% removal with non-fluorinated analogues.<sup>46</sup> However, these materials were synthesized using toxic solvents and the adsorption kinetics is slow. We have demonstrated adsorption at faster kinetics and high water flux with associated high % removal.

We prepared thin films of our materials on mixed ester cellulose (MCE) membranes and employed it for fast filtration of contaminants as opposed to incubation studies that has been explored extensively by researchers to perform adsorption studies with porous materials that do not have high open resin surface area like our materials. Membrane density and water flux measurements are shown in Table 4 and S3. The plate-like morphology supports easy transport of water channels resulting in high water flux. We tested PFOS and PFOA removal with a stock concentration of  $95.64 \mu\text{g L}^{-1}$  and  $95.02 \mu\text{g L}^{-1}$ , respectively and achieved >99% removal using a PFG-I thin film deposited ( $2.2 \mu\text{m}$ ,  $0.466 \text{ mg cm}^{-1}$ ) on MCE membrane, with a water flux of  $1870 \text{ L m}^{-2} \text{ h}^{-1} \text{ bar}^{-1}$  at one atm pressure. This water flux is 19 folds higher than graphene oxide membrane (thickness <  $1 \mu\text{m}$ ) with a water flux of  $95 \text{ L m}^{-2} \text{ h}^{-1} \text{ bar}^{-1}$  at one atm pressure.<sup>47</sup> Semi-fluorination in functionalized PFG-I impart fluorophilic property that support faster and effective removal of PFAS. The data showing removal of all emerging contaminants can

be found in Figure 4.9. We were able to remove DTZA upto 88% using an analyte concentration of  $117 \mu\text{g L}^{-1}$  due to the  $\pi$ - $\pi$  interactions with PFG-I. The MDL of all the contaminants screened using only the MS method was close to 1 ppb.

We investigated removal of metalloids oxyanions in the form of  $\text{CrO}_4^{2-}$ ,  $\text{VO}_4^{3-}$ ,  $\text{WO}_4^{2-}$  and  $\text{H}_2\text{AsO}_4^{1-}/\text{HasO}_4^{2-}$  using PFG-I resins. MDL values in accordance to ICP OES and MCL values of these metal ions specified by US EPA<sup>48</sup> are presented in Table S5. There is no MCL specified for W by US EPA but as a reference, we are considering the standard established by the Occupational Safety and Health Administration of  $3 \mu\text{g L}^{-1}$  as 15-minute short term exposure limit for airborne exposure to soluble tungsten.<sup>49</sup> Stock concentrations of these oxyanions were prepared above the MCL limit but within the range of environmentally relevant concentrations as shown in Table S4. We obtained a facile >99% removal of all oxyanions with filtrate concentrations reaching well below MCL limit. We investigated co-selectivity of PFG-I to metalloids oxyanions by using a stock solution of  $160 \mu\text{g L}^{-1}$  of arsenic trioxide in 0.2% sodium hydroxide ( $\text{AsO}_3^{3-}/\text{OH}^{1-}$ ), and achieved 62.5% removal by fast filtration using a PFG-I film with  $1.86 \text{ mg cm}^{-1}$  mass density (as shown in Figure 4.10). This proves selectivity of PFG to pervasive contaminants even in presence of other electrolytes under environmentally relevant concentrations.

We tested regeneration behavior of PFG-I resins by using the same vial incubation protocol as used in our previous works.<sup>32</sup> Regeneration studies demonstrated a slope of  $-0.014 \pm 0.052\%$  per cycle which means the material should maintain effectiveness till 85% even after working for 1000 cycles. Subsequent studies will include using these resins for breakthrough regeneration and reuse purposes.

PFG resins have unique structure that supports faster kinetics, high percent removal and high water flux. These materials have been fabricated keeping small systems in mind and extensive structural studies incorporating several cycles of breakthrough studies have not been studied. Semi-fluorination and functionalization density are important parameters for facile fabrication on MCE membranes. We will further investigate the dependence of structural integrity on the polyelectrolyte length and density, and maximum defluorination.

#### 4.5 Conclusion

In summary, this research study was aimed at understanding and taking advantage of facile defluorination and covalent grafting of fluorographite in green environment. Aqueous synthesis of defluorination and subsequent functionalization of fluorographite was performed to obtain functional graphitic materials for water purification purposes. This 2D material demonstrated a balanced structure-property-function relationship of high percent removal (>90%), high membrane water flux ( $1870 \text{ L m}^{-2}\text{h}^{-1}\text{bar}^{-1}$ ) and faster kinetics due to surface functionalization. PFGs demonstrated high potential to thrive in better than graphene oxide analogues and other materials synthesized under caustic/toxic conditions. Kinetics of analyte adsorption using PFG resins resin were rapid ( $\leq$  one minute) demonstrating Freundlich/Langmuir curve with  $K_f$  value of  $14.4 \text{ (mg/g)(L/mg)}$  corroborating good binding strength due to open resin structure. Transmission electron micrographs revealed crystalline sheets with poly(vbTMAC) functionalized domains. These resins were capable of high percent removal of emerging

pervasive analytes under environmentally relevant concentrations close to MCL.

Therefore, highly functionalized PFG materials are advanced model for next generation high capacity removal of contaminants of emerging concern and other sustainable technology applications.

#### 4.6 References:

1. Nine, M. J.; Cole, M. A.; Tran, D. N. H., Losic, D. Graphene: a multipurpose material for protective coatings. *J Mater Chem A*. **2015**, *3* (24), 12580-12602 10.1039/c5ta01010a
2. Hummers, W. S., Offeman, R. E. PREPARATION OF GRAPHITIC OXIDE. *J Am Chem Soc*. **1958**, *80* (6), 1339-1339 10.1021/ja01539a017
3. Furst, A.; Berlo, R. C., Hooton, S. HYDRAZINE AS A REDUCING AGENT FOR ORGANIC COMPOUNDS ( CATALYTIC HYDRAZINE REDUCTIONS. *Chemical Reviews*. **1965**, *65* (1), 51-& 10.1021/cr60233a002
4. Yang, Z. Q.; Sun, W.; Wang, L. D.; Li, S. J.; Zhu, T. Z., Liu, G. C. Liquid-phase exfoliated fluorographene as a two dimensional coating filler for enhanced corrosion protection performance. *Corrosion Science*. **2016**, *103*, 312-318 10.1016/j.corsci.2015.10.039
5. Huang, W. X.; Pei, Q. X.; Liu, Z. S., Zhang, Y. W. Thermal conductivity of fluorinated graphene: A non-equilibrium molecular dynamics study. *Chem Phys Lett*. **2012**, *552*, 97-101 10.1016/j.cplett.2012.09.043
6. Bulusheva, L. G.; Tur, V. A.; Fedorovskaya, E. O.; Asanov, I. P.; Pontiroli, D.; Ricco, M., Okotrub, A. V. Structure and supercapacitor performance of graphene materials obtained from brominated and fluorinated graphites. *Carbon*. **2014**, *78*, 137-146 10.1016/j.carbon.2014.06.061
7. Urbanova, V.; Karlicky, F.; Matej, A.; Sembera, F.; Janousek, Z.; Perman, J. A.; Ranc, V.; Cepe, K.; Michl, J.; Otyepka, M., Zboril, R. Fluorinated graphenes as advanced biosensors - effect of fluorine coverage on electron transfer properties and adsorption of biomolecules. *Nanoscale*. **2016**, *8* (24), 12134-12142 10.1039/c6nr00353b
8. Das, S.; Sudhagar, P.; Verma, V.; Song, D.; Ito, E.; Lee, S. Y.; Kang, Y. S., Choi, W. Amplifying Charge-Transfer Characteristics of Graphene for Triiodide Reduction in Dye-Sensitized Solar Cells. *Advanced Functional Materials*. **2011**, *21* (19), 3729-3736 10.1002/adfm.201101191
9. Zhu, M. S.; Xie, X. D.; Guo, Y. L.; Chen, P. L.; Ou, X. W.; Yu, G., Liu, M. H. Fluorographene nanosheets with broad solvent dispersibility and their applications as a modified layer in organic field-effect transistors. *Physical Chemistry Chemical Physics*. **2013**, *15* (48), 20992-21000 10.1039/c3cp53383b
10. Ho, K. I.; Huang, C. H.; Liao, J. H.; Zhang, W. J.; Li, L. J.; Lai, C. S., Su, C. Y. Fluorinated Graphene as High Performance Dielectric Materials and the

- Applications for Graphene Nanoelectronics. *Scientific Reports*. **2014**, *4*, 10.1038/srep05893
11. Medved, M.; Zoppellaro, G.; Ugolotti, J.; Matochova, D.; Lazar, P.; Pospisil, T.; Bakandritsos, A.; Tucek, J.; Zboril, R., Otyepka, M. Reactivity of fluorographene is triggered by point defects: beyond the perfect 2D world. *Nanoscale*. **2018**, *10* (10), 4696-4707 10.1039/c7nr09426d
  12. Sandford, G. Perfluoroalkanes. *Tetrahedron*. **2003**, *59* (4), 437-454 10.1016/s0040-4020(02)01568-5
  13. Lai, W. C.; Xu, D. Z.; Wang, X.; Wang, Z. M.; Liu, Y.; Zhang, X. J.; Li, Y. L., Liu, X. Y. Defluorination and covalent grafting of fluorinated graphene with TEMPO in a radical mechanism. *Physical Chemistry Chemical Physics*. **2017**, *19* (35), 24076-24081 10.1039/c7cp04439a
  14. Chronopoulos, D. D.; Bakandritsos, A.; Pykal, M.; Zbořil, R., Otyepka, M. Chemistry, properties, and applications of fluorographene. *Applied materials today*. **2017**, *9*, 60-70
  15. Kouloumpis, A.; Chronopoulos, D. D.; Potsi, G.; Pykal, M.; Vlcek, J.; Scheibe, M., Otyepka, M. One-Step Synthesis of Janus Fluorographene Derivatives. *Chem-Eur J*. **2020**, *26* (29), 6518-6524 10.1002/chem.201905866
  16. Rajeena, U.; Akbar, M.; Raveendran, P., Ramakrishnan, R. M. Fluorographite to hydroxy graphene to graphene: a simple wet chemical approach for good quality graphene. *New J Chem*. **2018**, *42* (12), 9658-9665 10.1039/c8nj01392f
  17. Baumgartner, R., McNeill, K. Hydrodefluorination and hydrogenation of fluorobenzene under mild aqueous conditions. *Environmental science & technology*. **2012**, *46* (18), 10199-10205
  18. Ssebugere, P.; Sillanpää, M.; Matovu, H.; Wang, Z.; Schramm, K.-W.; Omwoma, S.; Wanasolo, W.; Ngeno, E. C., Odongo, S. Environmental levels and human body burdens of per-and poly-fluoroalkyl substances in Africa: A critical review. *Science of The Total Environment*. **2020**, 139913
  19. Wu, N.; Cai, D.; Guo, M.; Li, M., Li, X. Per-and polyfluorinated compounds in saleswomen's urine linked to indoor dust in clothing shops. *Science of The Total Environment*. **2019**, *667*, 594-600
  20. Mamsen, L. S.; Björvang, R. D.; Mucs, D.; Vinnars, M.-T.; Papadogiannakis, N.; Lindh, C. H.; Andersen, C. Y., Damdimopoulou, P. Concentrations of perfluoroalkyl substances (PFASs) in human embryonic and fetal organs from first, second, and third trimester pregnancies. *Environment international*. **2019**, *124*, 482-492 <https://doi.org/10.1016/j.envint.2019.01.010>

21. Nowak, A.; Pacek, G., Mroziak, A. Transformation and ecotoxicological effects of iodinated X-ray contrast media. *Rev Environ Sci Bio-Technol.* **2020**, *19* (2), 337-354 10.1007/s11157-020-09534-0
22. Weidner, E., Ciesielczyk, F. Removal of Hazardous Oxyanions from the Environment Using Metal-Oxide-Based Materials. *Materials.* **2019**, *12* (6), 32 10.3390/ma12060927
23. Kailasam, V., Rosenberg, E. Oxyanion removal and recovery using silica polyamine composites. *Hydrometallurgy.* **2012**, *129*, 97-104 10.1016/j.hydromet.2012.08.010
24. Perez, J.; Toledo, L.; Campos, C. H.; Yanez, J.; Rivas, B. L., Urbano, B. F. Arsenic sorption onto an aluminum oxyhydroxide-poly (4-vinylbenzyl)trimethylammonium chloride hybrid sorbent. *RSC Adv.* **2016**, *6* (34), 28379-28387 10.1039/c6ra01230b
25. Dubecky, M.; Otyepkova, E.; Lazar, P.; Karlicky, F.; Petr, M.; Cepe, K.; Banas, P.; Zboril, R., Otyepka, M. Reactivity of Fluorographene: A Facile Way toward Graphene Derivatives. *J Phys Chem Lett.* **2015**, *6* (8), 1430-1434 10.1021/acs.jpcllett.5b00565
26. Yang, Y.; Lu, G. L.; Li, Y. J.; Liu, Z. Z., Huang, X. Y. One-Step Preparation of Fluorographene: A Highly Efficient, Low-Cost, and Large-Scale Approach of Exfoliating Fluorographite. *ACS Applied Materials & Interfaces.* **2013**, *5* (24), 13478-13483 10.1021/am405046u
27. Johnson, B. R.; Eldred, T. B.; Nguyen, A. T.; Payne, W. M.; Schmidt, E. E.; Alansari, A. Y.; Amburgey, J. E., Poler, J. C. High-Capacity and Rapid Removal of Refractory NOM Using Nanoscale Anion Exchange Resin. *ACS Applied Materials & Interfaces.* **2016**, *8* (28), 18540-18549 10.1021/acsami.6b04368
28. Wang, Z. H.; Wang, Z. H.; Pan, X. C.; Fu, L. Y.; Lathwal, S.; Olszewski, M.; Yan, J. J.; Enciso, A. E.; Wang, Z. Y.; Xia, H. S., Matyjaszewski, K. Ultrasonication-Induced Aqueous Atom Transfer Radical Polymerization. *ACS Macro Lett.* **2018**, *7* (3), 275-280 10.1021/acsmacrolett.8b00027
29. Ianchis, R.; Donescu, D.; Cinteza, L. O.; Purcar, V.; Nistor, C. L.; Petcu, C.; Nicolae, C. A.; Gabor, R., Preda, S. Polymer-clay nanocomposites obtained by solution polymerization of vinyl benzyl triammonium chloride in the presence of advanced functionalized clay. *J Chem Sci.* **2014**, *126* (3), 609-616 10.1007/s12039-014-0621-0
30. Gong, P. W.; Wang, Z. F.; Wang, J. Q.; Wang, H. G.; Li, Z. P.; Fan, Z. J.; Xu, Y.; Han, X. X., Yang, S. R. One-pot sonochemical preparation of fluorographene and

- selective tuning of its fluorine coverage. *J Mater Chem.* **2012**, 22 (33), 16950-16956 10.1039/c2jm32294c
31. Sun, C. B.; Feng, Y. Y.; Li, Y.; Qin, C. Q.; Zhang, Q. Q., Feng, W. Solvothermally exfoliated fluorographene for high-performance lithium primary batteries. *Nanoscale.* **2014**, 6 (5), 2634-2641 10.1039/c3nr04609e
  32. Sahu, A.; Blackburn, K.; Durkin, K.; Eldred, T. B.; Johnson, B. R.; Sheikh, R.; Amburgey, J. E., Poler, J. C. Green synthesis of nanoscale anion exchange resin for sustainable water purification. *Environmental Science: Water Research & Technology.* **2018**, 4 (10), 1685-1694
  33. Ramoraswi, N. O., Ndungu, P. G. Photo-Catalytic Properties of TiO<sub>2</sub> Supported on MWCNTs, SBA-15 and Silica-Coated MWCNTs Nanocomposites. *Nanoscale Research Letters.* **2015**, 10, 16 10.1186/s11671-015-1137-3
  34. Ban, F. Y.; Majid, S. R.; Huang, N. M., Lim, H. N. Graphene Oxide and Its Electrochemical Performance. *International Journal of Electrochemical Science.* **2012**, 7 (5), 4345-4351
  35. Sayah, A.; Habelhames, F.; Bahloul, A.; Nessark, B.; Bonnassieux, Y.; Tendelier, D., El Jouad, M. Electrochemical synthesis of polyaniline-exfoliated graphene composite films and their capacitance properties. *Journal of Electroanalytical Chemistry.* **2018**, 818, 26-34 10.1016/j.jelechem.2018.04.016
  36. Ye, X. Y.; Gong, P. W.; Wang, J. Q.; Wang, H. G.; Ren, S. L., Yang, S. R. Fluorinated graphene reinforced polyimide films with the improved thermal and mechanical properties. *Compos Pt A-Appl Sci Manuf.* **2015**, 75, 96-103 10.1016/j.compositesa.2015.04.005
  37. Tian, R.; Jia, X. H.; Yang, J.; Li, Y., Song, H. J. Large-scale, green, and high-efficiency exfoliation and noncovalent functionalization of fluorinated graphene by ionic liquid crystal. *Chem Eng J.* **2020**, 395, 9 10.1016/j.cej.2020.125104
  38. Sharma, R.; Chadha, N., Saini, P. Determination of defect density, crystallite size and number of graphene layers in graphene analogues using X-ray diffraction and Raman spectroscopy. *Indian J Pure Appl Phys.* **2017**, 55 (9), 625-629
  39. Stobinski, L.; Lesiak, B.; Malolepszy, A.; Mazurkiewicz, M.; Mierzwa, B.; Zemek, J.; Jiricek, P., Bieloshapka, I. Graphene oxide and reduced graphene oxide studied by the XRD, TEM and electron spectroscopy methods. *J Electron Spectrosc Relat Phenom.* **2014**, 195, 145-154 10.1016/j.elspec.2014.07.003
  40. Lotya, M.; Rakovich, A.; Donegan, J. F., Coleman, J. N. Measuring the lateral size of liquid-exfoliated nanosheets with dynamic light scattering. *Nanotechnology.* **2013**, 24 (26), 6 10.1088/0957-4484/24/26/265703

41. Engiert, J. M.; Vecera, P.; Knirsch, K. C.; Schafer, R. A.; Hauke, F., Hirsch, A. Scanning-Raman-Microscopy for the Statistical Analysis of Covalently Functionalized Graphene. *Acs Nano*. **2013**, 7 (6), 5472-5482 10.1021/nn401481h
42. Englert, J. M.; Dotzer, C.; Yang, G. A.; Schmid, M.; Papp, C.; Gottfried, J. M.; Steinruck, H. P.; Spiecker, E.; Hauke, F., Hirsch, A. Covalent bulk functionalization of graphene. *Nat Chem*. **2011**, 3 (4), 279-286 10.1038/nchem.1010
43. Aguilar-Bolados, H.; Contreras-Cid, A.; Yazdani-Pedram, M.; Acosta-Villavicencio, G.; Flores, M.; Fuentealba, P.; Neira-Carrillo, A.; Verdejo, R., Lopez-Manchado, M. A. Synthesis of fluorinated graphene oxide by using an easy one-pot deoxyfluorination reaction. *J Colloid Interface Sci*. **2018**, 524, 219-226 10.1016/j.jcis.2018.04.030
44. Bosch-Navarro, C.; Walker, M.; Wilson, N. R., Rourke, J. P. Covalent modification of exfoliated fluorographite with nitrogen functionalities. *J Mater Chem C*. **2015**, 3 (29), 7627-7631 10.1039/c5tc01633a
45. Yang, A.; Ching, C.; Easler, M.; Helbling, D. E., Dichtel, W. R. Cyclodextrin Polymers with Nitrogen-Containing Tripodal Crosslinkers for Efficient PFAS Adsorption. *ACS Materials Letters*. **2020**
46. Shetty, D.; Jahovic, I.; Skorjanc, T.; Erkal, T. S.; Ali, L.; Raya, J.; Asfari, Z.; Olson, M. A.; Kirmizialtin, S., Yazaydin, A. O. Rapid and Efficient Removal of Perfluorooctanoic Acid from Water with Fluorine-Rich Calixarene-Based Porous Polymers. *ACS Applied Materials & Interfaces*. **2020**
47. You, Y.; Jin, X. H.; Wen, X. Y.; Sahajwalla, V.; Chen, V.; Bustamante, H., Joshi, R. K. Application of graphene oxide membranes for removal of natural organic matter from water. *Carbon*. **2018**, 129, 415-419 10.1016/j.carbon.2017.12.032
48. USEPA. "2018 Edition of the Drinking Water Standards and Health Advisories Tables". **2018**. <https://www.epa.gov/sites/production/files/2018-03/documents/dwtable2018.pdf>.
49. USEPA. "Technical Fact Sheet – Tungsten". **2014**. [https://www.epa.gov/sites/production/files/2014-03/documents/ffrofactsheet\\_contaminant\\_tungsten\\_january2014\\_final.pdf](https://www.epa.gov/sites/production/files/2014-03/documents/ffrofactsheet_contaminant_tungsten_january2014_final.pdf).
50. Sahu, A.; Sheikh, R., Poler, J. C. Green Sonochemical Synthesis, Kinetics and Functionalization of Nanoscale Anion Exchange Resins and their Performance as Water Purification Membranes. *Ultrasonics Sonochemistry*. **2020**, 105163 <https://doi.org/10.1016/j.ultsonch.2020.105163>

## 4.7 Figures and Tables

Table 4.1. Elemental composition (in terms of At%) of fluorographite, fluorographite under reflux (control studies) PFG-I and PFG-V analyzed by XPS.

Element	C	F	N
fluorographite	40.76	58.76	0.49
fluorographite (control)	43.51	56.03	0.46
PFG-I	61.96	36.14	1.90
PFG-V	82.69	14.50	2.81

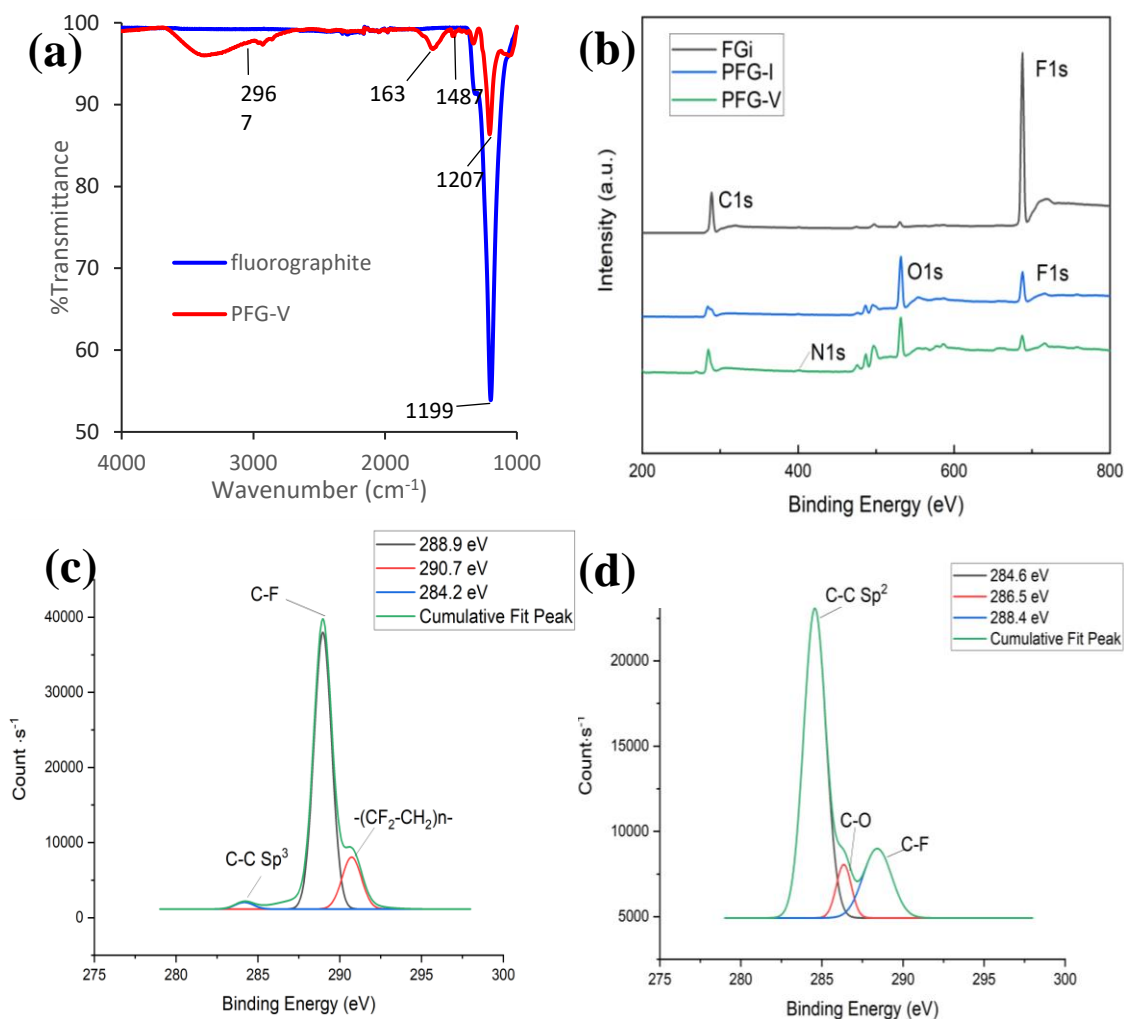


Figure 4.1. (a) ATR FTIR spectra of fluorographite and PFG-V demonstrating defluorination and functionalization of poly(vbTMAC) on fluorographite; (b) XPS survey scan of fluorographite, PFG-I and PFG-V; high resolution C 1s spectra of (c) fluorographite and (d) PFG-V and their deconvolutions results. Presence of adventitious oxygen was exhibited in XPS survey scan of PFG resins. FTIR, XPS survey scans and deconvolutions analysis confirmed defluorination of fluorographite.

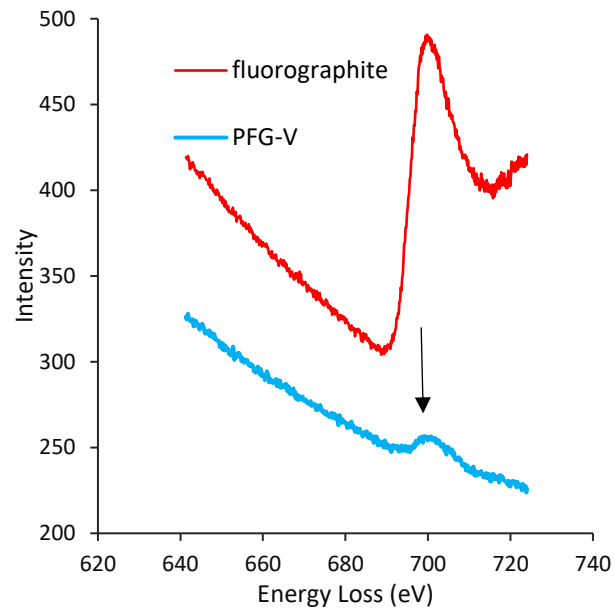


Figure 4.2. Measured EELS spectra showing F-K edge of (a) Fluorographite (b) PFG-V exhibiting characteristic post peak at 700 eV supporting defluorination processes.

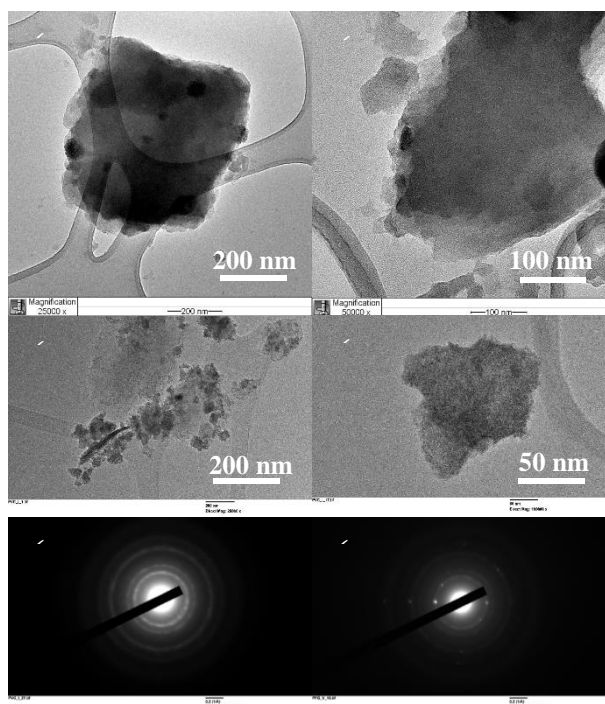


Figure 4.3. Transmission electron micrographs of (a,b) fluorographite sheets (c,d) PFG-I. SAED pattern of (e) PFG-I (f) PFG-V exhibited similar diffraction pattern as presented in XRD analysis. D-spacing calculation is shown in Supplementary Information.

Table 4.2. Crystallite sizes calculated from Raman analysis using the formula  $L(\text{nm}) = (2.4 \times 10^{-10})\lambda \frac{I_D}{I_G}^{-1}$

Sample	$I_D$	$I_G$	L (nm)
Fluorographite	213.4	216.6	19.5
PFG-I	5583.6	5967.9	20.3
PFG-V	10612.9	8113	14.7

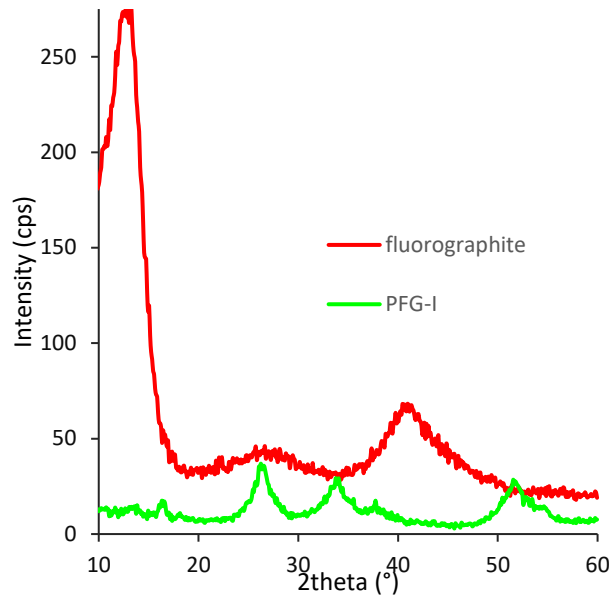


Figure 4.4. XRD patterns of pristine fluorographite and PFG-I.

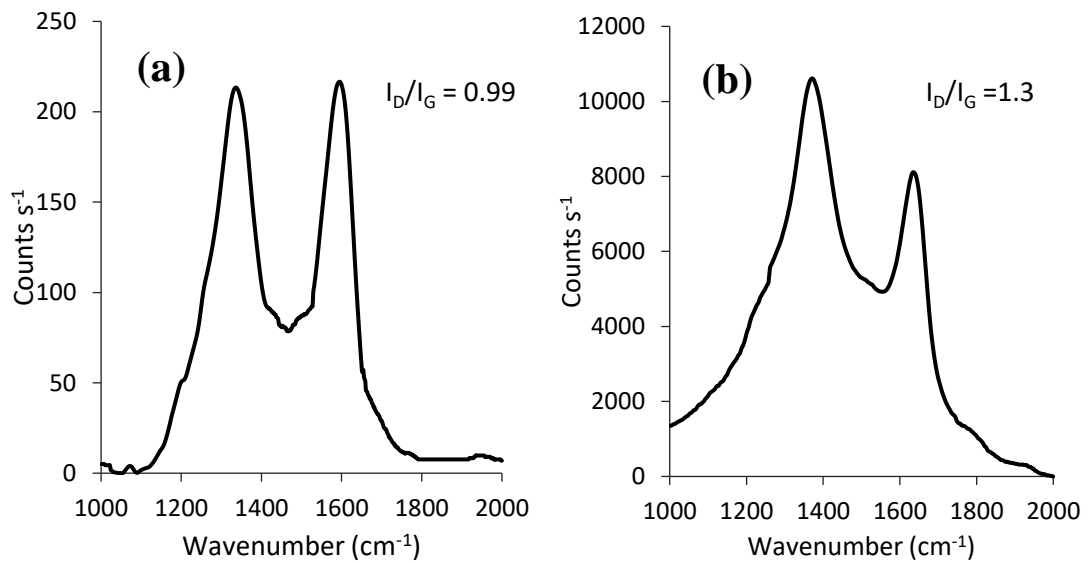


Figure 4.5. Raman spectra of (a) Fluorographite and (b) PFG-V. Crystallite size of the samples,  $L$  was calculated using Raman analysis.

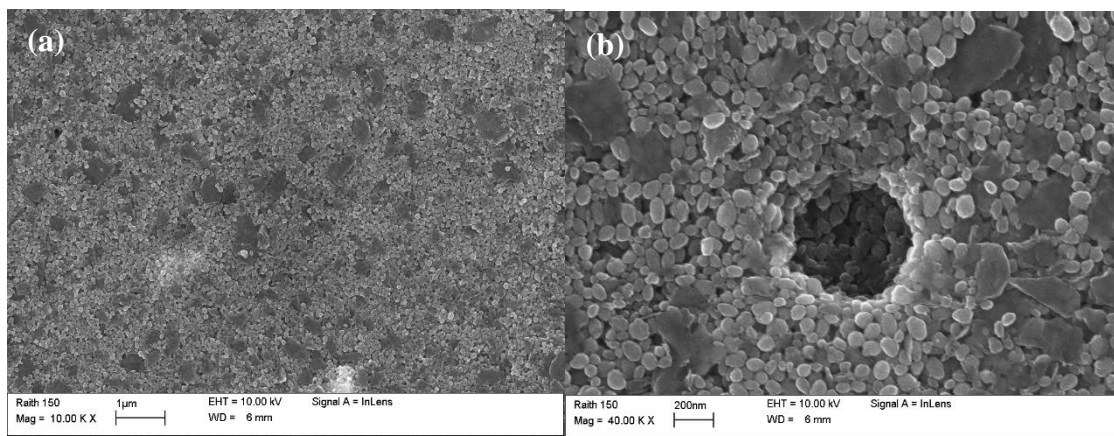


Figure 4.6. Scanning Electron Micrographs of PFG-II thin film revealing plate like morphology.

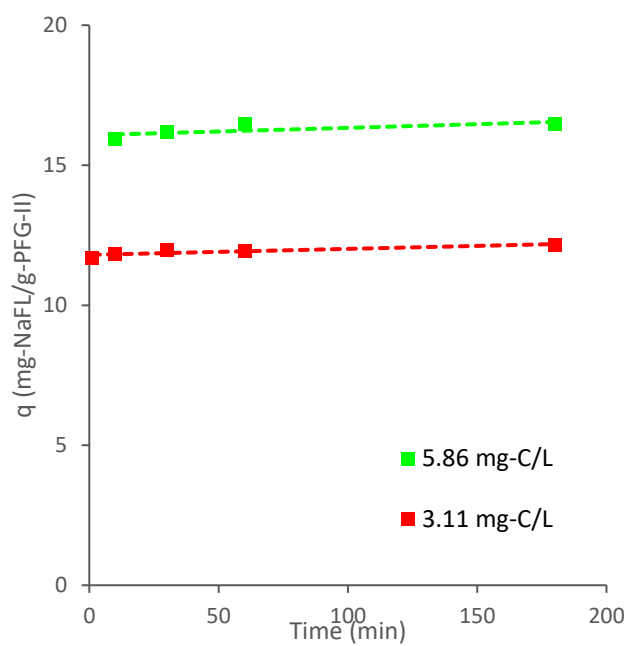


Figure 4.7. Kinetic studies of PFG-II using NaFL as analyte. 3.11 mg-C/L and 5.86 mg-c/L are two initial concentrations of NaFL. Pseudoequilibrium is achieved within few seconds which is characteristic of open resin.

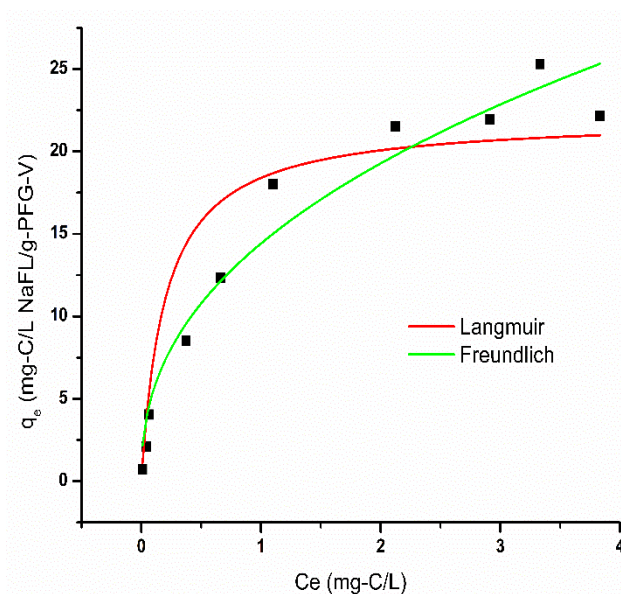


Figure 4.8. Adsorption isotherm of PFG-V. All samples incubated for 4 h. AIC testing supports Freundlich fitting (AIC 21.4) compared to Langmuir fitting (AIC 31.4)

Table 4.3: Water flux measurements of PFG-II thin films deposited on MCE determined at specific pressure. Multiple runs were measured and averaged.

Mass density ( $\text{mg cm}^{-2}$ )	Water flux ( $\text{L h}^{-1}\text{m}^{-2}\text{bar}^{-1}$ )
0.233	$2500 \pm 70$
0.466	$1870 \pm 50$
0.699	$506 \pm 150$

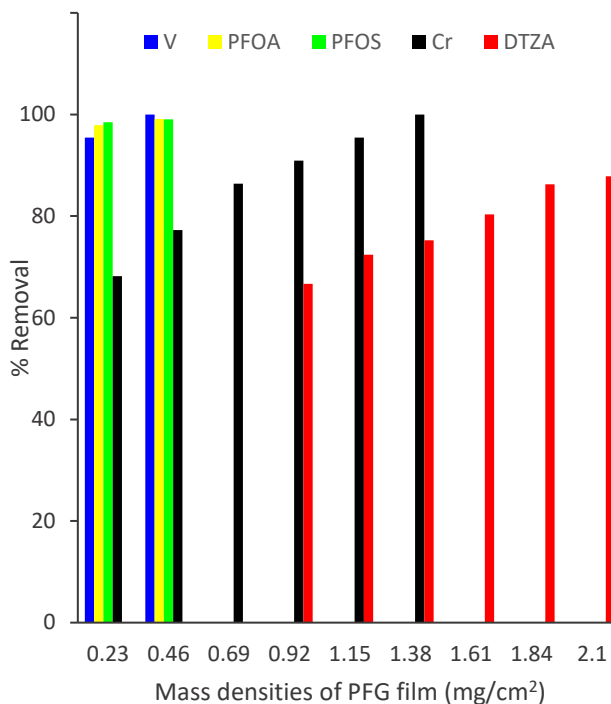


Figure 4.9. Percent removal of emerging contaminants by PFG-I as a function of mass density ( $\text{mg cm}^{-2}$ ) of PFG thin film deposited on MCE membrane (13 mm wide,  $0.2 \mu\text{m}$  pore size). Percent removal was performed using fast filtration. Each bar represents a specific contaminant.

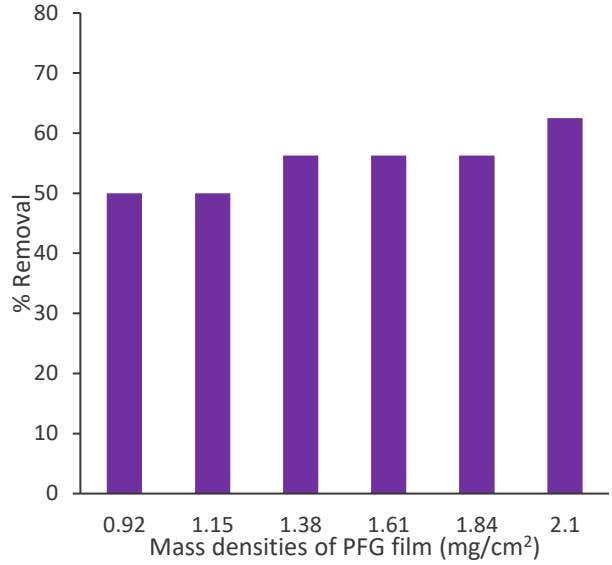


Figure 4.10. Percent removal of  $\text{AsO}_4^{3-}$  /  $\text{OH}^{1-}$  to assess co-selectivity of PFG-II resin in presence of  $\text{OH}^-$  ions. PFG thin film was deposited on MCE membrane (13 mm wide, 0.2  $\mu\text{m}$  pore size).

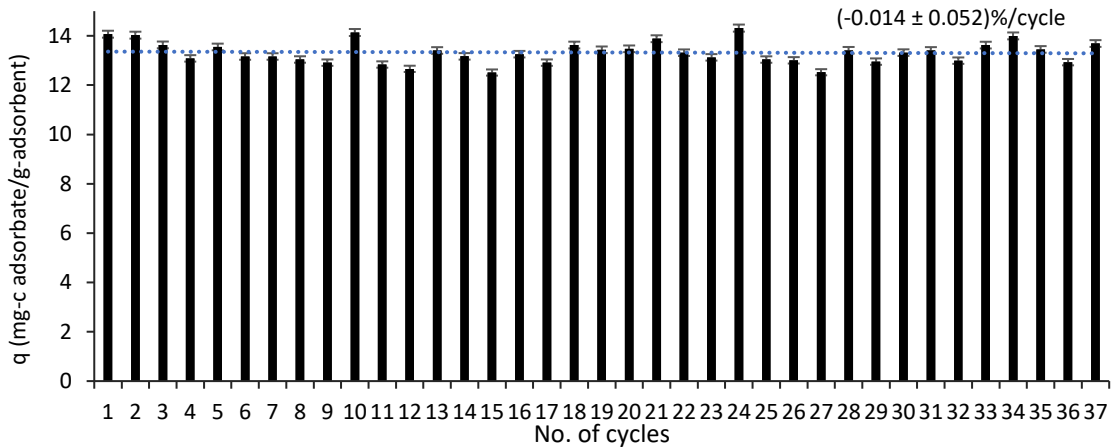


Figure 4.11. Regeneration and reusability studies of PFG-I thin films using NaFL as surrogate. 37 cycles were repeated, and it exhibited 0.014% decrease in  $q$  per cycle.

#### 4.8 Supplementary Figures and tables

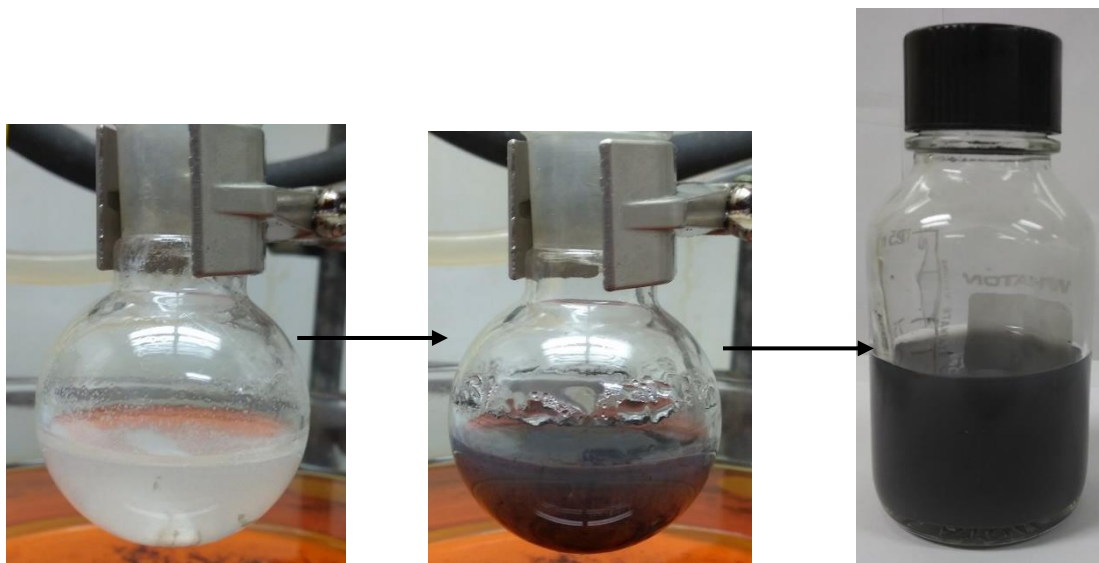


Figure S4.1. Change of color and dispersibility of PFG-V reaction (a) start of the reaction (b) after 3 days (c) purified PFG-V

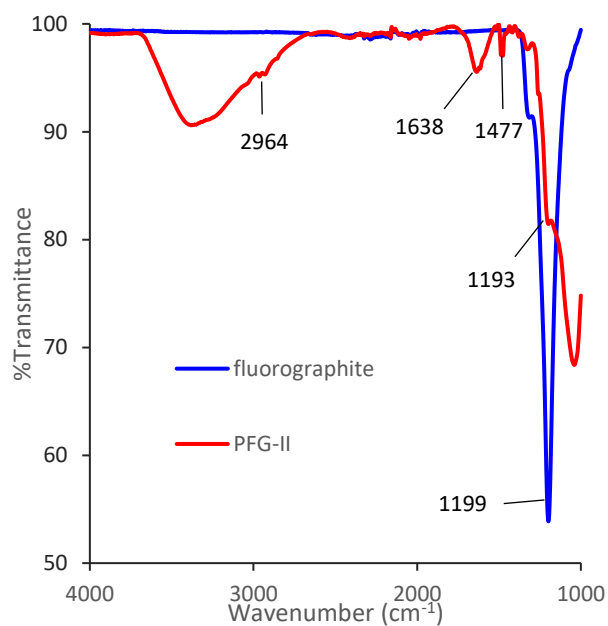


Figure S4.2. ATR FTIR of fluorographite and PFG-II.

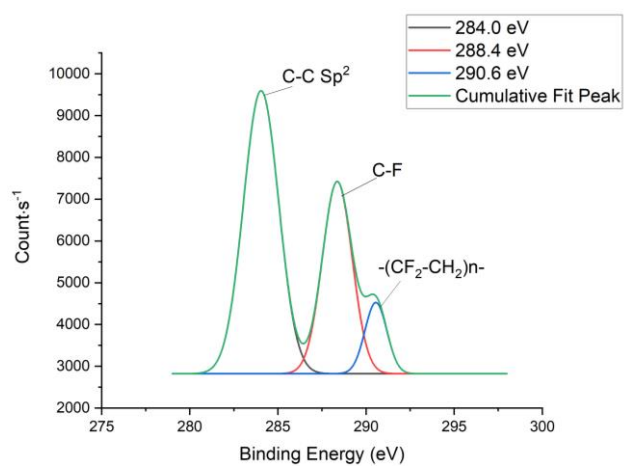


Figure S4.3. High resolution C 1s spectra of PFG-I and its deconvolutions results.

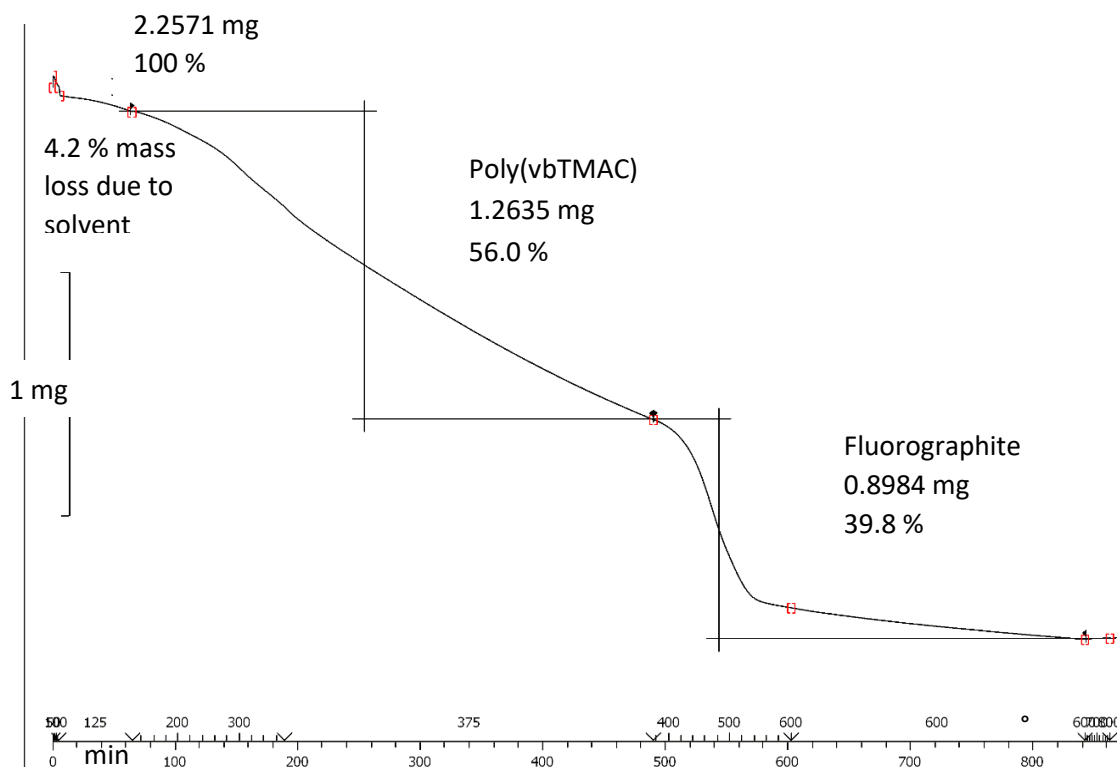


Figure S4.4. TGA thermogram of PFG-V (in air mode)

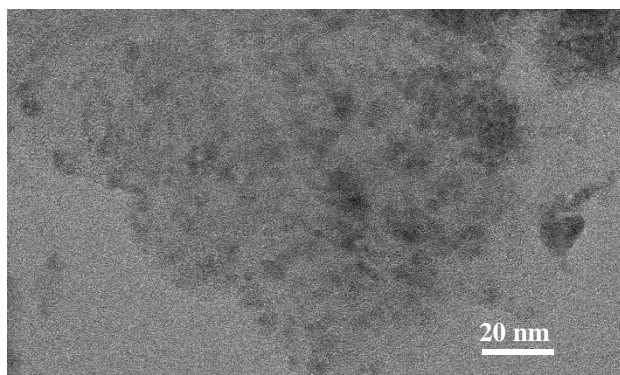


Figure S4.5. Transmission electron micrograph of PFG-V.

Table S4.1. List of d-spacing values calculated by measuring the area of the rings in SAED pattern and finding radius in ImageJ software. d spacing were correlated to hkl Miller indices using the following equation  $d =$

$$\frac{ac}{\sqrt{(al)^2 + \frac{4}{3}c^2(h^2 + hk + k^2)}}$$

where d is d-spacing, a = 2.461 Å and c = 6.708 Å

Samples	d-spacing (Å)			
	PFG-I	3.300	2.618	1.733
PFG-V	3.333	2.577	2.160	1.776

**Sample Name:** JCP-58D-96 30  
**SOP Name:** size SWCNT.sop  
**File Name:** JCP-58D-96.dts  
**Record Number:** 30  
**Material RI:** 1.59  
**Material Absorbtion:** 0.010  
**Dispersant Name:** Water  
**Dispersant RI:** 1.330  
**Viscosity (cP):** 0.8872  
**Measurement Date and Time:** Monday, June 22, 2020 11:49

**Temperature (°C):** 24.9  
**Count Rate (kcps):** 112.2  
**Cell Description:** Low volume disposable sizing cuv...  
**Duration Used (s):** 60  
**Measurement Position (mm):** 4.65  
**Attenuator:** 8

	Size (d.nm):	% Number	Width (d.nm):
<b>Z-Average (d.nm):</b> 226.4	<b>Peak 1:</b> 202.6	100.0	54.92
<b>Pdl:</b> 0.068	<b>Peak 2:</b> 0.000	0.0	0.000
<b>Intercept:</b> 0.949	<b>Peak 3:</b> 0.000	0.0	0.000

**Result quality :** Good

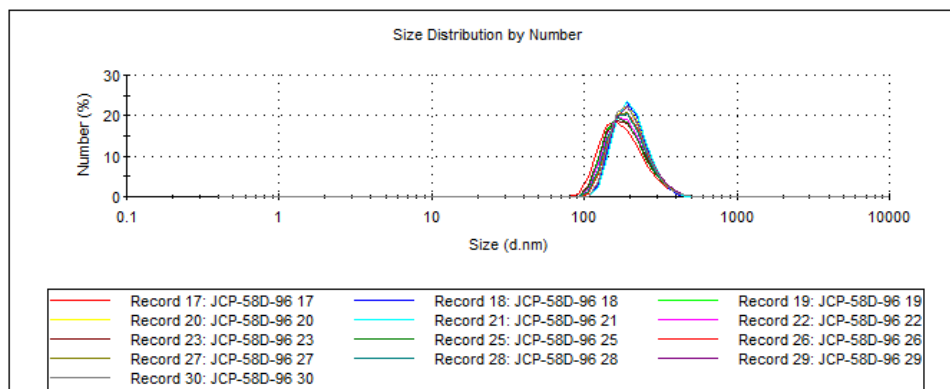


Figure S4.6. Effective hydrodynamic diameter (nm) of PFG-I dispersion. Multiple runs were measured and averaged. All data shown.

**Sample Name:** zeta JCP-58D-96 20  
**SOP Name:** zeta SWCNT.sop  
**File Name:** JCP-58D-96.dts  
**Record Number:** 75  
**Date and Time:** Monday, June 22, 2020 1:08:16 PM

**Dispersant Name:** Water  
**Dispersant RI:** 1.330  
**Viscosity (cP):** 0.8872  
**Dispersant Dielectric Constant:** 78.5

**Temperature (°C):** 25.0  
**Count Rate (kcps):** 203.5  
**Cell Description:** Clear disposable zeta cell

**Zeta Runs:** 12  
**Measurement Position (mm):** 2.00  
**Attenuator:** 8

	Mean (mV)	Area (%)	Width (mV)
<b>Zeta Potential (mV):</b> 46.6	<b>Peak 1:</b> 46.6	100.0	6.06
<b>Zeta Deviation (mV):</b> 6.06	<b>Peak 2:</b> 0.00	0.0	0.00
<b>Conductivity (mS/cm):</b> 0.0289	<b>Peak 3:</b> 0.00	0.0	0.00

**Result quality :** Good

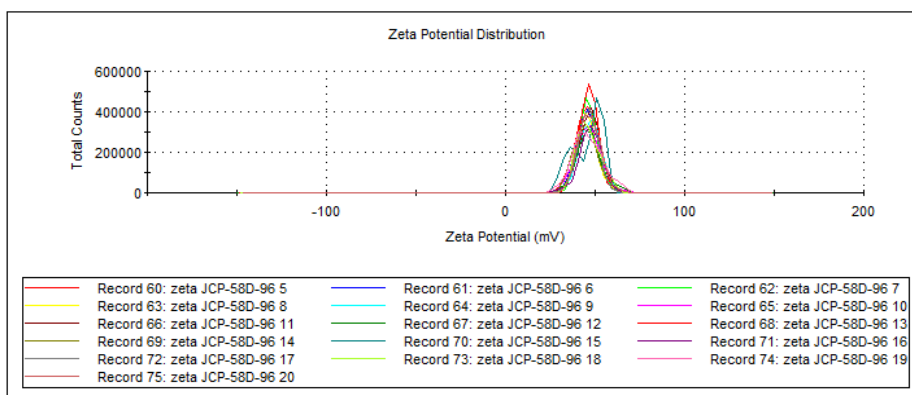


Figure S4.7. Zeta potential (mV) of PFG-I dispersion. Multiple runs were measured and averaged. All data shown.

**Sample Name:** size JCP-58D-103 30  
**SOP Name:** size SWCNT.sop  
**File Name:** JCP-58D-103.dts  
**Record Number:** 30  
**Material RI:** 1.59  
**Material Absorbtion:** 0.010  
**Dispersant Name:** Water  
**Dispersant RI:** 1.330  
**Viscosity (cP):** 0.8872  
**Measurement Date and Time:** Monday, July 13, 2020 11:09:

**Temperature (°C):** 25.0  
**Count Rate (kcps):** 147.9  
**Cell Description:** Low volume disposable sizing cuv...  
**Duration Used (s):** 70  
**Measurement Position (mm):** 4.65  
**Attenuator:** 9

	Size (d.nm):	% Number	Width (d.nm):
<b>Z-Average (d.nm):</b> 235.4	<b>Peak 1:</b> 181.5	100.0	48.98
<b>Pdl:</b> 0.240	<b>Peak 2:</b> 0.000	0.0	0.000
<b>Intercept:</b> 0.955	<b>Peak 3:</b> 0.000	0.0	0.000

**Result quality :** Good

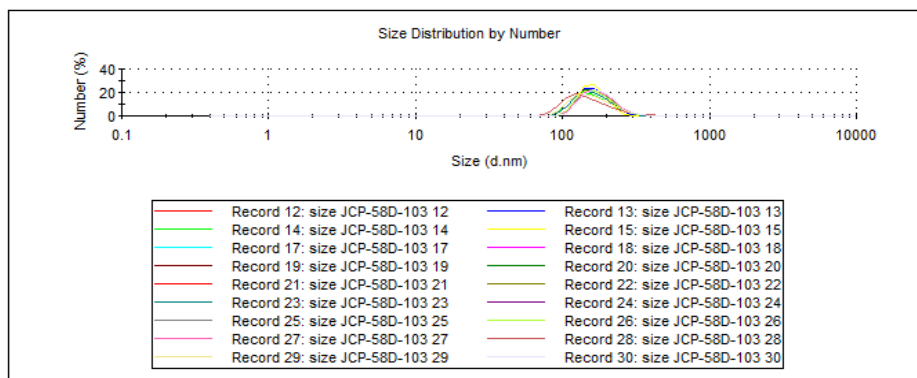


Figure S4.8. Effective hydrodynamic diameter (nm) of PFG-V dispersion. Multiple runs were measured and averaged. All data shown.

Sample Name: zeta JCP-58D-103 40

SOP Name: zeta SWCNT.sop

File Name: JCP-58D-103.dts

Record Number: 70

Date and Time: Monday, July 13, 2020 11:45:33 AM

Dispersant Name: Water

Dispersant RI: 1.330

Viscosity (cP): 0.8872

Dispersant Dielectric Constant: 78.5

Temperature (°C): 25.0

Count Rate (kcps): 40.0

Cell Description: Clear disposable zeta cell

Zeta Runs: 12

Measurement Position (mm): 2.00

Attenuator: 7

	Mean (mV)	Area (%)	Width (mV)
Zeta Potential (mV): 46.0	Peak 1: 46.0	100.0	7.48
Zeta Deviation (mV): 7.48	Peak 2: 0.00	0.0	0.00
Conductivity (mS/cm): 0.0213	Peak 3: 0.00	0.0	0.00

Result quality : **Good**

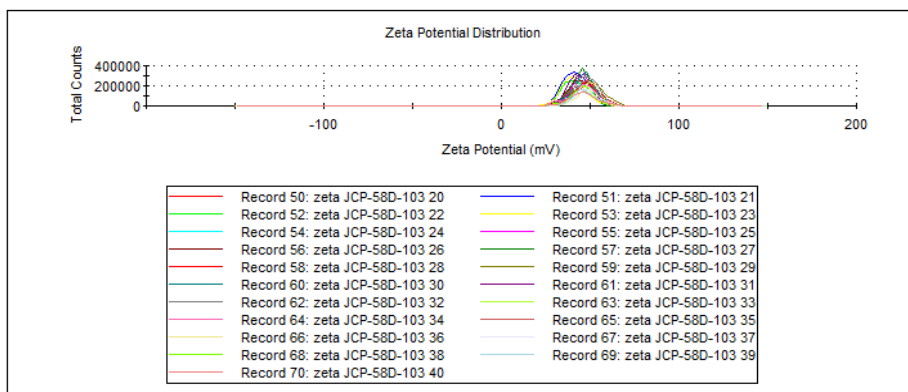


Figure S4.9. Effective zeta potential (mV) of PFG-V dispersion. Multiple runs were measured and averaged. All data shown.

Table S4.2. Hydrodynamic diameter (nm) and zeta potential (mV) measured using DLS.

Batch #	PFG-I	PFG-II	PFG-III	PFG-IV	PFG-V
Hydrodynamic diameter (nm)	192 ± 8	171 ± 2	167 ± 7	116 ± 2	176 ± 2
Zeta potential (mV)	+46.4 ± 0.5	+49.2 ± 1.7	+45.3 ± 1.2	+46.2 ± 0.9	+47.2 ± 0.9

Table S4.3: Water flux measurements of PFG-IV thin films deposited on MCE determined at specific pressure. Multiple runs were measured and averaged.

Mass density (mg cm <sup>-2</sup> )	Water flux (L h <sup>-1</sup> m <sup>-2</sup> bar <sup>-1</sup> )
0.233	7069 ± 1
0.466	1925 ± 3
0.699	1173 ± 12

Table S4.4: Parameters derived from Langmuir and Freundlich fitted models of NaFL binding isotherm to PFG-V

Analyte	Langmuir			Freundlich		
	$K_L$ ( $M^{-1}$ )	$Q_M$ (mg/g)	R	$K_f$ (mg/g)(L/mg) <sup>1/n</sup>	n	R
NaFL	$5 \pm 2.6$	$22.1 \pm 2.0$	0.875	$14.4 \pm 0.8$	$2.4 \pm 0.2$	0.955

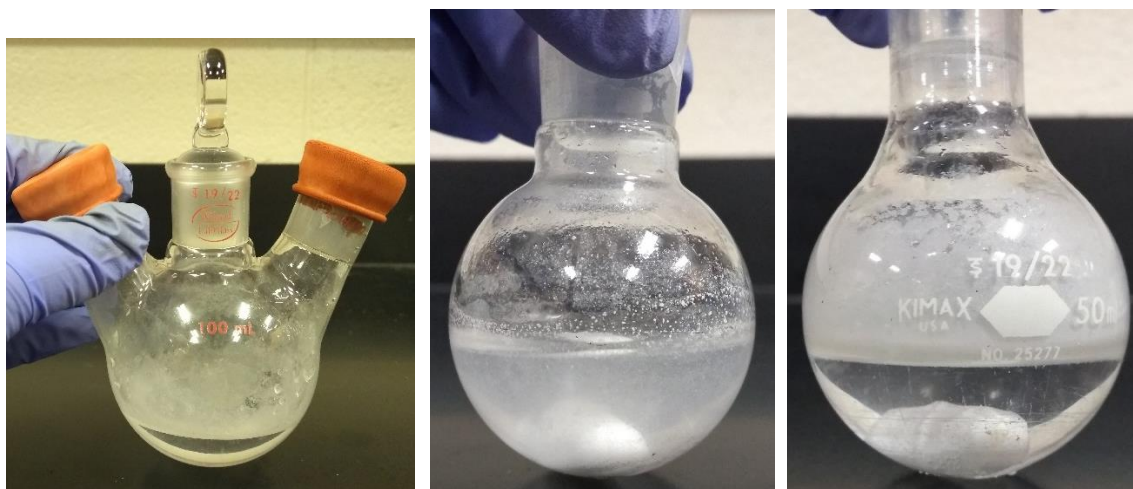


Figure S4.10: Different batches of controlled experiments in cold bath (a) FGI in water after 2 h sonication at  $90 W cm^{-2}$  for 2 h (b) FGI and PEG in water (c) FGI in water stirred for 3 days.



Figure S4.11: Different batches of controlled experiments in reflux (a) FGi in water (b) FGi and PEG in water under reflux for 3 days

Table S4.5. Overview of reagents/processes involved in different batches of PFGs.

Reagents	PFG-I	PFG-II	PFG-III	PFG-IV	PFG-V
<b>TEMPO</b>	+	-	-	-	-
<b>Catalyst/ligand complex</b>	+	+	+	- (<5 ppm)	- (<5 ppm)
<b>Reducing agent</b>	+	+	-	-	-
<b>ultrasonication</b>	+	+	+	+	-
<b>reflux</b>	+	+	+	+	+
<b>Time duration (3 days)</b>	+	+	+	+	+

## OVERALL CONCLUSION

Materials at extremely small scales have high specific surface area. The high specific surface area provides the accessibility of large numbers of exposed active sites for targeted interaction. This leads to increase in effectivity of adsorption per mass of raw material when nanomaterials are used as a scaffold compared to bulk materials in water purification systems. Also, the fabrication of nanocomposites should be designed in such a way that it ensures contact-based removal of contaminants compared to diffusion-based removal since contact-based removal will lead to faster sorption kinetics. Since, effectivity per mass of raw material is high for nanomaterials, high capacity water purification is possible with thin film assembly that can intrinsically support high water flux. Thus, implementation of nanocomposites in water purification systems will lead to fast, efficient and affordable solutions in comparison to their bulk parts.

This dissertation is focused on sustainable synthesis of nanocomposites in the form of nano assisted ion exchange systems employed for facile and high capacity water purification. This research study also incorporates green chemistry for the synthesis and functionalization of anion exchange resin polyelectrolytes onto carbon nanostructures. In addition to the study of nanoscale materials, this dissertation study explored the synergistic role of sonochemistry in mediating radical polymerization and functionalization onto carbon nanostructures. The behavior of polymerization and functionalization was extensively explored in presence and absence of hydroxyl radicals generated by sonolysis of water. Short strand brushes of polyelectrolyte were functionalized onto SWCNT in an all-aqueous environment using modified ARGET

ATRP conditions, eliminating the usage of any organic solvent. ARGET ATRP is a robust process for chain initiation, propagation, and chain-end functionalization. When ATRP is combined with sonochemistry, they work synergistically supporting chain initiation, growth and functionalization without addition of initiators, reducing agents, and at low catalyst/ligand complex concentration occurring effectively at low temperatures. Kinetics and length of these polymers were compared to conventional ARGET ATRP synthesized polyelectrolytes where both the types exhibited semilogarithmic behavior with respect to monomer concentration. Apparent activation energy of poly(vbTMAC) for radical initiation and propagation in presence and absence of ultrasonication exhibited similar trend as published in literature.

Adhering to green chemistry principles, we explored a graphitic derivative that exhibits facile surface functionalization. Fluorographene is a green alternative to 2D materials that requiring nothing but an electron rich surface-functionalizing agent (in our case, it is the living end of the poly(vbTMAC) chain end). The result is a facile method for surface modification, defluorination and surface functionalization of graphemic nanostructured carbon in water! This leads to a less energy-intensive green processes that can be used to formulate materials for sustainable applications like water purification. This work explored the physiochemical characterization of PFG to understand the bonding, crystal spacing and substantiate the defluorination and functionalization of 2D structure of graphite. Future work includes optimization of degree of defluorination and functionalization of polyelectrolytes on these semi-defluorinated 2D scaffolds and incorporation of these materials in breakthrough systems to understand the structural robustness.

Functionalization of SWCNT in water is facile and has a direct correlation to duration of reflux. Aq-SNR, when fabricated as thin films, exhibited mesoporous pin hole free wide pores mesh properties that support high water flux of large volumes of analytes and high loading capacity maintaining scaffold robustness and defect tolerance through breakthrough studies. Shorter strands functionalized Aq-SNR exhibited prolonged breakthrough compared to longer strands functionalized Aq-SNR due to the ease of contaminant finding binding site in short strands environment compared to longer strands which was corroborated with molecular mechanics studies.

Defluorination and functionalization of fluorographite in water is a novel process developed to emphasize green chemistry synthesis and eliminate use of caustic/toxic reagents. PFG resins work along the same lines of faster kinetics similar to Aq-SNR while Aq-SNR exhibit higher binding capacity due to easy tailoring of higher functionalization in Aq-SNR. PFG resins, when fabricated as a thin film, exhibited plate-like grains of functionalized graphitic crystals. These particles demonstrate high flux yet high adsorption due to tortuous path length for molecules that enables adsorption at environmentally relevant concentrations. When resolved using TEM, the exfoliated functionalized regions become evident on individual PFG resins.

As both of these materials demonstrate open resin structure, they are easily regenerated and reused, which enables sustainable manufacturing and environmental stewardship. I have also worked on biodegradable cellulose nanofibers which are an excellent candidate for surface functionalization and advocacy of green chemistry. Hence, the objective of meeting the standards of green synthesis is met and this work

establishes synthesis of analogues that open new avenues for fabrication of smart point-of-use water purification systems.

## Future Prospects

My dissertation is based on fundamental studies of tailoring cost-effective nanomaterials for sustainable applications like water purification. I have developed these nanomaterials and methods using a green processability approach so that they do not incur a toxic payload to the environment. Since we are focusing on removal of small hydrophilic molecules and metal ions, we need nanocomposite thin films that support high water flux and high percentage removal of contaminants. It is fundamentally important to compare how various nanostructured materials will respond to intrinsic parameters like degree of functionalization, water flux and percent removal parameters that will help in designing the required pretotype for thin film water purification systems.

The three projects I described in my dissertation are just the first steps along the way to a longer view vision of this water purification goal, encompassing many other avenues of research. For example, the nanostructured carbon materials are conductive, and like carbon nanotubes can also be used as sensor systems. Similar to CNTs, graphene nanoribbons are quasi one-dimensional structures that exhibit selective high reactivity at the edge.<sup>1</sup> This would modify the band structure of graphene ribbons<sup>2</sup> and provide specificity to certain chemicals for sensing application. For example, functionalizing with F moieties at edge sites can make the scaffold fluorophilic for PFAS like contaminants. However, graphene nanoribbons are expensive (\$600/g) like CNTs.

Since we are striving to build smart nanofiltration systems that are inexpensive (<\$1/g), use of biopolymers (like cellulose and chitosan) will be affordable solutions. I have also worked on cellulose materials where we surface modified the C6 of sugar units along the cellulose chain with COO- groups and later, formed stable amide linkages with

allyl amine that provided accessible vinylic groups required for poly(vbTMAC) attack and functionalization. All the reactions resulting in poly(vbTMAC) functionalization were done in water. Chitosan has primary amine group on the C2 of every carbohydrate unit. These are favorable sites for linkers to connect poly(vbTMAC) functionalized carbon nanodiamonds or carbon nanodots, or chelating agents and form flowers on a stem morphology comprising of two or more nanostructures. It should be possible to replace chitosan with a sheet scaffold like graphitic carbon nitride and form same functionalization. It will be interesting to compare the water flux and percent removal of these thin film assemblies to sticks (CNT) and sheets (graphene) assemblies. It will be possible to perform all these approaches in water using environmentally benign reagents.

Rational design of these nanostructured materials must be carefully calculated to incorporate facile techniques, low cost and environmentally benign raw materials so that it can be used for large scale production of smart water purification systems. My dissertation targeted the applicability of all the aforementioned parameters and opens new avenues for many sustainable applications like water purifications, sensors and air purification that can be explored in near future.

## References

1. Panighel, M.; Quiroga, S.; Brandimarte, P.; Moreno, C.; Garcia-Lekue, A.; Vilas-Varela, M.; Rey, D.; Sauthier, G.; Ceballos, G., Peña, D. Stabilizing Edge Fluorination in Graphene Nanoribbons. *ACS Nano*. **2020**, *14* (9), 11120-11129
2. Wagner, P.; Ewels, C. P.; Adjizian, J.-J.; Magaud, L.; Pochet, P.; Roche, S.; Lopez-Bezanilla, A.; Ivanovskaya, V. V.; Yaya, A., Rayson, M. Band gap engineering via edge-functionalization of graphene nanoribbons. *The Journal of Physical Chemistry C*. **2013**, *117* (50), 26790-26796

## Introduction References:

1. Shannon, M. A.; Bohn, P. W.; Elimelech, M.; Georgiadis, J. G.; Marinas, B. J., Mayes, A. M. Science and technology for water purification in the coming decades. *Nanoscience and technology: a collection of reviews from nature Journals*: World Scientific; **2010**:337-346.
2. USEPA. Announcement of Small System Compliance Technology Lists for Existing National Primary Drinking Water Regulations and Findings Concerning Variance Technologies. 1998; <https://archive.epa.gov/water/archive/web/html/clistfrn.html>.
3. Weidner, E., Ciesielczyk, F. Removal of Hazardous Oxyanions from the Environment Using Metal-Oxide-Based Materials. *Materials*. **2019**, *12* (6), 32 10.3390/ma12060927
4. USEPA. "2018 Edition of the Drinking Water Standards and Health Advisories Tables". **2018**. <https://www.epa.gov/sites/production/files/2018-03/documents/dwtable2018.pdf>.
5. Yang, A. N.; Ching, C. S.; Easier, M.; Helbling, D. E., Dichtel, W. R. Cyclodextrin Polymers with Nitrogen-Containing Tripodal Crosslinkers for Efficient PFAS Adsorption. *ACS Mater Lett*. **2020**, *2* (9), 1240-1245 10.1021/acsmaterialslett.0c00240
6. Shetty, D.; Jahovic, I.; Skorjanc, T.; Erkal, T. S.; Ali, L.; Raya, J.; Asfari, Z.; Olson, M. A.; Kirmizialtin, S., Yazaydin, A. O. Rapid and Efficient Removal of Perfluorooctanoic Acid from Water with Fluorine-Rich Calixarene-Based Porous Polymers. *ACS Appl Mater Interfaces*. **2020**
7. Siraj, K. T., Rao, P. P. Review on current world water resources scenario and water treatment technologies and techniques. *IJAR*. **2016**, *2* (4), 262-266
8. Qu, X. L.; Brame, J.; Li, Q. L., Alvarez, P. J. J. Nanotechnology for a Safe and Sustainable Water Supply: Enabling Integrated Water Treatment and Reuse. *Accounts Chem Res*. **2013**, *46* (3), 834-843 10.1021/ar300029v
9. Organization, W. H. Pharmaceuticals in drinking-water. **2012**
10. Matsui, Y.; Knappe, D. R. U., Takagi, R. Pesticide adsorption by granular activated carbon adsorbers. 1. Effect of natural organic matter preloading on removal rates and model simplification. *Environ Sci Technol*. **2002**, *36* (15), 3426-3431 10.1021/es0113652

11. Matsui, Y.; Fukuda, Y.; Inoue, T., Matsushita, T. Effect of natural organic matter on powdered activated carbon adsorption of trace contaminants: characteristics and mechanism of competitive adsorption. *Water Res.* **2003**, *37* (18), 4413-4424 10.1016/s0043-1354(03)00423-8
12. Kothawala, D. N.; Kohler, S. J.; Ostlund, A.; Wiberg, K., Ahrens, L. Influence of dissolved organic matter concentration and composition on the removal efficiency of perfluoroalkyl substances (PFASs) during drinking water treatment. *Water Res.* **2017**, *121*, 320-328 10.1016/j.watres.2017.05.047
13. Sabio, E.; Gonzalez, E.; Gonzalez, J. F.; Gonzalez-Garcia, C. M.; Ramiro, A., Ganan, J. Thermal regeneration of activated carbon saturated with p-nitrophenol. *Carbon.* **2004**, *42* (11), 2285-2293 10.1016/j.carbon.2004.05.007
14. Johnson, B. R.; Eldred, T. B.; Nguyen, A. T.; Payne, W. M.; Schmidt, E. E.; Alansari, A. Y.; Amburgey, J. E., Poler, J. C. High-Capacity and Rapid Removal of Refractory NOM Using Nanoscale Anion Exchange Resin. *ACS Appl Mater Interfaces.* **2016**, *8* (28), 18540-18549 10.1021/acsami.6b04368
15. Li, R.; Zhang, L., Wang, P. Rational design of nanomaterials for water treatment. *Nanoscale.* **2015**, *7* (41), 17167-17194
16. Nnamchi, P. S., Obayi, C. S. Electrochemical Characterization of Nanomaterials. *Characterization of Nanomaterials*: Elsevier; **2018**:103-127.
17. Santhosh, C.; Velmurugan, V.; Jacob, G.; Jeong, S. K.; Grace, A. N., Bhatnagar, A. Role of nanomaterials in water treatment applications: A review. *Chem Eng J.* **2016**, *306*, 1116-1137 10.1016/j.cej.2016.08.053
18. Adeleye, A. S.; Conway, J. R.; Garner, K.; Huang, Y. X.; Su, Y. M., Keller, A. A. Engineered nanomaterials for water treatment and remediation: Costs, benefits, and applicability. *Chem Eng J.* **2016**, *286*, 640-662 10.1016/j.cej.2015.10.105
19. Simakova, A.; Averick, S. E.; Konkolewicz, D., Matyjaszewski, K. Aqueous ARGET ATRP. *Macromolecules.* **2012**, *45* (16), 6371-6379 10.1021/ma301303b
20. Fantin, M.; Isse, A. A.; Matyjaszewski, K., Gennaro, A. ATRP in Water: Kinetic Analysis of Active and Super-Active Catalysts for Enhanced Polymerization Control. *Macromolecules.* **2017**, *50* (7), 2696-2705 10.1021/acs.macromol.7b00246
21. Min, K.; Gao, H., Matyjaszewski, K. Use of Ascorbic Acid as Reducing Agent for Synthesis of Well-Defined Polymers by ARGET ATRP. *Macromolecules.* **2007**, *40* (6), 1789-1791 10.1021/ma0702041

22. Fantin, M.; Isse, A. A.; Gennaro, A., Matyjaszewski, K. Understanding the Fundamentals of Aqueous ATRP and Defining Conditions for Better Control. *Macromolecules*. **2015**, *48* (19), 6862-6875 10.1021/acs.macromol.5b01454
23. Werner, A.; Schmitt, V.; Sebe, G., Heroguez, V. Convenient Synthesis of Hybrid Polymer Materials by AGET-ATRP Polymerization of Pickering Emulsions Stabilized by Cellulose Nanocrystals Grafted with Reactive Moieties. *Biomacromolecules*. **2019**, *20* (1), 490-501 10.1021/acs.biomac.8b01482
24. Matyjaszewski, K., Xia, J. H. Atom transfer radical polymerization. *Chemical Reviews*. **2001**, *101* (9), 2921-2990 10.1021/cr940534g
25. Matyjaszewski, K., Tsarevsky, N. V. Nanostructured functional materials prepared by atom transfer radical polymerization. *Nat Chem*. **2009**, *1* (4), 276-288
26. Min, K.; Gao, H. F., Matyjaszewski, K. Use of ascorbic acid as reducing agent for synthesis of well-defined polymers by ARGET ATRP. *Macromolecules*. **2007**, *40* (6), 1789-1791 10.1021/ma0702041
27. Jakubowski, W.; Min, K., Matyjaszewski, K. Activators regenerated by electron transfer for atom transfer radical polymerization of styrene. *Macromolecules*. **2006**, *39* (1), 39-45 10.1021/ma0522716
28. Li, C. J., Trost, B. M. Green chemistry for chemical synthesis. *Proc Natl Acad Sci U S A*. **2008**, *105* (36), 13197-13202 10.1073/pnas.0804348105
29. Sahu, A.; Blackburn, K.; Durkin, K.; Eldred, T. B.; Johnson, B. R.; Sheikh, R.; Amburgey, J. E., Poler, J. C. Green synthesis of nanoscale anion exchange resin for sustainable water purification. *Environ Sci-Wat Res Technol*. **2018**, *4* (10), 1685-1694 10.1039/c8ew00593a
30. Wang, Z. H.; Wang, Z. H.; Pan, X. C.; Fu, L. Y.; Lathwal, S.; Olszewski, M.; Yan, J. J.; Enciso, A. E.; Wang, Z. Y.; Xia, H. S., Matyjaszewski, K. Ultrasonication-Induced Aqueous Atom Transfer Radical Polymerization. *ACS Macro Lett*. **2018**, *7* (3), 275-280 10.1021/acsmacrolett.8b00027
31. Sahu, A.; Sheikh, R., Poler, J. C. Green sonochemical synthesis, kinetics and functionalization of nanoscale anion exchange resins and their performance as water purification membranes. *Ultrason Sonochem*. **2020**, *67*, 10 10.1016/j.ultsonch.2020.105163
32. Rokita, B.; Rosiak, J. M., Ulanski, P. Ultrasound-Induced Cross-Linking and Formation of Macroscopic Covalent Hydrogels in Aqueous Polymer and Monomer Solutions. *Macromolecules*. **2009**, *42* (9), 3269-3274 10.1021/ma802565p

33. Bradley, M., Grieser, F. Emulsion polymerization synthesis of cationic polymer latex in an ultrasonic field. *J Colloid Interface Sci.* **2002**, *251* (1), 78-84  
10.1006/jcis.2002.8383
34. Nine, M. J.; Cole, M. A.; Tran, D. N. H., Losic, D. Graphene: a multipurpose material for protective coatings. *J Mater Chem A.* **2015**, *3* (24), 12580-12602  
10.1039/c5ta01010a
35. Hummers, W. S., Offeman, R. E. PREPARATION OF GRAPHITIC OXIDE. *J Am Chem Soc.* **1958**, *80* (6), 1339-1339 10.1021/ja01539a017
36. Furst, A.; Berlo, R. C., Hooton, S. HYDRAZINE AS A REDUCING AGENT FOR ORGANIC COMPOUNDS ( CATALYTIC HYDRAZINE REDUCTIONS. *Chemical Reviews.* **1965**, *65* (1), 51-& 10.1021/cr60233a002
37. Yang, Z. Q.; Sun, W.; Wang, L. D.; Li, S. J.; Zhu, T. Z., Liu, G. C. Liquid-phase exfoliated fluorographene as a two dimensional coating filler for enhanced corrosion protection performance. *Corrosion Science.* **2016**, *103*, 312-318  
10.1016/j.corsci.2015.10.039
38. Huang, W. X.; Pei, Q. X.; Liu, Z. S., Zhang, Y. W. Thermal conductivity of fluorinated graphene: A non-equilibrium molecular dynamics study. *Chem Phys Lett.* **2012**, *552*, 97-101 10.1016/j.cplett.2012.09.043
39. Bulusheva, L. G.; Tur, V. A.; Fedorovskaya, E. O.; Asanov, I. P.; Pontiroli, D.; Ricco, M., Okotrub, A. V. Structure and supercapacitor performance of graphene materials obtained from brominated and fluorinated graphites. *Carbon.* **2014**, *78*, 137-146 10.1016/j.carbon.2014.06.061
40. Urbanova, V.; Karlicky, F.; Matej, A.; Sembera, F.; Janousek, Z.; Perman, J. A.; Ranc, V.; Cepe, K.; Michl, J.; Otyepka, M., Zboril, R. Fluorinated graphenes as advanced biosensors - effect of fluorine coverage on electron transfer properties and adsorption of biomolecules. *Nanoscale.* **2016**, *8* (24), 12134-12142  
10.1039/c6nr00353b
41. Das, S.; Sudhagar, P.; Verma, V.; Song, D.; Ito, E.; Lee, S. Y.; Kang, Y. S., Choi, W. Amplifying Charge-Transfer Characteristics of Graphene for Triiodide Reduction in Dye-Sensitized Solar Cells. *Advanced Functional Materials.* **2011**, *21* (19), 3729-3736 10.1002/adfm.201101191
42. Zhu, M. S.; Xie, X. D.; Guo, Y. L.; Chen, P. L.; Ou, X. W.; Yu, G., Liu, M. H. Fluorographene nanosheets with broad solvent dispersibility and their applications as a modified layer in organic field-effect transistors. *Physical Chemistry Chemical Physics.* **2013**, *15* (48), 20992-21000 10.1039/c3cp53383b

43. Ho, K. I.; Huang, C. H.; Liao, J. H.; Zhang, W. J.; Li, L. J.; Lai, C. S., Su, C. Y. Fluorinated Graphene as High Performance Dielectric Materials and the Applications for Graphene Nanoelectronics. *Sci Rep.* **2014**, *4*, 10.1038/srep05893
44. Dubecky, M.; Otyepkova, E.; Lazar, P.; Karlicky, F.; Petr, M.; Cepe, K.; Banas, P.; Zboril, R., Otyepka, M. Reactivity of Fluorographene: A Facile Way toward Graphene Derivatives. *J Phys Chem Lett.* **2015**, *6* (8), 1430-1434 10.1021/acs.jpcelett.5b00565
45. Medved, M.; Zoppellaro, G.; Ugolotti, J.; Matochova, D.; Lazar, P.; Pospisil, T.; Bakandritsos, A.; Tucek, J.; Zboril, R., Otyepka, M. Reactivity of fluorographene is triggered by point defects: beyond the perfect 2D world. *Nanoscale.* **2018**, *10* (10), 4696-4707 10.1039/c7nr09426d
46. Lai, W. C.; Xu, D. Z.; Wang, X.; Wang, Z. M.; Liu, Y.; Zhang, X. J.; Li, Y. L., Liu, X. Y. Defluorination and covalent grafting of fluorinated graphene with TEMPO in a radical mechanism. *Phys Chem Chem Phys.* **2017**, *19* (35), 24076-24081 10.1039/c7cp04439a
47. Chronopoulos, D. D.; Bakandritsos, A.; Pykal, M.; Zbořil, R., Otyepka, M. Chemistry, properties, and applications of fluorographene. *Applied materials today.* **2017**, *9*, 60-70
48. Kouloumpis, A.; Chronopoulos, D. D.; Potsi, G.; Pykal, M.; Vlcek, J.; Scheibe, M., Otyepka, M. One-Step Synthesis of Janus Fluorographene Derivatives. *Chem-Eur J.* **2020**, *26* (29), 6518-6524 10.1002/chem.201905866
49. Baumgartner, R., McNeill, K. Hydrodefluorination and hydrogenation of fluorobenzene under mild aqueous conditions. *Environmental science & technology.* **2012**, *46* (18), 10199-10205
50. Baker, R. W. *Membrane technology and applications.* John Wiley & Sons; **2012**.
51. Jang, D.; Idrobo, J. C.; Laoui, T., Karnik, R. Water and Solute Transport Governed by Tunable Pore Size Distributions in Nanoporous Graphene Membranes. *ACS Nano.* **2017**, *11* (10), 10042-10052 10.1021/acsnano.7b04299
52. He, J. B.; Lin, X. M.; Chan, H.; Vukovic, L.; Kral, P., Jaeger, H. M. Diffusion and Filtration Properties of Self-Assembled Gold Nanocrystal Membranes. *Nano Letters.* **2011**, *11* (6), 2430-2435 10.1021/nl200841a
53. Bosch-Navarro, C.; Walker, M.; Wilson, N. R., Rourke, J. P. Covalent modification of exfoliated fluorographite with nitrogen functionalities. *Journal of Materials Chemistry C.* **2015**, *3* (29), 7627-7631 10.1039/c5tc01633a

54. Sadeghi, I.; Kronenberg, J., Asatekin, A. Selective Transport through Membranes with Charged Nanochannels Formed by Scalable Self-Assembly of Random Copolymer Micelles. *ACS Nano*. **2018**, *12* (1), 95-108 10.1021/acsnano.7b07596